

Open quantum dots modeled with microwave cavities

A Dissertation
Presented in Partial Fulfillment of the Requirements
for the Degree of
Doctor of natural science
(Dr. rer. nat.)



Submitted to the Faculty of Physics,
Philipps-University Marburg

by

Young-Hee Kim

from Seoul

Marburg/Lahn
November 2004

Vom Fachbereich Physik der Philipps-Universität Marburg/Lahn

als Dissertation angenommen am 02.11.2004

Erstgutachter: Prof. Dr. H.-J. Stöckmann

Zweitgutachter: Prof. Dr. J. P. Bird

Tag der mündlichen Prüfung: 12.11.2004

Zusammenfassung

In dieser Arbeit werden offene Mikrowellenresonatoren mit harten Wänden und mit weichen Wänden als Modellsystem eines Quantenpunktes untersucht. Da die Quantenpunkte Abmessungen im μm -Bereich haben, ist es noch schwierig, dabei verschiedene Messungen durchzuführen, bis auf die Transportmessungen. Für die Simulation sind die Mikrowellenresonatoren nach einem Quantenpunktbillard angefertigt, das in der Arbeitsgruppe von J. P. Bird untersucht wurde.

Erstens werden die periodisch vorkommenden vernarbten Wellenfunktionsfamilien bei einem Resonator mit harten Wänden analysiert und die möglichen entsprechenden Bahnen werden identifiziert. Um die komplizierteren vernarbten Wellenfunktionsfamilien zuzuordnen, wurden Kanaltransmissionsmessungen durchgeführt, wobei ein Absorber auf 1381 Positionen auf einem 5-mm-Raster positioniert wurde. Dann wird der Einfluss des Absorbers untersucht, indem die Transmissionsdaten fouriertransformiert werden, und Fourierabbildungen davon analysiert werden. Die berechneten Bahnlängen und die von den Experimenten erhaltenen Werte stimmen gut überein.

Durch Variation des Abstands zwischen Deckel und Boden des Resonators lassen sich Potentiale simulieren, wobei die Äquivalenz zwischen Quantenmechanik und Elektrodynamik ausgenutzt wird. Dadurch wurde ein Resonator mit den weichen Wänden erzeugt, dessen Potentialstruktur einem Quantenpunktbillard entspricht. Die bei dem Billard gemessenen Eigenfrequenzen für die periodischen Bouncing-Ball-Familien mit den Theoriewerten, die über eine WKB-Näherung berechnet werden, zeigen sehr gute Übereinstimmung. Die Wellenfunktionsfamilie mit einer X-förmigen Bahn wird als ein Beweis des dynamischen Tunnelns untersucht. Durch die Phasendifferenzanalyse und das Transportverhalten wird das dynamische Tunneln nachgewiesen, welches bei Mikrowellenexperiment schwierig zu beobachten ist.

Im letzten Abschnitt werden die statistischen Eigenschaften der Wellenfunktionen bei einem unsymmetrischen offenen Billard mit harten Wänden diskutiert. Die Öffnung zu der Außenwelt des Billards macht die Wellenfunktion komplex, da die Wellen nicht nur rein stehend ist, sondern auch laufend vorkommen. Das Übergangsgebiet von der reellen zu der imaginären Wellenfunktion wird untersucht, indem die Öffnungen des Billards durch Frequenzänderung erhöht werden. Die Verteilung der Phasensteifigkeit, die das Verhältnis von Imaginärteil zu Realteil angibt, die weitreichenden Korrelationen der Intensität und der Stromdichte werden verglichen mit den Theoriewerten, die mit der *random superposition of plane waves*-Theorie [Ber77] berechnet werden. Bei allen untersuchten Größen findet man gute Übereinstimmung zwischen Experiment und Theorie.

Abstract

In this work, open microwave resonators have been investigated as a model system of a quantum dot. Since quantum dots are μm -sized, measurements in quantum dots are still very difficult except for transport measurement, but relatively simple in a microwave resonator. We fabricated a flat resonator and a resonator with soft-wall potential so that the shape corresponded to a quantum dot which has been investigated in the laboratory of J. P. Bird.

For a flat resonator, *i. e.* a resonator with a hard-wall potential, periodically occurring scarred wave function families are analyzed, and the associated orbits are identified. For complicated wave function families, we use a Fourier spectroscopy. Influence of an absorber center is investigated using Fourier transform of transmission between the input and output leads. The Fourier map is analyzed to identify scar families. The calculated orbits lengths and the experimentally obtained values show very good agreement.

By varying the height of the resonator, potentials can be simulated, using the correspondence between quantum mechanics and electrodynamics. Using this relation, a resonator with soft-wall potential was fabricated. The shape of the potential corresponds to the above mentioned quantum dot. The measured eigenfrequencies for the periodic bouncing-ball scar families agree very well with the theoretical values from a WKB approximation. The wave function family of an X-like cross bouncing ball is used to obtain evidence of dynamical tunneling. By phase difference analysis and transport behavior, the presence of dynamical tunneling is proven.

In the last part of this work, the statistical properties of the wave functions of an asymmetric open flat resonator are discussed. Opening to the outside world of billiard makes the wave function complex, since there is transport. This cross-over regime, from real to imaginary of wave functions is investigated opening of the billiard by frequency increasing. The phase rigidity distribution which give the ratio between the real and imaginary parts of the wave function, the long-range correlation of intensity and the current density are compared with the theoretical values calculated from the *random superposition of plane waves* theory [Ber77]. For all investigated quantities, a very good agreement between experiment and theory is found.

Contents

1	Introduction	5
2	Basic principles of microwave experiments	7
2.1	Theoretical background	7
2.2	Measuring technique	9
3	Quantum-dot like resonator	12
3.1	Background	12
3.2	Hard-wall billiard	13
3.2.1	Experiment	13
3.2.2	Wave function scarring	18
3.2.3	Scanning Fourier spectroscopy	23
3.3	Soft-wall resonator	31
3.3.1	Experiment	31
3.3.2	WKB approximaion	37
3.3.3	Dynamical tunneling	41
3.3.4	Outlook	46
4	Wave function statistics for open systems	47
4.1	Intensity distribution in dependence of the phase rigidity	47

4.2	Current and vorticity auto correlation	52
4.3	Long-range correlation	59
A	Fitted wave functions for the soft-wall billiard	66
B	WKB approximation	73
C	Random superposition of plane waves	76
D	Mathematical functions/ formulas	78
	Bibliography	80

List of Figures

2.1	Sketch of resonator and measurement table	11
3.1	Quantum dot and corresponding potential	13
3.2	Set up: Sketch and Photograph of the quantum dot resonator . .	14
3.3	Channel transmission spectrum in open microwave cavity	15
3.4	Magnetoconductance on a quantum dot and transmission in a resonator	16
3.5	Typical wave functions and corresponding current distributions . .	17
3.6	Eigenfrequencies at horizontal bouncing ball scars (hard wall billiard)	19
3.7	Eigenfrequencies at vertical bouncing ball scars (hard wall billiard)	20
3.8	Eigenfrequencies at diamond-like scars (hard wall billiard)	21
3.9	Complicated scar families	22
3.10	Sketch of the billiard scanning	23
3.11	Transmission spectra $ S_{32} $ with different absorber position	24
3.12	Wave function comparison for different absorber positions	25
3.13	Wave functions for periodic orbits with an absorber	26
3.14	Length spectra with an absorber at different positions	27
3.15	Channel transmission map $ S_{32} $ with absorber scan	29
3.16	Classical trajectories and the Fourier maps	30
3.17	Structure of resonator and corresponding potential	32
3.18	Measured reflection and transmission spectra of soft-wall resonator	33
3.19	Comparison of selected wave functions	35

3.20	Selected wave functions of the soft-wall resonator	36
3.21	Vertical bouncing-ball scarred wave functions	38
3.22	Horizontal bouncing-ball scarred wave functions	39
3.23	Cross bouncing-ball scarred wave functions	40
3.24	Cross-like scarred wave function	41
3.25	Clean and Dirty states	42
3.26	Dirty states by breaking the symmetry of potential	42
3.27	Mean value of the phase difference over the measured area $\langle \Delta\phi \rangle_{(x,y)}$	43
3.28	Spectrum $ S_{11} $, $ S_{32} $ and phase difference at 15.285 GHz	44
3.29	Typical cross bouncing-ball scar near 15.285 GHz	45
4.1	Intensity distribution for the wave function	50
4.2	Typical wave functions and corresponding current distributions for asymmetrical billiard	51
4.3	Selected vorticity map	52
4.4	Spatial autocorrelation functions	54
4.5	Spatial autocorrelation functions of $j_x(r)$, $j_y(r)$, $j_{\parallel}(r)$, and $j_{\perp}(r)$.	55
4.6	Experimental spatial autocorrelation functions of the vorticity $\omega(r)$	56
4.7	Vortex pair correlation function	57
4.8	Nearest neighbor distance distribution of vortices	58
4.9	Phase rigidity distribution	61
4.10	Connected correlator of squared intensity	62
4.11	Connected correlator of squared intensity and squared current den- sity	63
4.12	Connected correlator of squared current density	64

Chapter 1

Introduction

The difference between regular motion in integrable systems and chaotic motion in non-integrable systems is observed by the chronological expansion of neighboring trajectories in phase space. Two trajectories that start out very close to each other separate only linearly in the case of regular motion, whereas they separate exponentially in the case of chaotic motion. The corresponded exponent is called the Lyapunov-exponent [Sch94].

Since the phase space trajectory is meaningless in quantum mechanics, the classical definition of “*chaos*” is not directly applicable. From Bohr’s correspondence principle, we expect a gradual transition from quantum to classical mechanics in the limit $\hbar \rightarrow 0$, corresponding to high quantum numbers. In this semiclassical region, the classical chaotic motion can be recognized again [Gut90, Haa01]. The survey of such quantum systems is called “*quantum chaos*”. From a statistical point of view, eigenvalues and eigenfunctions of the wave equation in a chaotic system can be described by a random-superposition of plane-waves (RSPW) [Ber77], as well as by random matrix theory (RMT) [Bro81, Ber85, Guh97]. Numerical calculations for a chaotic system are very time consuming. Therefore experimental approaches are beneficial. In our group, various billiard systems have been investigated by means of microwave experiments and many theoretical predictions have been proved [Stö90, Ste93, Per00, Kuh01, Sch01, Bar01, Kim02].

Quantum dot billiard experiments have been of interest, too. They were initiated by C.M. Marcus and coworkers [Mar92], studying electronic transport through ballistic microscopic semiconductor structures. These consist of a mesoscopic scattering region, connected to external reservoirs by means of quantum-point-contact leads. In recent studies of such dots by J.P. Bird [Bir99, Bir97b], their transport characteristics were found to exhibit evidence for the presence of strongly scarred wave function states [Jal90, Mar92, Fro94, Fro95]. In submicron-

sized semiconductor structures, experiments are confined to transport measurements whereas microwave experiments allow wave function and current measurements as well. Chapter 3 shall deal with the simulation of a quantum dot billiard with an open microwave cavity. In section 3.2, we shall demonstrate how microwave experiments may be used to perform analog studies of transport, and the influence of a movable scattering center on the wave function in an open quantum dot.

Adiabatic changes of the resonator height allow the realization of a soft-wall potential in a microwave resonator. H.M. Lauber presented a microwave experiment with a harmonic potential and a Hénon-Heiles potential in his thesis [Lau94]. In section 3.3, we shall present the transmission properties and the wave functions of an open microwave resonator with a soft-wall potential, simulating the typical structure of a quantum-dot potential.

Over the last twenty years, the role of quantum mechanical tunneling has received considerable attention. Many of the recently discovered tunneling phenomena involve a counterpart to potential barrier penetration called dynamical tunneling by Davis and Heller [Dav81, Hel95]. This tunneling occurs between two separated regions of classically trapped quasiperiodic motion in the phase space. We shall show experimental evidence of the existence of dynamical tunneling between two distinct two regions in phase space in section 3.3.3.

Wave functions in a chaotic billiard cross over from real to complex as the the opening to the outside world increases. Recently, the full real-to-complex cross over regime was studied using microwave experiments [Bar02, Chu00]. The statistical distribution of wave functions in the cross over regime depends on how the average is taken over the coordinate \vec{r} , the frequency ν , or both. In chapter 4, we shall show the distribution of intensities, currents and vorticities, as well as phase rigidity fluctuations, long-range correlations of intensity and current density.

Chapter 2

Basic principles of microwave experiments

2.1 Theoretical background

In a flat microwave resonator of height d whose top and bottom plates are parallel to each other, the stationary solutions of electrodynamic wave equations, whose time dependencies are described by harmonic oscillation, follow [Jac82]

$$\frac{1}{c^2} \frac{\partial^2}{\partial t^2} \begin{pmatrix} \vec{E}(x, y, z, t) \\ \vec{B}(x, y, z, t) \end{pmatrix} = \Delta \begin{pmatrix} \vec{E}(x, y) \\ \vec{B}(x, y) \end{pmatrix} \exp i(k_z z - \omega t) \quad (2.1)$$

where the electric field $\vec{E}(x, y)$ and the magnetic field $\vec{B}(x, y)$ do not depend on each other. This leads to the Helmholtz-Equation

$$[\Delta_{x,y} + k^2 - k_z^2] \begin{pmatrix} \vec{E}(x, y) \\ \vec{B}(x, y) \end{pmatrix} = 0, \quad (2.2)$$

where the wave vector $k = \frac{2\pi\nu}{c}$, the z -component of the wave vector $k_z = \frac{\theta\pi}{d}$, $\theta = 0, 1, 2, \dots$, and ν and c are frequency and the velocity of light respectively.

We can decompose the vectors following

$$\begin{pmatrix} \vec{E} \\ \vec{B} \end{pmatrix} = \begin{pmatrix} \vec{E}_z + \vec{E}_{xy} \\ \vec{B}_z + \vec{B}_{xy} \end{pmatrix} \quad (2.3)$$

where \vec{E}_z , \vec{B}_z are z -components, and the \vec{E}_{xy} , \vec{B}_{xy} $x - y$ -components which are parallel to the $x - y$ plane. With the boundary conditions

$$\begin{pmatrix} \vec{E}_{tang} \\ \vec{B}_{norm} \end{pmatrix} = 0 \quad (2.4)$$

where \vec{E}_{tang} : tangential component to the resonator boundary

\vec{B}_{norm} : normal component to the resonator boundary,

one can obtain the solutions of Eq. (2.2)

for the TE (Transversal-Electric) - Modes:

$$\begin{aligned} B_z &= B_z(x, y) \sin\left(\frac{\theta\pi}{d}z\right), \quad \theta = 1, 2, 3, \dots \\ E_z &= 0 \end{aligned} \quad (2.5)$$

for the TM (Transversal-Magnetic) - Modes:

$$\begin{aligned} E_z &= E_z(x, y) \cos\left(\frac{\theta\pi}{d}z\right), \quad \theta = 0, 1, 2, \dots, \\ B_z &= 0 \end{aligned} \quad (2.6)$$

Eq. 2.2 is equivalent to the stationary Schrödinger equation for a particle in a potential $V(x, y)$.

$$\left[\Delta_{x,y} + \frac{2mE}{\hbar^2} - \frac{2mV(x, y)}{\hbar^2} \right] \psi(x, y) = 0 \quad (2.7)$$

It yields the following correspondences

$$\psi(x, y) \equiv E_z(x, y) \quad (2.8)$$

$$\frac{2mE_n}{\hbar^2} \equiv k_n^2 = \left(\frac{2\pi\nu_n}{c}\right)^2 \quad (2.9)$$

$$\frac{2mV}{\hbar^2} \equiv k_z^2 = \left(\frac{\theta\pi}{d}\right)^2 \quad (2.10)$$

These correspondences between quantum mechanics and electrodynamics go even further. For a quasi-two-dimensional resonator, the Poynting vector is given by [Šeb99]

$$\vec{S}(x, y) \sim \text{Im}[E_z^*(x, y)\nabla E_z(x, y)] \quad (2.11)$$

This corresponds to the quantum mechanical probability current density

$$\vec{j}(x, y) \sim \text{Im}[\psi^*(x, y)\nabla\psi(x, y)]. \quad (2.12)$$

Thus, we arrive at a direct correspondence between the current density and the Poynting vector. Since the latter may be measured directly in experiment, the quantum-mechanical current density may also be obtained.

Below the frequency $\nu_{max} = \frac{c}{2d}$ only the TM-Mode remains for $\theta = 0$. Then Eq. (2.2) can be reduced to

$$\left(\Delta_{x,y} + \left(\frac{2\pi\nu_n}{c} \right)^2 \right) E_z(x, y) = 0 \quad (2.13)$$

with Dirichlet boundary conditions at the resonator walls, *i. e.* $E_z = 0$. This is equivalent to the stationary Schrödinger equation of a two-dimensional billiard with hard walls [Stö99]

$$\left(\Delta_{x,y} + \frac{2mE}{\hbar^2} \right) \psi(x, y) = 0. \quad (2.14)$$

If the top and bottom plates are not exactly parallel, but the height d of the resonator varies with (x, y) , then the z -component of the wave vector k_z should adapt the (x, y) -dependent boundary condition. The separation of the z -component dependence resulting into Eq. (2.6) is no longer exact. But error terms are small, if $d(x, y)$ varies only adiabatically on the scale of the de Broglie wave length. The Helmholtz Equation for TM-mode for $\theta = 1$ is equivalent to the Schrödinger equation for a particle in a soft potential.

From Eq. (2.10), the following relation between the potential $V(x, y)$ and the resonator height $d(x, y)$ is obtained

$$\frac{2mV(x, y)}{\hbar^2} \equiv \left(\frac{\pi}{d(x, y)} \right)^2 \quad (2.15)$$

This relation will be applied to fabricate a microwave resonator with a soft wall potential (see section 3.3.1).

2.2 Measuring technique

For our measurements, we use antennas as input and output channels. The transmission- and reflection behavior of systems can be described by scattering-matrix theory.

For example, a measurement with two antennas is considered as a 2-channel-scattering-system. The combination of the output signals b_1 and b_2 (the amplitudes of the outbound waves) with the input signals a_1 and a_2 (amplitudes of the incoming waves) is described by the so called S-parameters (elements of scattering matrix),

$$\begin{pmatrix} b_1 \\ b_2 \end{pmatrix} = \begin{pmatrix} S_{11} & S_{12} \\ S_{21} & S_{22} \end{pmatrix} \begin{pmatrix} a_1 \\ a_2 \end{pmatrix} \quad (2.16)$$

The relation between S and the electrodynamic Greensfunction for billiards is derived in [Ste95]. For isolated resonances, it reduces to a billiard Breit-Wigner function.

$$S_{ij} = \delta_{ij} - 2(\alpha + i\beta)G(\vec{r}_i, \vec{r}_j; k) \quad (2.17)$$

where α , β are coupling constants which depend on antenna geometry, and

$$G(\vec{r}_i, \vec{r}_j; k) = \sum_{n=1}^{\infty} \frac{\psi_n(\vec{r}_i)\psi_n(\vec{r}_j)}{k_n^2 - k^2 + \Delta_n - \frac{i}{2}\Gamma_n} \quad (2.18)$$

where

$$\begin{aligned} \psi_n(\vec{r}_i) &: \text{wave function of undisturbed systems at } \vec{r}_i = (x_i, y_i) \\ \Gamma_n &: \text{the spectral line width of resonance with } \Gamma_n = \alpha \sum_i |\psi_n(\vec{r}_i)|^2 \\ \Delta_n &: \text{the resonance shift with } \Delta_n = \beta \sum_i |\psi_n(\vec{r}_i)|^2 \end{aligned}$$

In the resonance case ($k^2 = k_n^2 + \Delta_n$), Eq. 2.17 becomes

$$S_{ij} = \delta_{ij} + 2(-\beta + i\alpha) \frac{\psi_n(\vec{r}_i)\psi_n(\vec{r}_j)}{\frac{1}{2}\Gamma_n} \quad (2.19)$$

For the reflection measurement S_{ii} with $i = 1, 2$, the amplitudes $|\psi_n(\vec{r}_i)|^2$ at \vec{r}_i are accordingly to calculate :

$$|\psi_n(\vec{r}_i)|^2 = \frac{(1 - \text{Re}(S_{ii}(\vec{r}_i)))\Gamma_n}{4\beta} = \frac{\text{Im}(S_{ii}(\vec{r}_i))\Gamma_n}{4\alpha} \quad (2.20)$$

The Agilent8720ES VNA (Vectorial Network Analyzer) measures the entire scattering matrix S of a system with modulus and phase as function of frequency.

The VNA 8720ES can measure in the frequency range of 0.05-20 GHz with a maximal resolution of 1 kHz. A detailed description is found in [Ste93, Bar01].

Two dimensional wave function measurements can be measured with a measurement table, in which we move the antenna position by computer control. To

control the devices and to record the measured data, a program written by U. Kuhl in Delphi is used [Ste93, Kuh98].

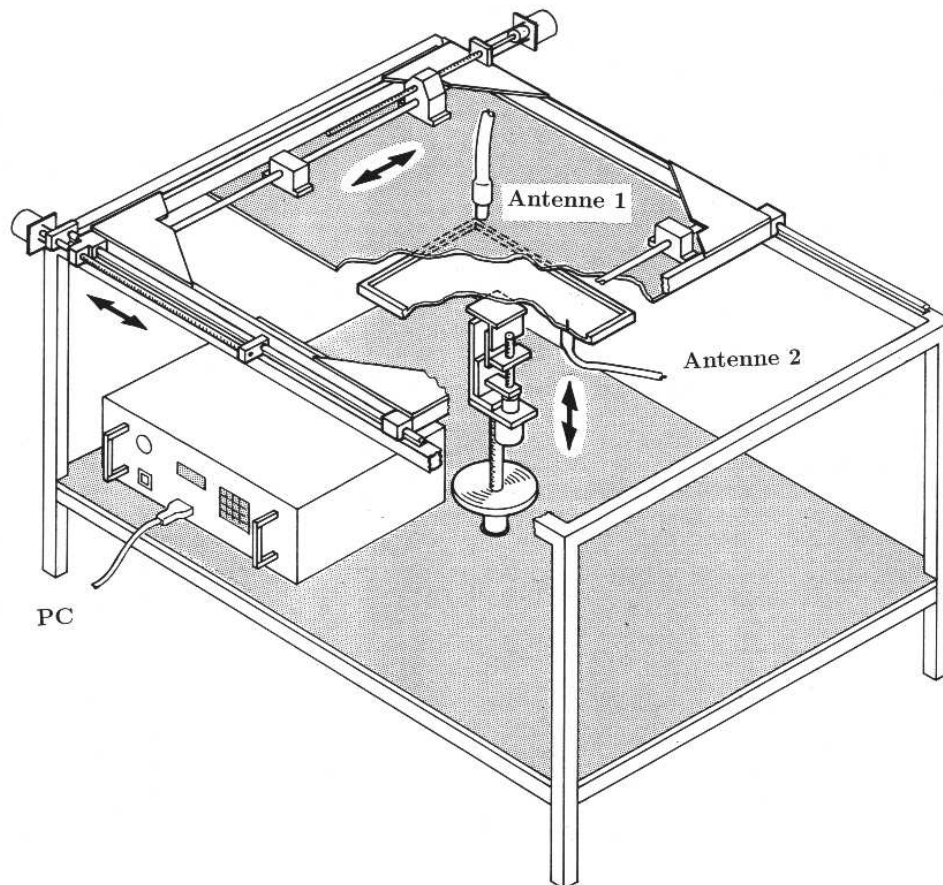


Figure 2.1: Sketch of resonator with coupling antenna and measurement table [Kuh98]

Chapter 3

Quantum-dot like resonator

3.1 Background

During the last decades, it has become possible to manufacture structures of μm size. In the case of semiconductors, electrons can form a two-dimensional gas located between two layers of a heterostructure. The potential confining this two-dimensional gas can be controlled. At temperatures below 1 K, the phase coherence length is larger than the system size, and quantum coherence plays an important role. The elastic mean free path length is typically $10\ \mu\text{m}$ or larger. The electrons move “*ballistically*”, *i. e.* they scatter only at the boundaries defined by the confining potential. The device can be viewed as a billiard and is called a quantum dot. The number of electrons in the dot varies typically from just a few to several hundred. The coupling between the dot and leads may be controlled by gates which create a potential barrier.

Quantum-dot-billiard experiments were initiated by C.M. Marcus and coworkers [Mar92], who studied electronic transport through ballistic microscopic semiconductor structures which consist of a mesoscopic scattering region, connected to external reservoirs by means of quantum-point-contact leads. The quantum dot billiards are true quantum mechanical systems. The motion of the electrons can be modified by the presence of magnetic fields due to Lorentz forces leading to a break of time-reversal symmetry. To achieve ballistic electron transport, the measurements have to be done well below 1 K to suppress phonon induced scattering. In recent studies of such dots by J.P. Bird [Bir99, Bir97b], their transport characteristics were found to exhibit evidence for the presence of strongly scarred wave function states [Jal90, Mar92, Fro94, Fro95] which recur in intensity when either the magnetic field or the energy is varied. The scarred wave functions have important implications for the semiclassical description of trans-

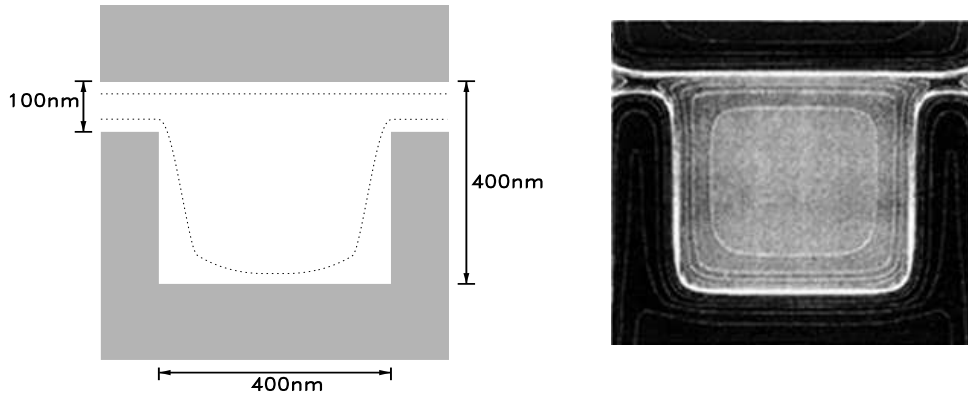


Figure 3.1: Quantum dot and corresponding potential

The quantum dot studied by J.P. Bird (left panel). The grey regions denote the gate pattern of the quantum dot. The dotted line roughly indicates the expected profile of the quantum dot that forms in the two-dimensional electron gas layer. The contour lines of the corresponding potential [Bir95, Mic98] are shown in the right panel.

port in dots, since they indicate a highly nonuniform sampling of phase space within the dot. Such behavior is in turn inconsistent with the assumption of fully chaotic transport, which is often made in semiclassical treatments of these dots. In submicron-sized semiconductor structures, essentially, only transport measurements can be performed. Wave functions can not be measured which are accessible in microwave experiment. This was the motivation of our microwave experiment. Magnetoconductance fluctuation in the quantum dot were studied by J.P. Bird and co-workers cite[Bir95, Bir97, Bir99].

We simulated the open quantum dot experiment by J.P. Bird which is shown in Fig. 3.1 and in Refs. [Bir97a, Bir97b]. By confirming the presence of measurable transport results, associated with the wave function scars, our studies demonstrate the usefulness of microwave-analog studies of transport in mesoscopic systems.

3.2 Hard-wall billiard

3.2.1 Experiment

The quantum-dot like resonator ($160\text{ mm} \times 210\text{ mm} \times 8\text{ mm}$) was made of brass and the geometry shown in Figure 3.2 was used to measure the entire of the scatter-

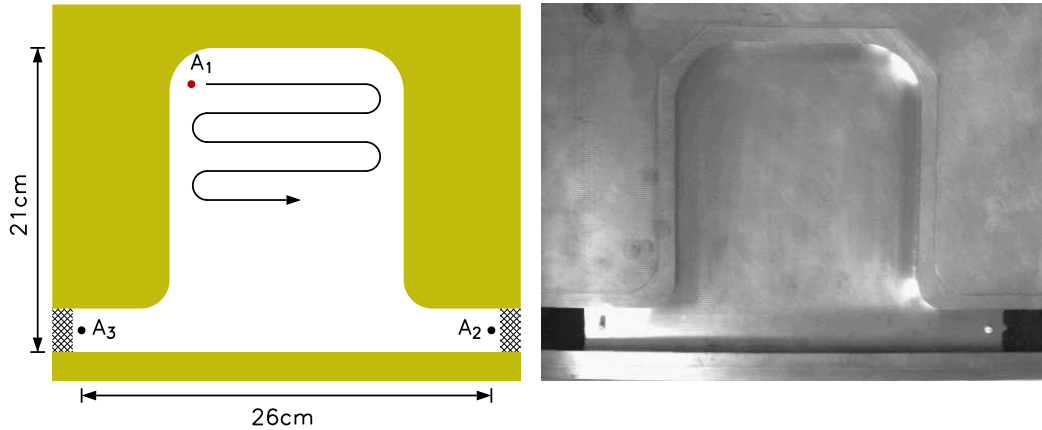


Figure 3.2: Set up: Sketch and Photograph of the quantum dot resonator
 Left: Sketch of the billiard, A_1 is the probe antenna and A_2 , A_3 are input and output antennas, respectively. Right: Photograph of the billiard. At the end of each lead, an absorber is placed to avoid reflections.

ing matrix S (see Eqs. (2.16) - (2.20)), with modulus and phase, as function of frequency. The height $d = 8$ mm ensures that only a single transverse mode is present at frequencies up to $\nu_{max} = 18.7$ GHz as explained in section 2.1. To open the system, two waveguides with width of 30 mm were included at the bottom corners of the resonator. In the end of the leads, absorbers made of carbon-doped-glass-fiber were placed to reduce unwanted reflections. The antennas A_2 and A_3 in the leads were of standard construction, consisting of an inner conductor (copper) of diameter 1 mm, which is coated by teflon of diameter 4 mm. To minimize the leakage through the probe antenna, the diameter of the probe antenna A_1 was reduced to 0.2 mm and it was not coated by teflon. The billiard was set on the measurement table in Figure 2.1. On the top plate of the measurement table, the probe antenna A_1 was mounted and scanned the billiard by moving the top plate [Kuh98] on a square grid of period 5 mm. The transmission S_{12} between the input antenna A_2 and the movable scanning antenna A_1 , and the reflection S_{11} at the scanning antenna A_1 were measured at 1381 positions in the frequency range of 1 - 17 GHz in steps of 0.5 MHz. As reference, the transmission S_{32} between A_2 and A_3 was measured. The measured transmission spectrum S_{32} is shown in Fig. 3.3. The width of each lead is $W = 3$ cm. Hence the system is open for frequencies higher than the threshold frequency $\nu_T = \frac{c}{2W} = 5$ GHz. The second and third modes open at $2\nu_T$ and $3\nu_T$. The billiard has two leads connecting it to the external world. Hence the total number of channels N is 2, 4, 6 for the first, second, and third mode respectively. These threshold frequencies of the modes are marked with dashed lines in Fig. 3.3. In the experiment, however, because of the limited length of the leads, the effect of evanescent modes can be seen close to the threshold frequencies. In Fig.3.4, the transmission fluctuation

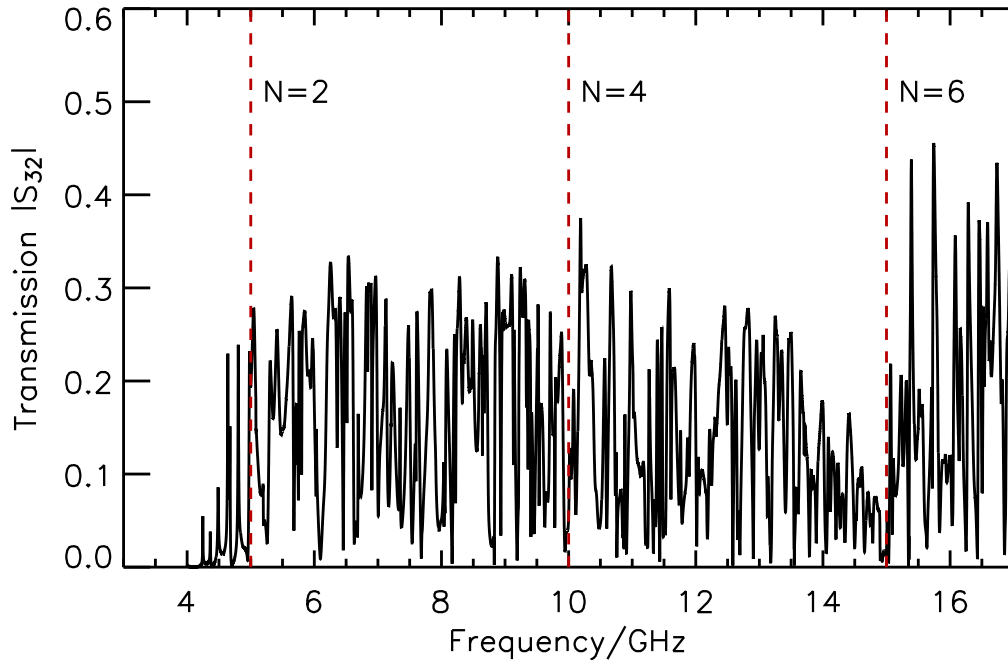


Figure 3.3: Channel transmission spectrum in open microwave cavity. Transmission $|S_{32}|$ from the input antenna A_2 in the right lead to the output antenna A_3 in the left lead. The dashed lines indicate where the first, second, third mode open, *i. e.* total number of channels ($N = 2$, $N = 4$, $N = 6$) changes at the frequencies.

$|S_{32}|$ is expanded in the frequency range of 7.5-10 GHz and the magnetoconductance fluctuation in the quantum dot are compared. In this frequency range, only one mode for each lead is open and the ratio of wave length to the cavity size corresponds to the ratio of the Fermi wavelength $\lambda \sim 40\text{nm}$ and the effective size $\sim 300\text{nm}$ of the quantum dot [Mic98] shown in Fig. 3.1. This comparison of such similar features in these two different systems provides a clear indication that the wave-like nature of the electron is critical to understanding the main aspects of transport in the quantum dots. Fig. 3.5 shows typical wave functions (left panel) and current distributions (right panel) within the microwave resonator. We used the transmission S_{12} between the input antenna in the right lead A_2 and the probe antenna A_1 for these plots. Dark region in wave functions corresponds to maximum intensity and arrow lengths in flow map indicate the magnitude of the Poynting vector. The corresponding frequencies are marked in the channel transmission spectrum $|S_{32}|$ of Fig. 3.4. At 9.241 and 9.310 GHz, leakage current through the probe antenna can give rise to unwanted artifacts in the measurements. At most frequencies where the transmission is larger, it is no significant problem, as shown in Fig. 3.5 for 8.281 GHz.

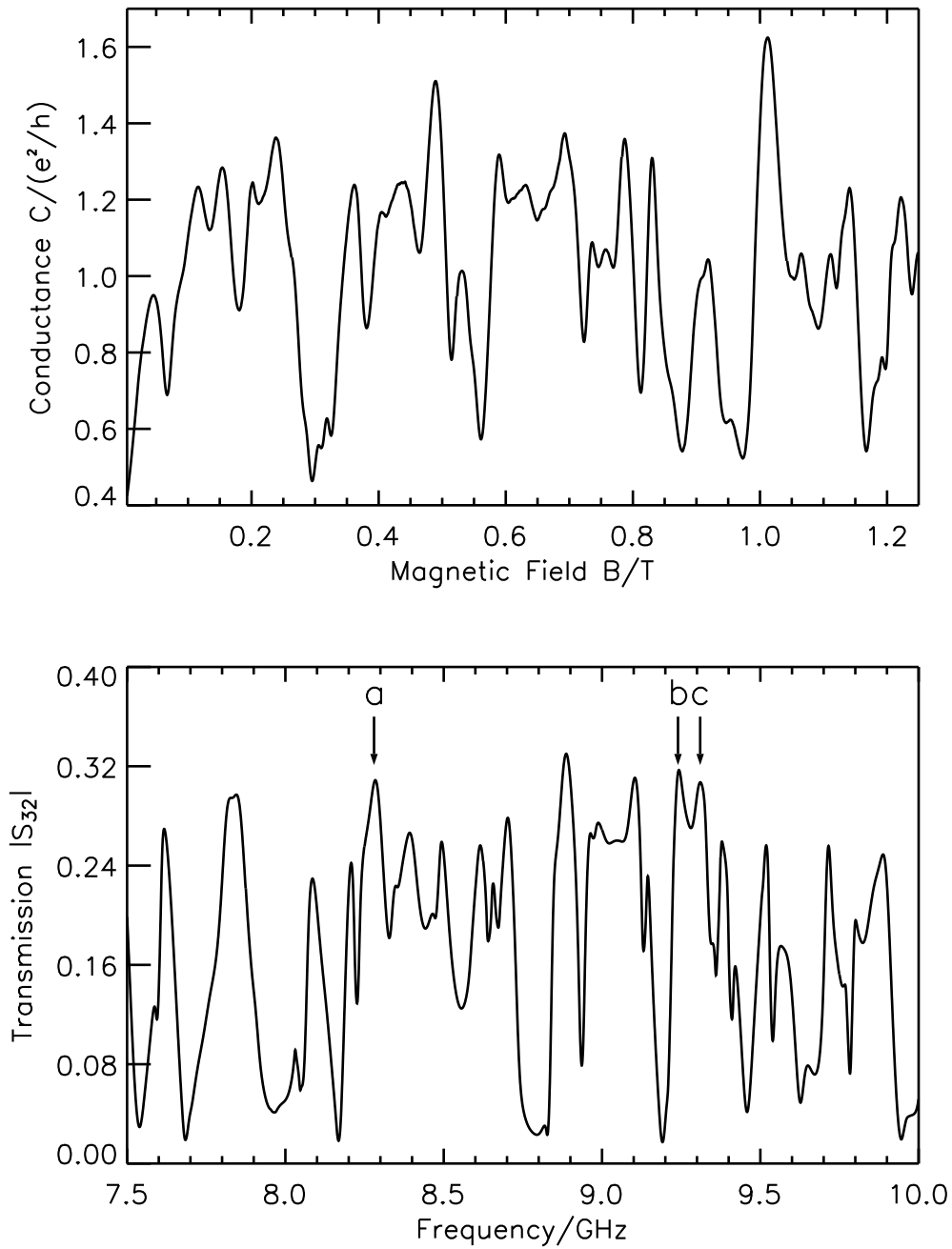


Figure 3.4: Magnetoconductance on a quantum dot and transmission in a resonator

Upper panel shows the magnetoconductance fluctuations observed in the quantum dot of Fig. 3.1. In the lower panel, with Gaussian window smoothed transmission spectrum $|S_{32}|$ is shown in the frequency range of 7.5 GHz – 10 GHz. The two curves are comparable to each other.

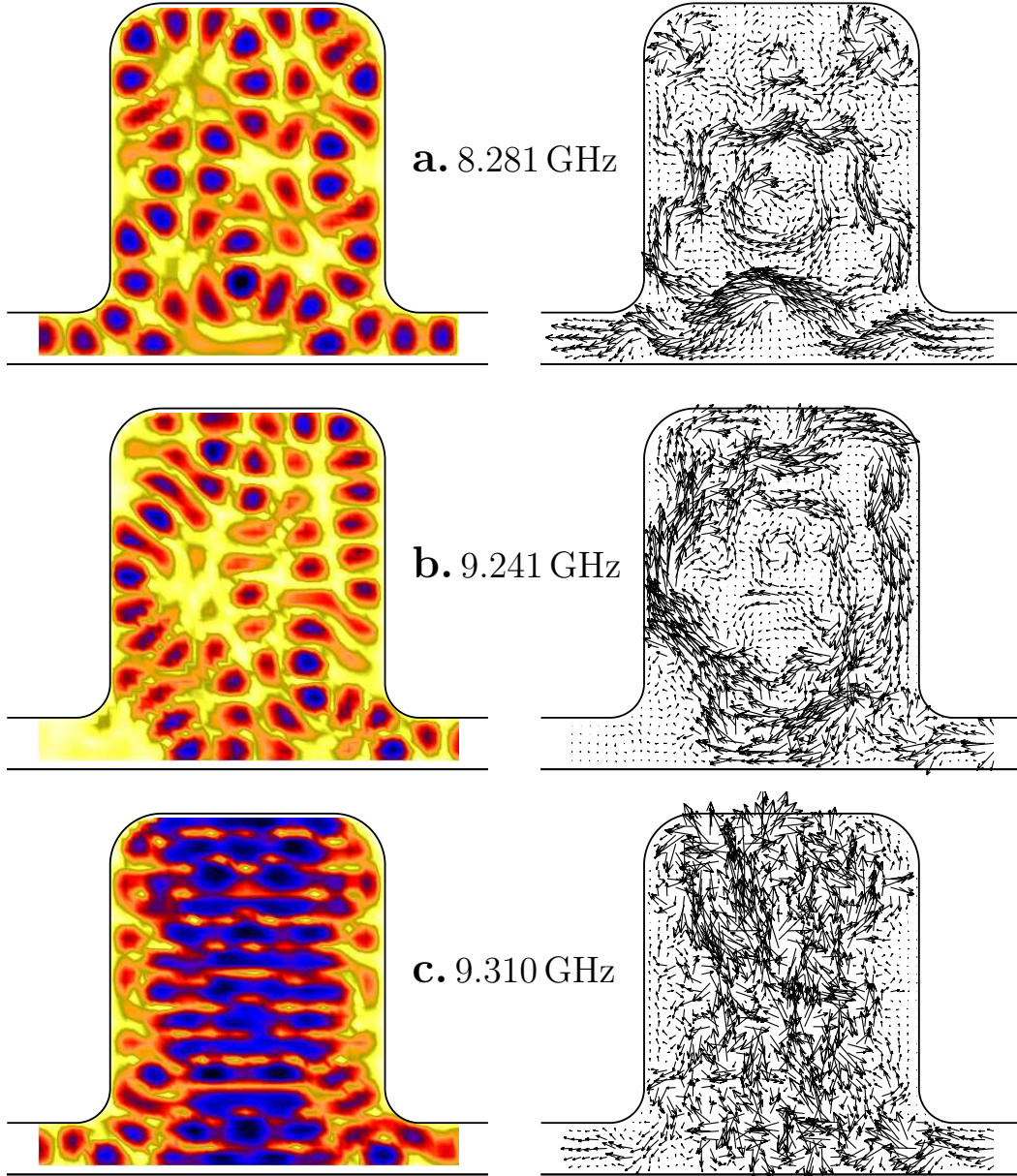


Figure 3.5: Typical wave functions and corresponding current distributions. The selected wave function plots $|S_{12}|$ (left column) and the corresponding current distributions (right column) for $a = 8.281$ GHz, $b = 9.241$ GHz, $c = 9.310$ GHz. Dark region in wave functions corresponds to maximum intensity and arrow lengths in flow map indicate the magnitude of the Poynting vector. The corresponding frequencies are marked in the channel transmission spectrum $|S_{32}|$ of Fig. 3.4.

3.2.2 Wave function scarring

In Fig. 3.6, the frequencies at which horizontal bouncing ball wave functions occur are plotted versus node index n in the upper panel. The corresponding wave functions obtained from the modulus of the transmission $|S_{12}|$ for the node indexes $n = 3, 5, 6, 9, 11, 14$ are shown in the lower panel. From this figure, one can see that the scars recur quite regularly as the frequency varies. The slope of the straight line corresponds to a period $\Delta\nu = 0.937$ GHz. Since the orbit length should be an integer multiple of the wavelength $l = n\lambda$, this corresponds to an orbit length $l = c/\Delta\nu = 0.32$ m which is exactly twice the distance between the vertical faces of the billiard. Fig. 3.7 and Fig. 3.8 show vertical bouncing ball and diamond-like scar families, respectively. From the upper panels of the Figures, we too can calculate the slope gradients which yield the orbits lengths. The period of the vertical bouncing ball orbits $\Delta\nu = 0.708$ GHz corresponds to an orbit length 0.42 m. This is the twice distance between the horizontal faces of the cavity as expected. The same process yields a frequency period $\Delta\nu = 0.563$ GHz corresponding to an orbits length 0.53 m for the diamond like orbits which we also obtained by a calculation of this orbit with the billiard size.

We have found very regularly and clearly recurring horizontal and vertical bouncing ball and diamond like scar families. For these scar families, we could find an exact agreement between the orbit lengths obtained by the frequency periods $\Delta\nu$ and the orbit lengths calculated from the billiard size.

Additionally, there are several complicated scars which also recur as the frequency is varied. Typical member of these scar families are shown in Fig. 3.9. To find all members of these scar families is difficult due to their overlapp with the stronger scarred wave functions, and their instability. Hence we could not obtain exact periods of these scar families. The possible orbits whose lengths are matched with approximately found periods of the scar families are plotted with white lines in the selected wave functions in Fig. 3.9. In the next section, such complicated cases are carefully investigated with the periodic orbits theory and the Scanning Fourier spectroscopy [Gut90, Stö99].

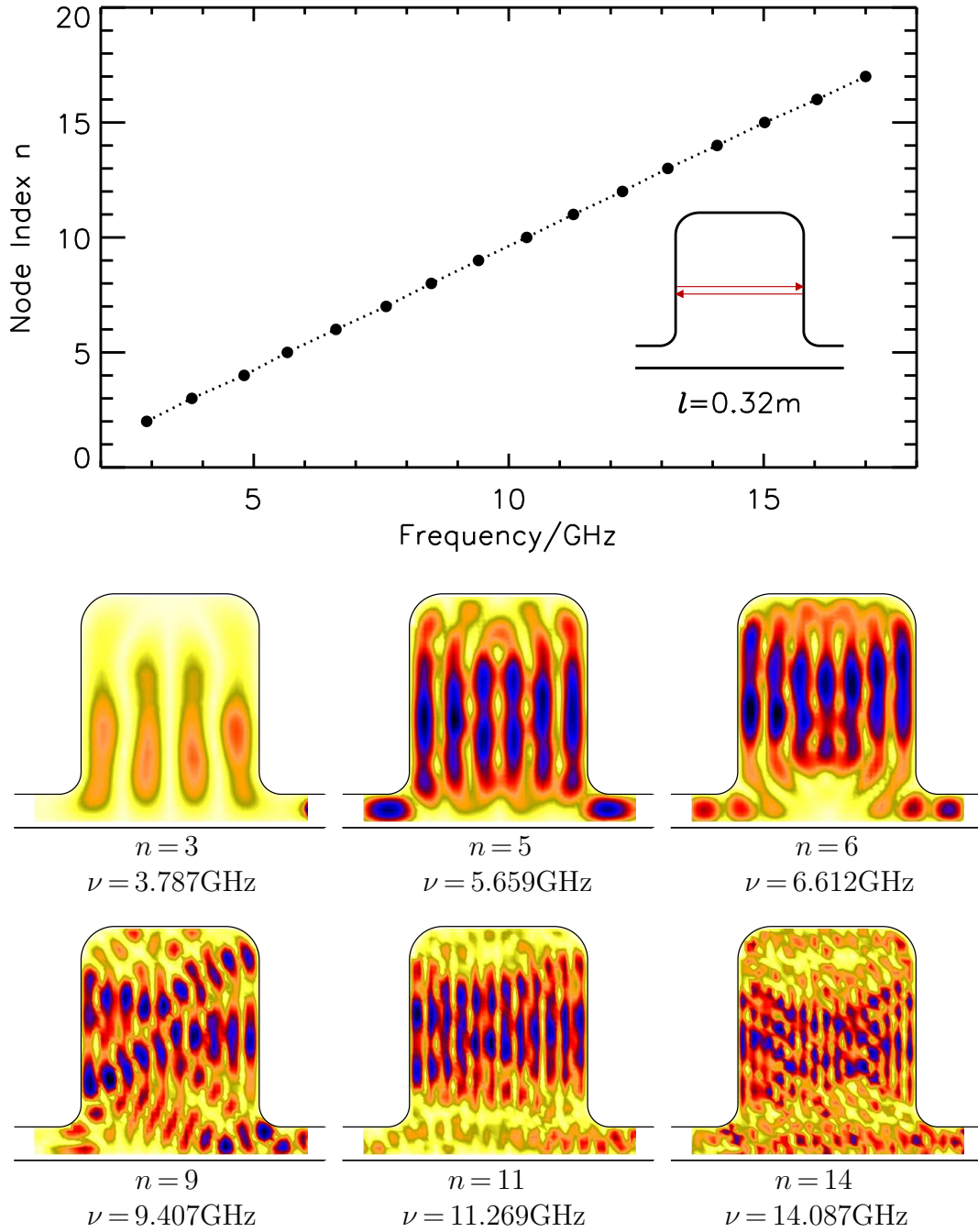


Figure 3.6: Eigenfrequencies at horizontal bouncing ball scars (hard wall billiard) The measured frequencies at horizontal bouncing ball wave functions are plotted in the upper panel and the typical member of the corresponding scar family.

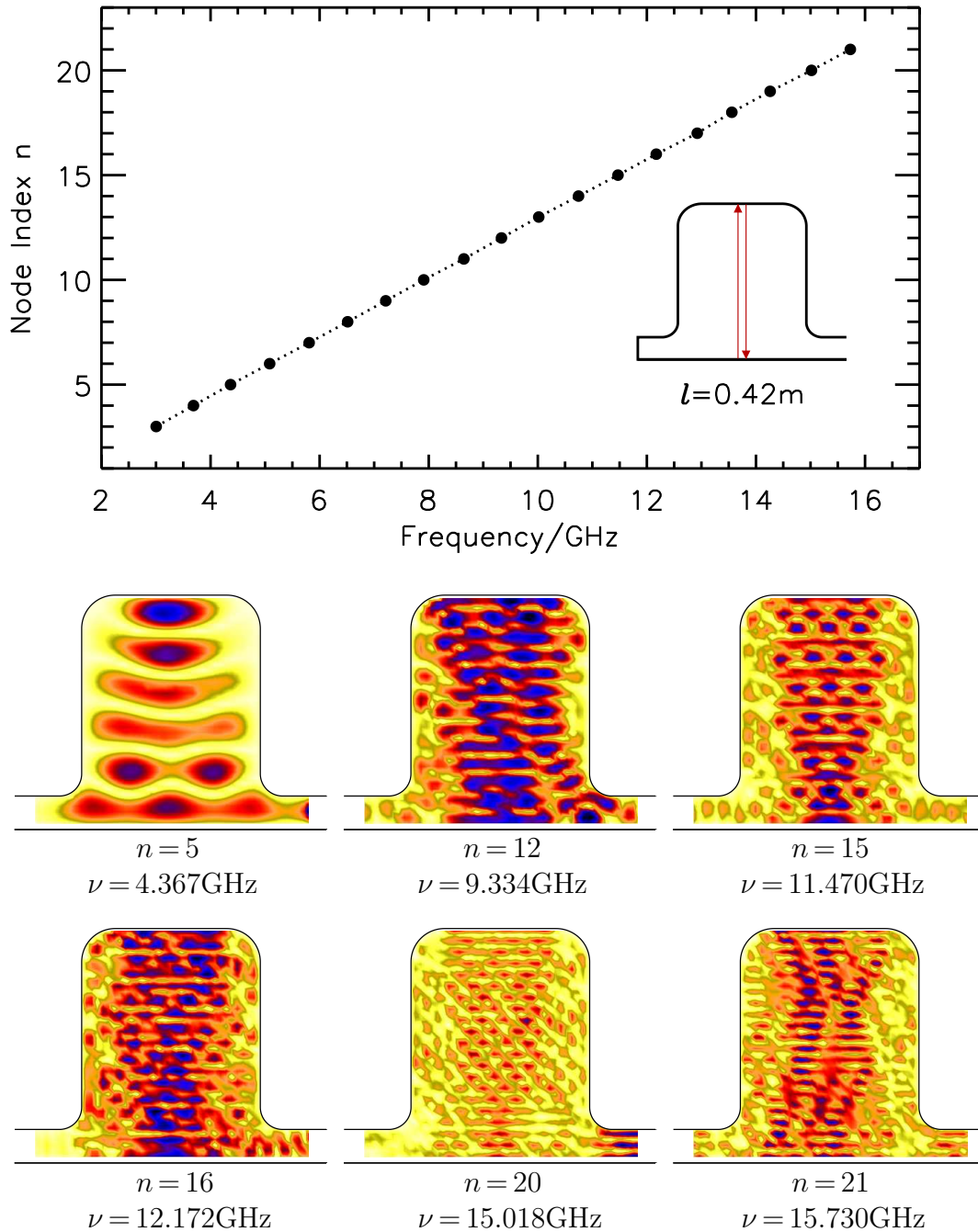


Figure 3.7: Eigenfrequencies at vertical bouncing ball scars (hard wall billiard). The measured frequencies at vertical bouncing ball wave functions are plotted in the upper panel and the typical member of the corresponding scar family.

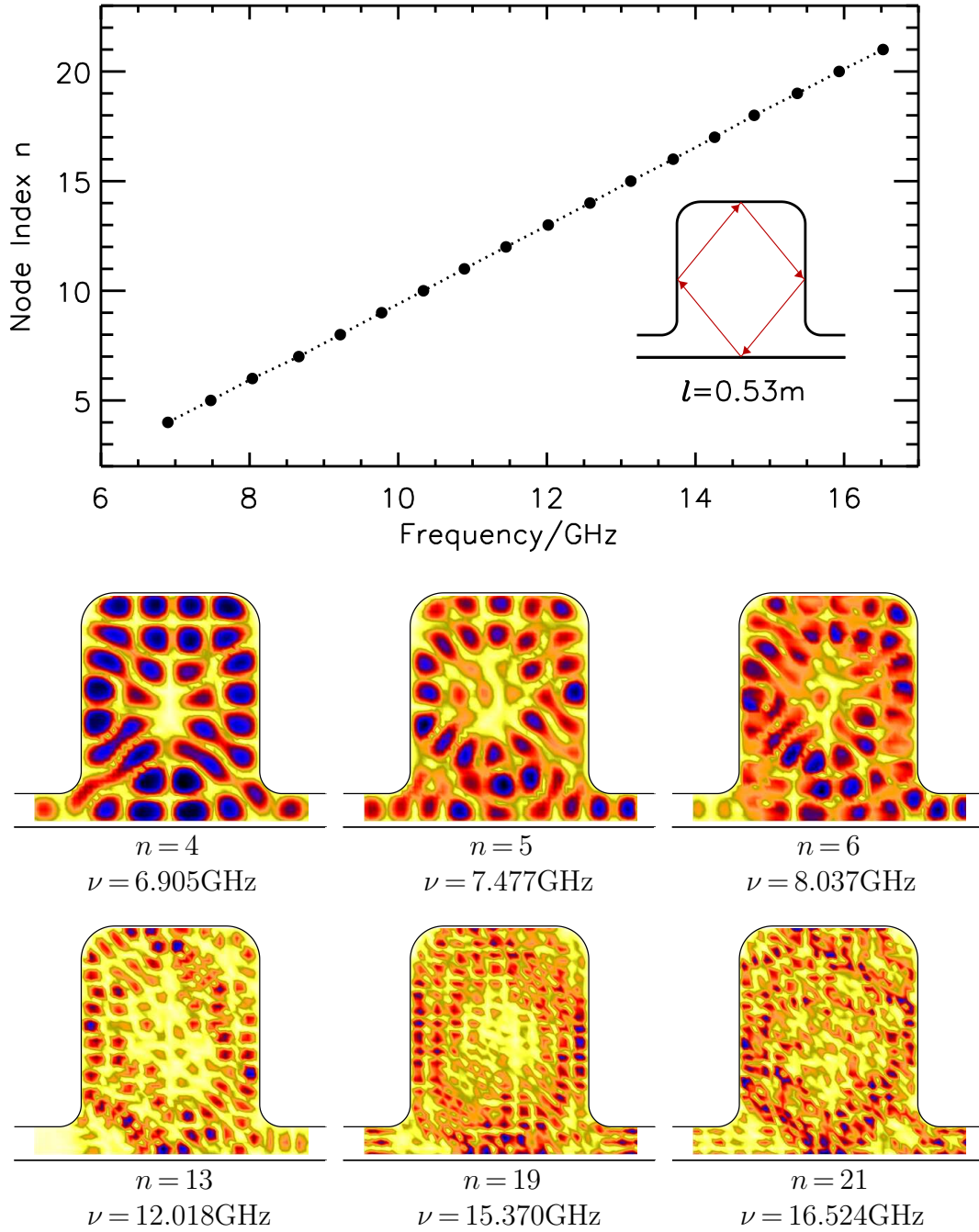


Figure 3.8: Eigenfrequencies at diamond-like scars (hard wall billiard)
 The measured frequencies at diamond-like wave functions are plotted in the upper panel and the typical member of the corresponding scar family.

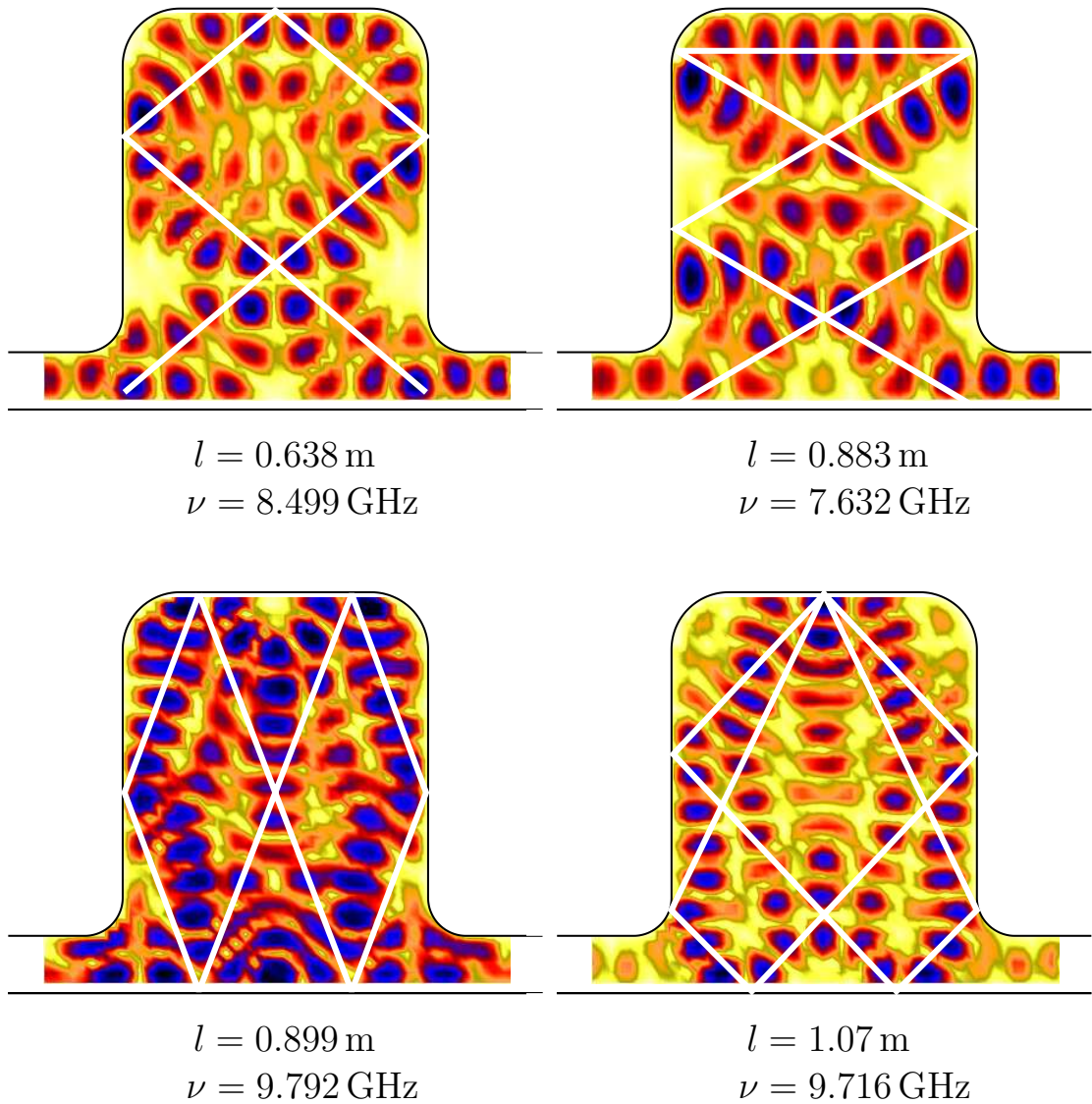


Figure 3.9: Complicated scar families
 Complicated recurred scars. Typical member of complicated recurred scars are plotted. Possible associated orbits are plotted with white lines.

3.2.3 Scanning Fourier spectroscopy

In this section, we study the influence of a movable absorber on the transmission properties, and the wave functions, of the same microwave cavity as in Figure 3.2 in section 3.2.1. In addition, we placed a disk like absorber with diameter of 1.5 cm and height of 8 mm at a fixed position in the billiard. Then we measured the S matrix as described in section 3.2.1. This measurement is illustrated in the left panel in Fig. 3.10 and was repeated for three different absorber positions. The red marked point is the probe antenna A_1 and the checkered circle presents the absorber. The absorber positions are plotted with black points in the right panel in Fig. 3.11. A second type of measurement is also shown in the right panel in Fig. 3.10, where we replaced the probe antenna A_1 by the absorber disk. Moving the absorber on a square grid of 5 mm, we measured the transmission between the input antenna A_2 in the right lead and the output antenna A_3 in the left lead.

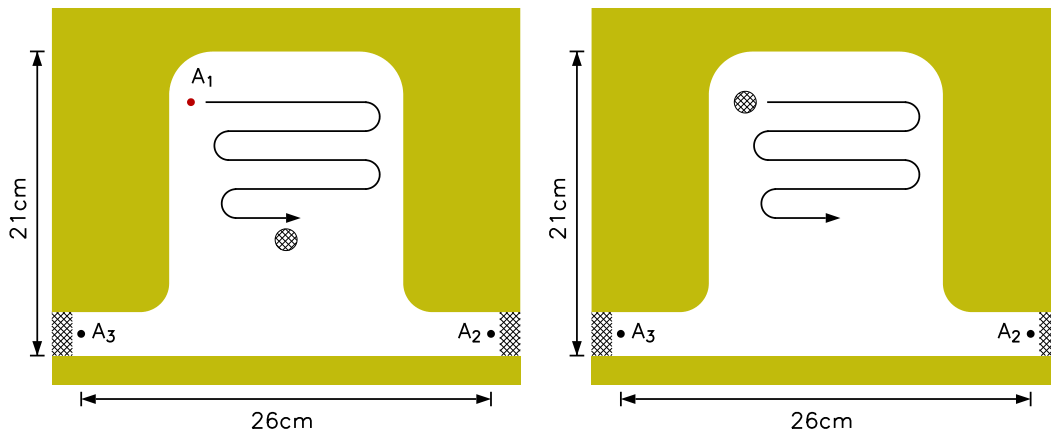


Figure 3.10: Sketch of the billiard scanning

Left: Scanning of the probe antenna A_1 with an absorber present, the reflection S_{11} and transmission S_{12} were measured. Right: Scanning of an absorber disk, transmission S_{32} between the waveguide leads was measured.

In Fig. 3.11, the transmission spectra $|S_{32}|$ for different fixed positions of the absorber disk are compared in the frequency range of 4.4 GHz - 4.9 GHz. One can see the influence of the absorber position on the microwave transmission through the cavity. In general, the transmission amplitudes are suppressed in the presence of the absorber in the case of b,c,d in the right panel in Fig. 3.11. Especially, the first and last resonance at 4.489 GHz and 4.808 GHz are strongly disrupted in cases b, c, d. The second resonance at 4.642 GHz is mostly disturbed in the case of c, and the third one at 4.677 GHz in d. We can understand this result better with Fig. 3.12 which shows the wave functions at each of the resonant

frequencies for the empty resonator and with the absorber located at three different positions. The columns correspond to the resonant frequencies 4.489 GHz, 4.642 GHz, 4.677 GHz, 4.808 GHz and the rows present the cases a, b, c, d. If the absorber position corresponds to local maxima of the original wave function without absorber, then the original wave function structure is destroyed or strongly distorted as seen at 4.489 GHz and 4.808 GHz while their patterns almost remain at 4.642 GHz and 4.677 GHz where the absorber is located closer to nodal lines in the original wave function.

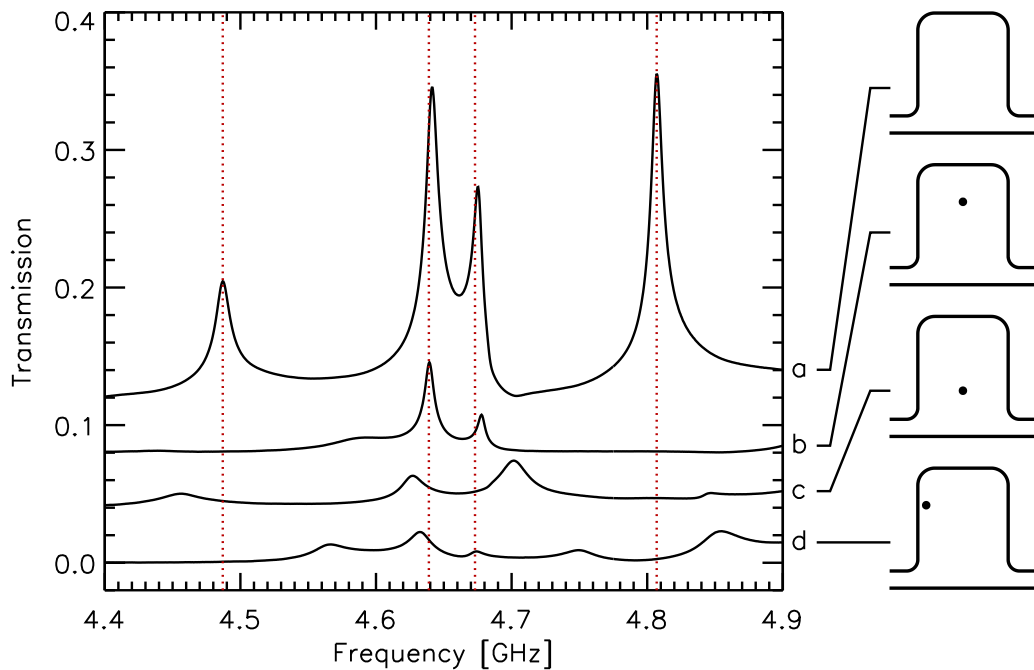


Figure 3.11: Transmission spectra $|S_{32}|$ with different absorber position. Typical isolated resonances (a) with no absorber present, (b)-(d) for three different absorber positions as shown in the right column. The spectra are shifted upwards by increments of 0.04.

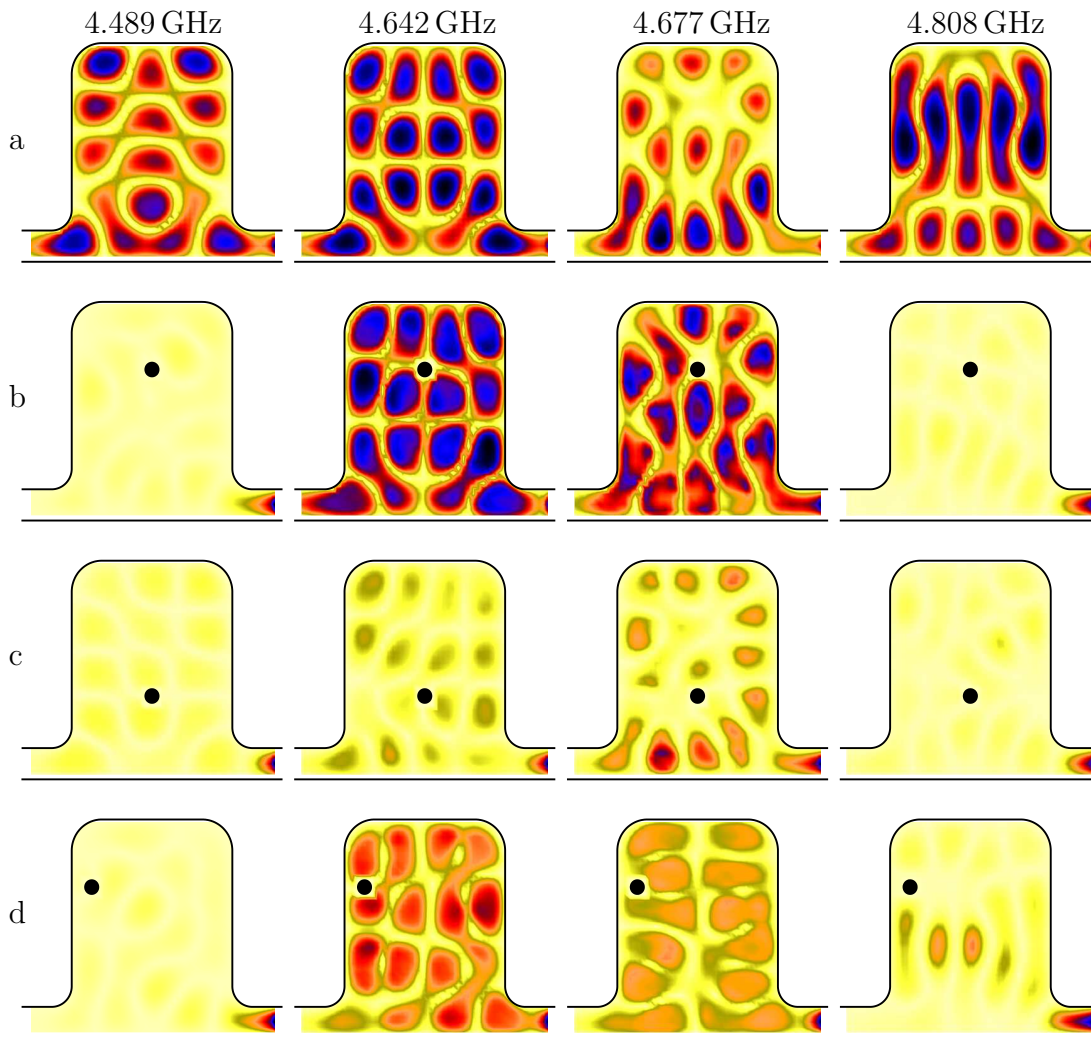


Figure 3.12: Wave function comparison for different absorber positions
Wave functions for the resonances shown in Fig. 3.11, with a absorber located at different positions.

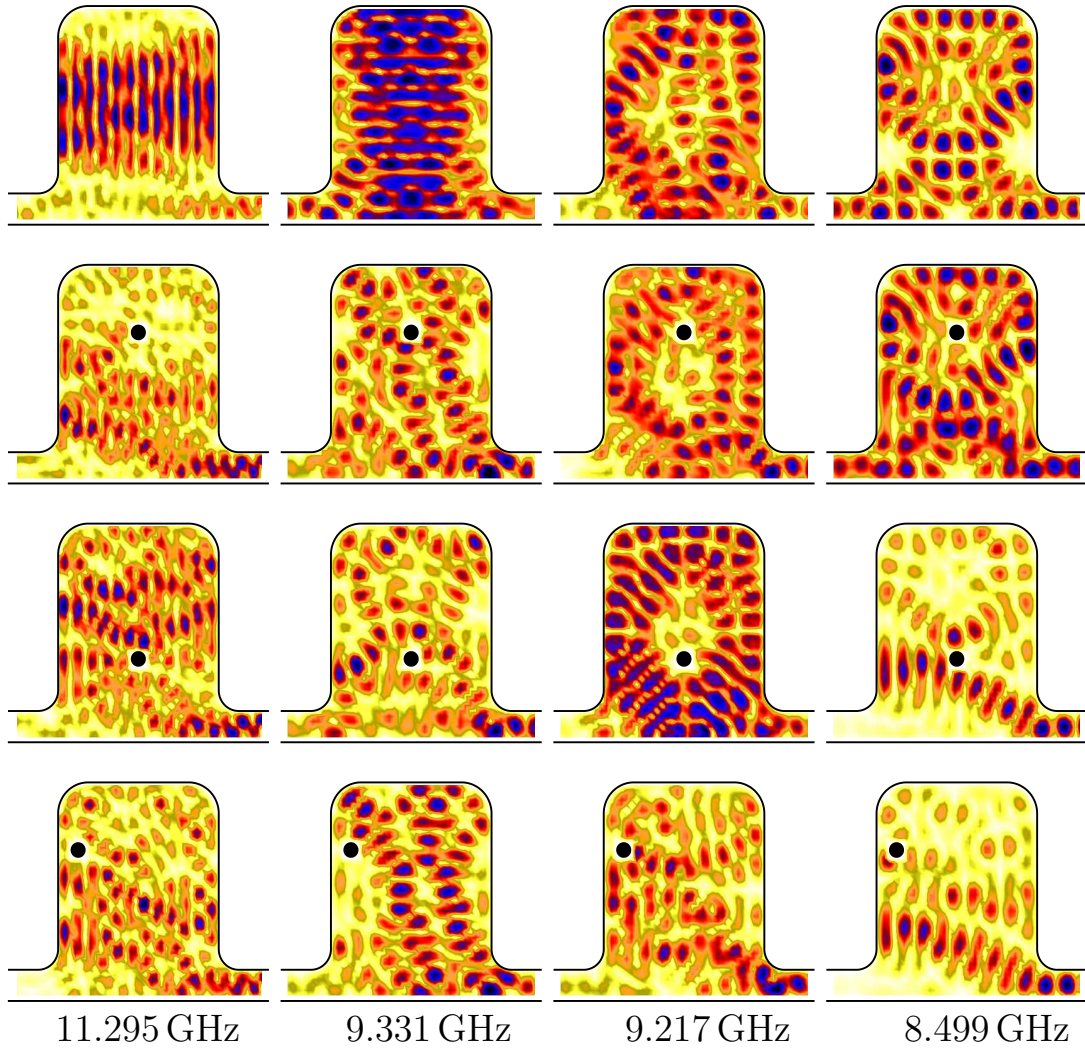


Figure 3.13: Wave functions for periodic orbits with an absorber

Wave functions for the horizontal and vertical bouncing-ball orbits, diamond-like scar and loop-like scar. In this frequency range, wavelength is comparable with the diameter of the absorber. Consequently the original wave function patterns are strongly destroyed by the absorber.

In Fig. 3.13, the scarred wave functions studied in the section 3.2.2 are plotted in the upper panel. The left column shows the absorber influence on the horizontal bouncing ball orbits. The vertical bouncing ball orbit is shown in the second column, and the diamond like trajectory and loop like trajectory are in the third and fourth columns, respectively. The resonant frequencies of these wave functions in Fig. 3.13 correspond to a half wavelength of 1.5 cm which is the diameter of the absorber. Therefore, the effect of the absorber is stronger than in Fig. 3.12 where the wave functions have a lower eigenfrequency. The main principle, however, is identical. Whenever the absorber is located closed to the scarred regions, the

original wave function pattern is strongly distorted. The loop like scar remains only when the impurity is placed in the center of the upper loop. In the horizontal bouncing ball scars, the bouncing ball structure remains regardless of where the absorber is placed though the wave functions are partly deformed.

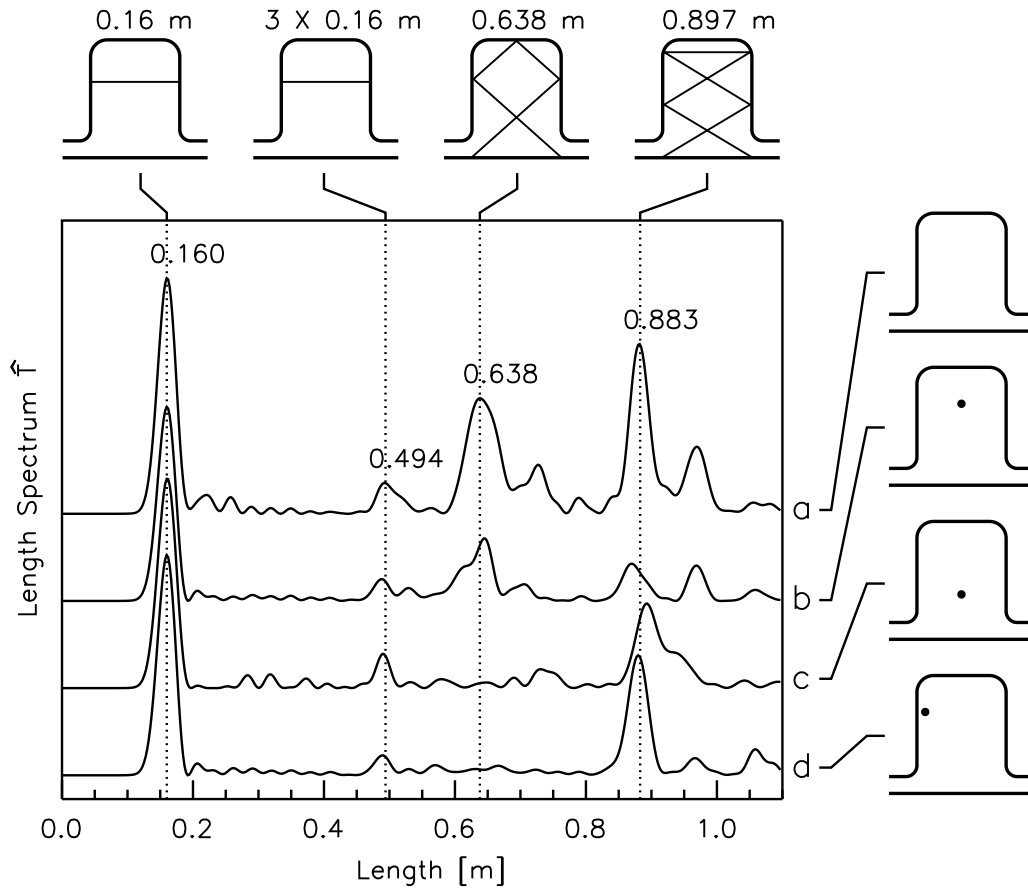


Figure 3.14: Length spectra with an absorber at different positions Length spectra by Fourier transform of the transmission spectrum of the clean cavity (a), (b)-(d) with the absorber located at three different positions. Each maximum corresponds to a trajectory connecting the entrance with the exit port. The spectra are shifted at the abscise by a constant

Semiclassical quantum mechanics yields the transmission amplitude

$$t(k) = \sum_j a_j e^{ikl_j}, \quad k = \frac{2\pi\nu}{c}, \quad (3.1)$$

as a sum over all classical trajectories j connecting the entrance and exit ports [Gut90]. Here, k is the wavenumber, ν is frequency, c is light velocity,

and l_j is the length of the classical trajectory j with (complex) stability factor a_j . By taking the Fourier transform of this expression, one can obtain the stability weighted length spectrum of the periodic orbits [Eck88, Stö99].

$$\hat{t}(l) = \frac{1}{2\pi} \int t(k) e^{-ikl} dk = \sum_j a_j \delta(l - l_j) \quad (3.2)$$

This equation allows a semiclassical interpretation of our results. Fig. 3.14 shows length spectra $\hat{T} = \hat{t}(l)^2$ from the transmission between the input and the output channels S_{32} . The peaks of the length spectra can be associated with classical trajectories. Some classical trajectories whose lengths are consistent with the major peaks in the Fourier spectra are also shown. As we have already mentioned, the absorber destroys the scarred wave function structure whenever it is placed close to the trajectory, whereas the resonance remains intact if the absorber is not on the orbit. Only small changes of the peaks of the length spectra which are associated with the horizontal bouncing ball orbits are observed with the absorber present in the cavity. The peaks for the loop-like orbit disappear when the absorber is at position c (under center) and d (off-center). The last orbit of the upper panel in Fig. 3.14 is suppressed when the absorber is placed in the upper center of the billiard b (upper center).

The results of Fig. 3.14 suggest a new type of experiment which we call scanning Fourier spectroscopy. As we described in the beginning of this section, we measured the transmission between the channels S_{32} with absorber present at each position within the billiard. In Fig. 3.15, the channel transmission $|S_{32}|$ is mapped out for the frequencies which are marked by dotted lines in Fig. 3.11. Dark color corresponds the maximum of $|S_{32}|$. When the absorber is placed on the dark region, it suppresses the channel transmission less than on the light region. This region corresponds to the nodal line of the original wave functions at these frequencies of the first row in Fig. 3.12 as we expected.

We repeated the Fourier transform defined in Eq. (3.2) for each transmission spectrum $|S_{32}|$ at each position and generated length dependent Fourier maps. We plotted the Fourier amplitude for each absorber position for fixed length. The selected Fourier maps are shown in the right panel in Fig. 3.16 and the associated classical orbits with corresponding scars wave function for billiard without absorber. Light regions indicate small, and dark regions correspond to large, amplitude. The associated classical trajectories are indicated with white lines. In the light region in the Fourier map, the absorber strongly suppresses the transmission amplitude, *i. e.* the absorber was placed close to the orbit whose length corresponds the length of the Fourier map. The associated classical orbits marked by white lines match very well with the light regions in the Fourier maps, even for the quite complicated trajectories with length 0.638 and 0.897 m. This result suggests the possibility of mapping out the wave function of a quantum dot

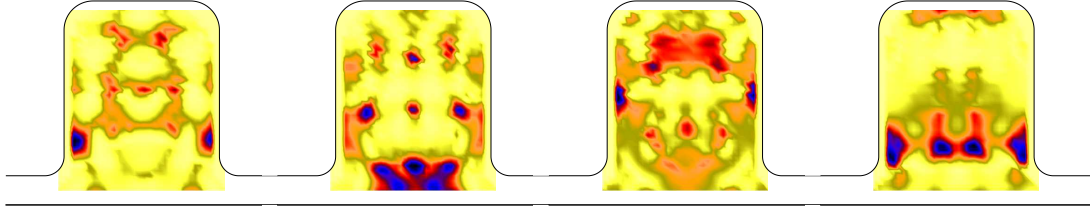


Figure 3.15: Channel transmission map $|S_{32}|$ with absorber scan. Channel transmission $|S_{32}|$ with absorber at each position within the billiard is plotted for 4.489, 4.642, 4.677 and 4.808 GHz. Dark color corresponds to the maximum. The absorber on the dark region suppresses the transmission less than on the light region. This region corresponds to the nodal line in the corresponding original wave function which is shown in Fig. 3.12.

in a scanning probe experiment, by monitoring the change in the conductance as a scanning probe is rastered over its area [Top01, Top00, Woo02]. According to Fig. 3.16, such an approach should allow one to identify the paths most relevant to transmission through a quantum dot.

In this section and the previous section 3.2.2, we studied periodically recurring scar families and possible associated trajectories that dominate transmission through the open microwave cavity. Some of these trajectories connect the input and output leads, as illustrated in Fig. 3.14 and Fig. 3.16 for the lengths 0.638 and 0.897 m, whereas other orbits are isolated from the channels like the vertical bouncing ball orbits with $l = 0.42$ m, the diamond-like orbits with $l = 0.53$ m. The latter ones do not show up as peaks in the Fourier transform, since they do not contribute to the transport, as might be expected from the usual semiclassical approximation. In the following section 3.3, however, we observe different properties in a microwave resonator with a soft wall potential, which are not expected in the classical case. A cross-like scar family shall be investigated as an evidence of dynamical tunneling.

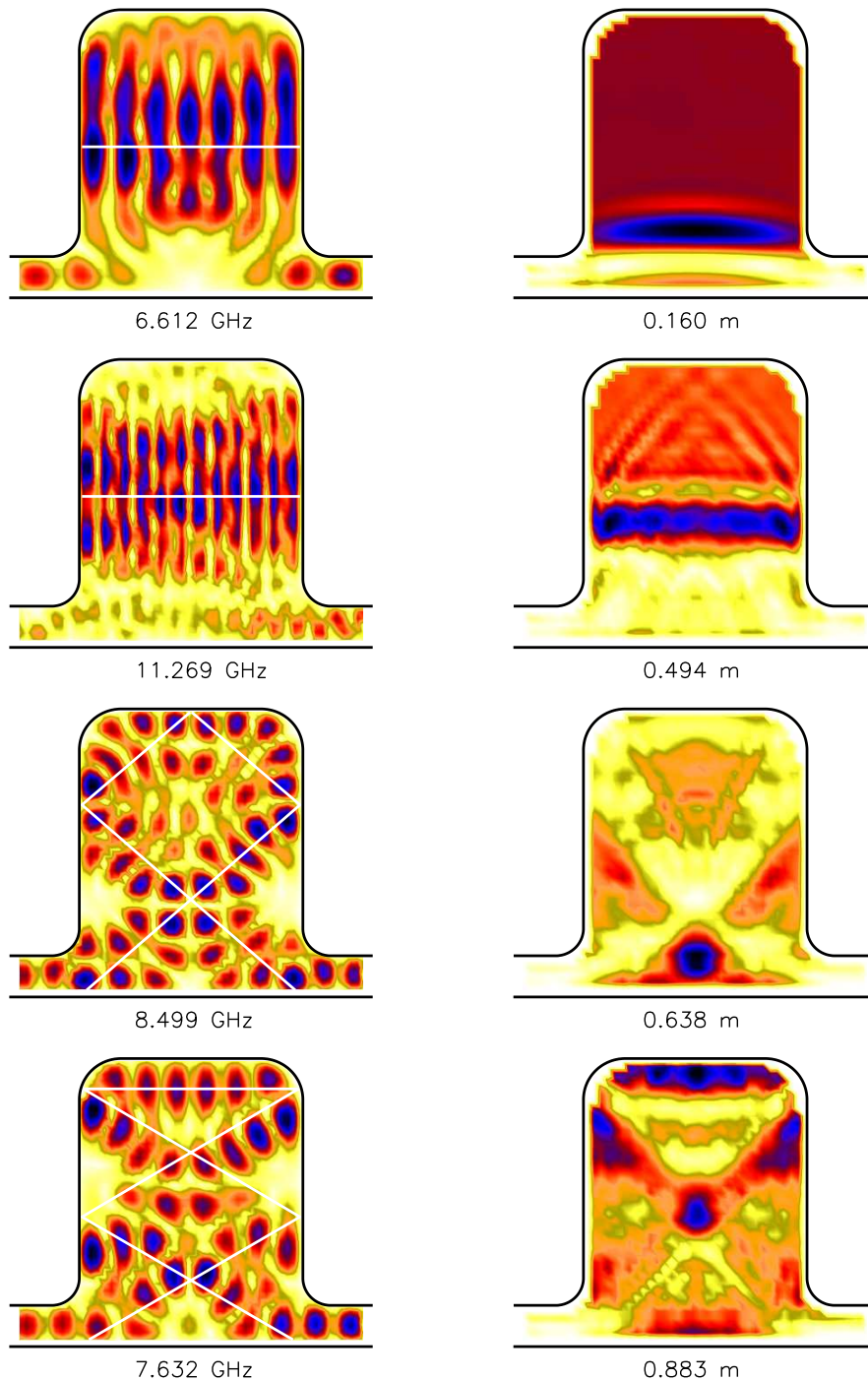


Figure 3.16: Classical trajectories and the Fourier maps

The left column shows selected classical trajectories with wave wave function obtained from $|S_{12}|$. The corresponding Fourier maps are illustrated in the right column. The Fourier maps are produced by Fourier transform of the transmission between the input and output channels S_{32} with the absorber scanning through the billiard. Small amplitudes are represented by light colors in the Fourier maps. They correspond to the classical trajectories. Details see text.

3.3 Soft-wall resonator

In this section, we shall present the results of an experiment on a microwave resonator with a soft-wall potential. There is already a study of a microwave experiment with soft-wall potential by Lauber [Lau94], where microwave experiments for a harmonic potential and a Hénon-Heiles potential were presented. They studied closed systems, however, and we shall study the transmission properties and the wave functions of an open microwave resonator with a soft-wall potential, simulating the typical structure of a quantum-dot potential. We compare the measured eigenvalues with those calculated from a WKB approximation. We present wave functions associated with certain periodic orbits as evidence for dynamical tunneling between two isolated islands [Mou02, Tom94, Tom01, Hen01, Ste01, Hel95] in phase space.

3.3.1 Experiment

The typical soft-wall potential of a quantum-dot [Bir95] is constant in the center, but increases quadratically close to the boundaries. The sketch of a quantum-dot and the corresponding contour of the potential are shown in Fig. 3.1. As we derived in Eq. (2.15), the correspondence between the potential and the height for TM mode $\theta = 1$ allowed us to realize the soft wall potential of a quantum-dot with a microwave resonator. The maximal height d_{max} and minimal height d_{min} of the resonator were 16.65 mm and 6.3 mm respectively. A photograph of the resonator used here is shown in Fig. 3.17(a). The resonator was produced by a computer-assisted milling machine in height steps of 0.1 mm, so that the shape of the potential of the resonator (see Eq. 3.5) was similar to the soft-wall potential of a quantum-dot. Fig. 3.17(b) shows the height profile where the z coordinate has been stretched by a factor of 10. The height profile along a horizontal cut and the corresponding potential are shown in Fig. 3.17(c) and Fig. 3.17(d) respectively. In the measurements, the top plate supporting the probe antenna A_1 was moved on a quadratic grid of side length 5mm, thus mapping out the field distribution within the resonator, just as in section 3.2.1. Since the top plate had to be moved in the experiment, and due to the imperfection in the mechanical treatment, the uncertainties in the height were about 0.9 mm. For frequencies ν below the minimal frequency $\nu_{min} = \frac{c}{2d_{max}} = 9$ GHz, only the TM-mode with $\theta = 0$ exists. Since the billiard is open in the $x - y$ plane, the $\theta = 0$ mode gives only rise to a smooth background, but not to sharp resonances. For frequencies with $\nu_{min} < \nu < \nu_{max} = \frac{c}{d_{max}} = 18$ GHz, the TM-mode with $\theta = 1$ can also exist. This is the frequency range of interest. For frequencies $\nu > \nu_{max}$, the modes with $\theta \geq 2$ can exist. Reflection S_{11} and transmission S_{12} were measured on a square grid of period 5 mm in the frequency range of 8.5 GHz-18 GHz in steps of 0.5 MHz. There

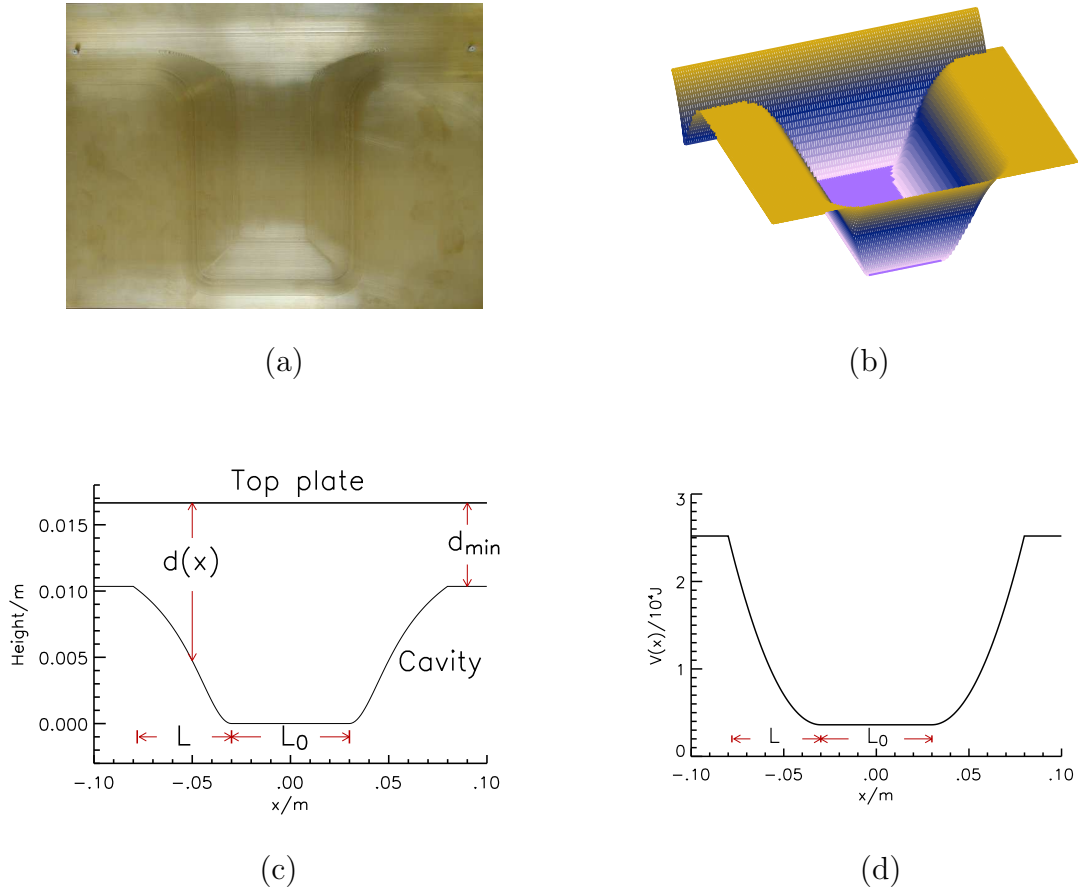


Figure 3.17: Structure of resonator and corresponding potential
 (a) Photograph of the resonator, (b) height profile, (c) horizontal cut of height profile, (d) profile of the corresponding soft-wall potential

was another frequency threshold $\nu_T = 12.5$ GHz of relevance. At this frequency, the attached channels open, *i. e.* below this frequency all states for $\theta = 1$ of the resonator are bound, whereas for higher frequencies the states extend into the leads and have thus to be interpreted as resonance states. In the upper panel in Fig. 3.18, the measured reflection $|\hat{S}_{11}|$ on the position of $(x, y) = (140, 125)$ mm and the corresponding channel transmission spectrum $|\hat{S}_{32}|$ are shown.

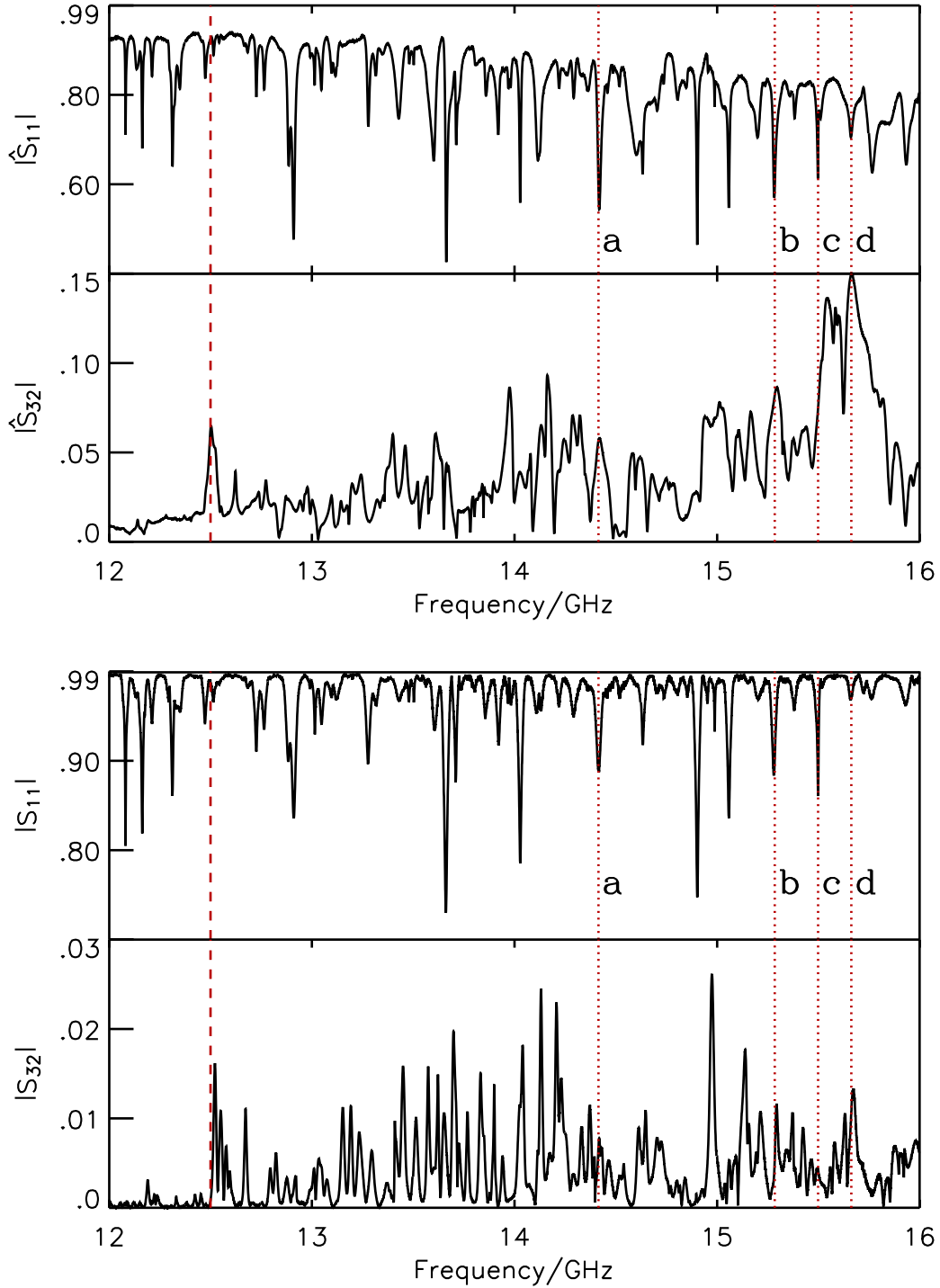


Figure 3.18: Measured reflection and transmission spectra of soft-wall resonator. Upper panel: the measured reflection spectrum $|\hat{S}_{11}|$ on the position of $(x, y) = (140, 125)$ mm and channel transmission spectrum $|\hat{S}_{32}|$. Lower panel: the corresponding spectra with correction $|S_{11}|$, $|S_{32}|$. Wave functions for the frequencies with dotted lines are shown in Fig. 3.20. The channel opening frequency $\nu_T = 12.5$ GHz is marked by a dashed line.

Due to the opening in the $x - y$ direction, only a part of the radiated microwave is coupled into the system, hence, the ground lines of the measured spectra (especially transmission spectrum) are not very clean. Subtracting the average value over 100 neighboring values, we removed this component from the measured spectra and plot the result in the lower panel in Fig. 3.18. The corresponding wave functions from the reflection $|S_{11}|$ and the transmission $|S_{12}|$ at the frequencies with the vertical dotted lines are illustrated in Fig. 3.20. At the threshold frequency ν_T marked by a dashed line in Fig. 3.18, the billiard states start to couple to the wave guides. Fitting the resonances below this frequency is easier than the resonances above ν_T . From the fit parameters α , β of Eq. (2.17), we could obtain the wave functions ψ . Wave functions $|\psi|^2$ are shown in Appendix A.

We compared the differently obtained wave functions at 12.743 GHz, 12.603 GHz, 12.630 GHz in Fig. 3.19. The upper panel shows the measured channel transmission $|\hat{S}_{32}|$ and the corrected transmission $|S_{32}|$ where the ground line is subtracted. In the lower panel, the corresponding wave functions are illustrated. The first row shows the fitted wave functions $|\psi|^2$. The measured transmission for this fixed frequency $|\hat{S}_{12}|$ is plotted in the second row. In the last row, the corrected transmission $|S_{12}|$ are shown. Without correction, the resonances are not clearly found in the plot of the \hat{S}_{32} in the upper panel, hence, the wave function structures are hardly recognized in the second row of the lower panel. After correction, the wave functions of $|S_{12}|$ are comparable with the fitted wave functions $|\psi|^2$. From now, we will use the fitted wave functions $|\psi|^2$ for the resonant frequencies which are below the threshold frequency $\nu_T = 12.5$ GHz or very strongly coupled resonances like the vertical and horizontal bouncing ball scar families. For other cases, the corrected transmission $|S_{12}|$ and reflection $|S_{11}|$ will be presented.

Fig. 3.20 shows members of the frequently recurring scar families. The resonant frequencies a, b, c, d are marked with dotted lines in Fig. 3.18. The left panel illustrates the wave functions of the reflection $|S_{11}|$. In the right panel, the corresponding transmission plots $|S_{12}|$ are shown. These three scar families, associated with the vertical bouncing ball orbits, horizontal bouncing ball orbits, as well as with a scar of the shape of the X-like-cross orbits, are most pronounced for the microwave resonator with the soft-wall potential. It is interesting to note the the X-like-cross structure was not observed on the hard wall resonator in section 3.2.2. Instead, we found scar families in the shape of a loop connecting input and output leads (see Fig 3.9). The cross-like scar family and bouncing ball scars are in more detail discussed in the next section 3.3.2 and 3.3.3.

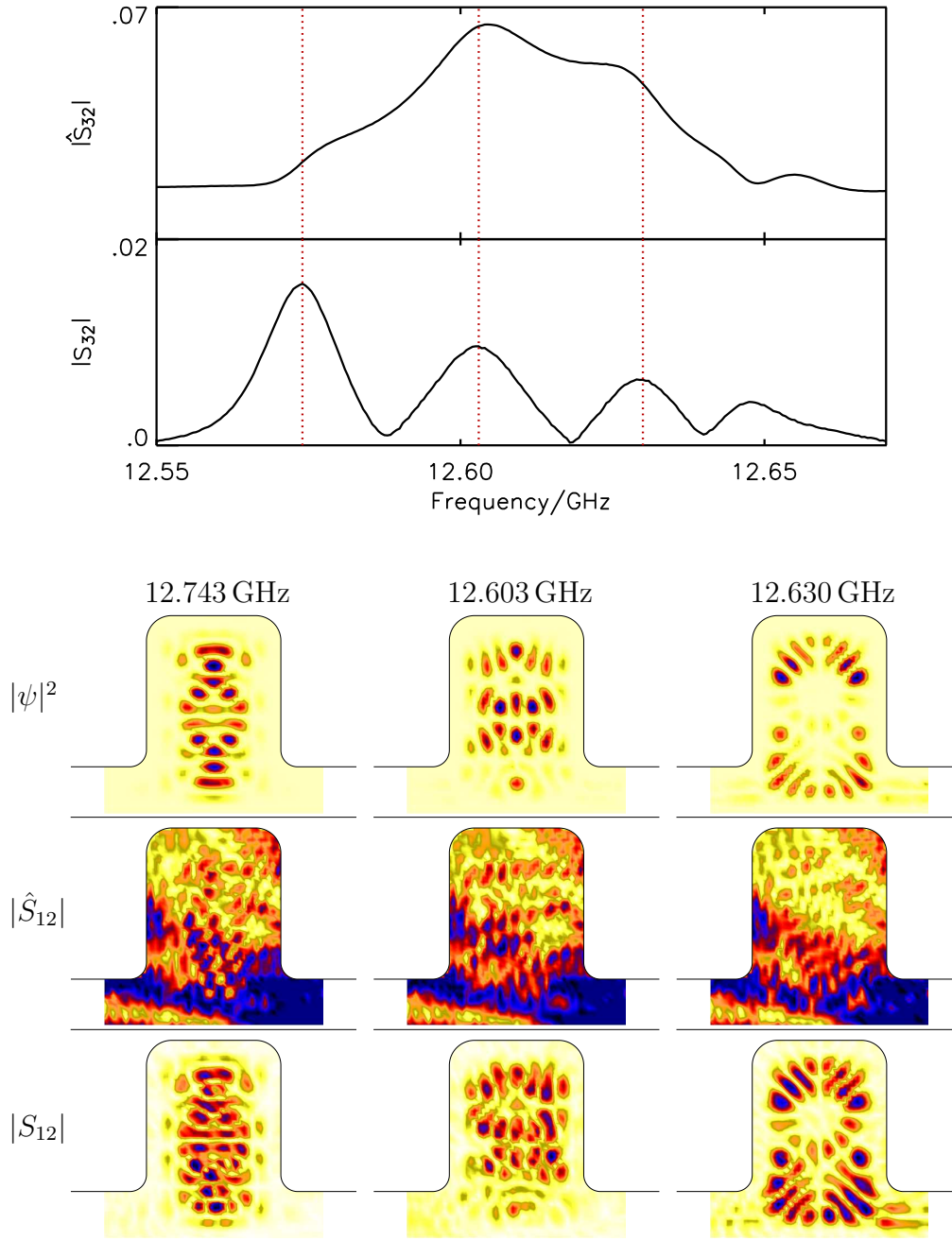


Figure 3.19: Comparison of selected wave functions

The measured transmission $|\hat{S}_{32}|$ and the corrected $|S_{32}|$ are plotted in the upper panel. In the lower panel, the first row shows the wave function $|\psi|$, plots of the measured transmission $|\hat{S}_{12}|$ in the second row, plots of the corrected transmission $|S_{12}|$ in the third row for the three different frequencies marked by dotted lines in the transmission spectra.

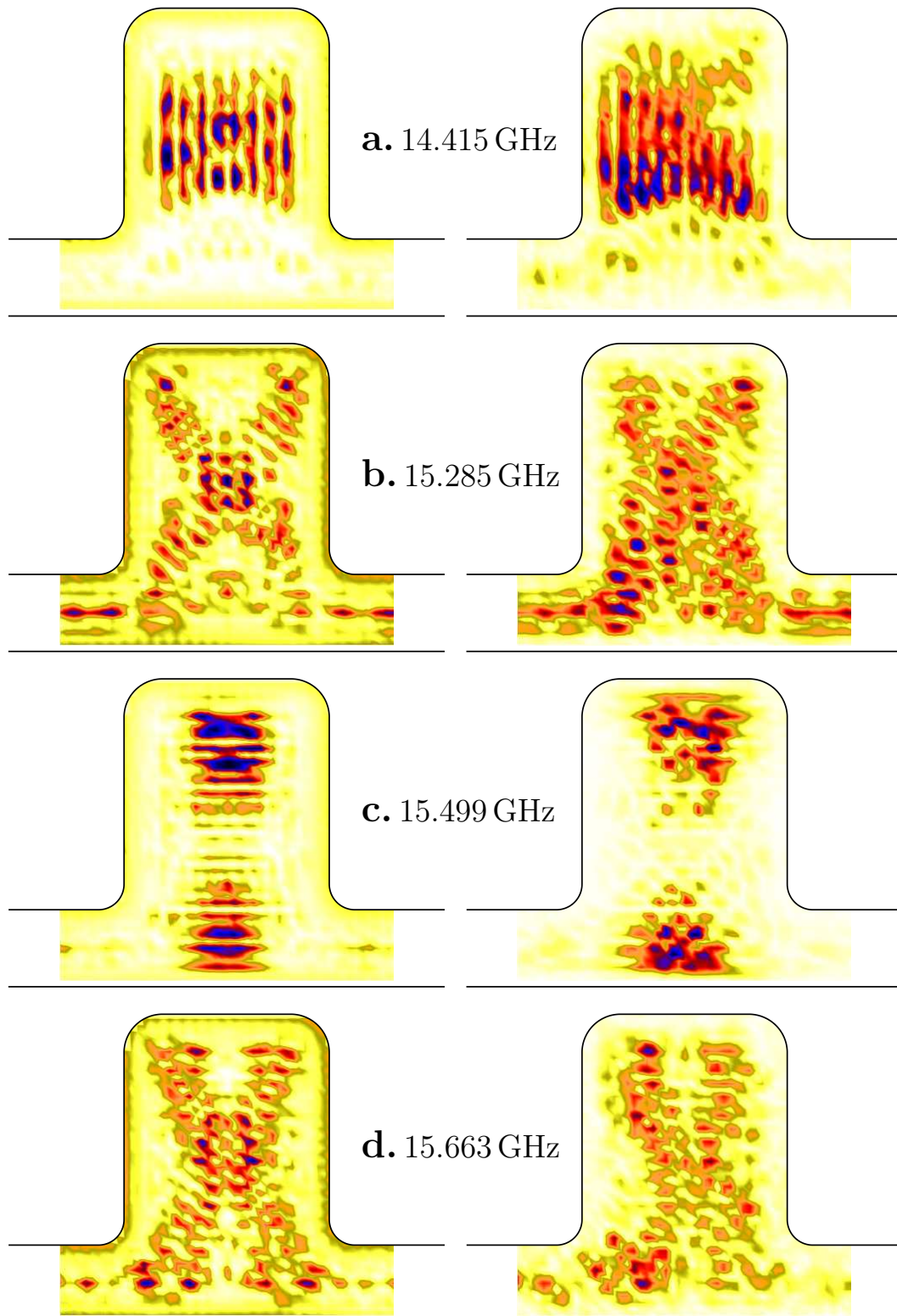


Figure 3.20: Selected wave functions of the soft-wall resonator. Corresponded reflection wave functions $|S_{11}|$ and transmission wave functions $|S_{12}|$ at the marked frequencies in Fig. 3.18.

3.3.2 WKB approximation

In the semi-classical case, we expect the wave function can be characterized by position dependent wave numbers. We can decompose the wave function into an amplitude factor $A(q)$ and a phase factor $S(q)$ for a one-dimensional system

$$\psi(q) = A(q)e^{\frac{i}{\hbar}S(q)}. \quad (3.3)$$

Eigenenergies $E_n \sim \nu_n^2$ of the members of the three scar families, associated with the vertical bouncing ball orbits, horizontal bouncing ball orbits, the X-like-cross orbits from Fig. 3.20 can be calculated semiclassically by means of a WKB approximation (after Wentzel, Kramer, Brillouin, details in Appendix B). In a one-dimensional system with two classical turning points q_1, q_2 , the action S is quantized according to

$$S_n = 2 \int_{q_1}^{q_2} p dq = 2 \int_{q_1}^{q_2} \sqrt{2m(E_n - V(q))} dq = 2\pi\hbar \left(n + \frac{1}{2} \right). \quad (3.4)$$

This gives an implicit expression for the eigenenergy E_n of the n th state. Eq. 3.4 may be directly applied to the scarred structures observed in the experiment. For the two bouncing-ball families, a one-dimensional treatment is obviously justified, and the cross-like structure may be looked upon as a superposition of two one-dimensional structures oriented along the diagonal of the billiard. For the cross-like structures, the application of the WKB approximation is somewhat questionable above 12.5 GHz where the states start to extend into the wave guides, but we shall see that this leads only to small deviations. The one-dimensional potential to be inserted into Eq. 3.4 is given by (see Fig. 3.17)

$$V(q) = \begin{cases} \left(\frac{\hbar\pi}{\sqrt{2md_{\max}}} \right)^2, & |q| \leq \frac{L_0}{2} \\ \frac{1}{2}\omega^2(|q| - \frac{L_0}{2})^2 + V_{\min}, & \frac{L_0}{2} < |q| < \frac{L_0}{2} + L \\ \left(\frac{\hbar\pi}{\sqrt{2md_{\min}}} \right)^2, & \frac{L_0}{2} + L < |q| \end{cases} \quad (3.5)$$

where $\omega = \sqrt{\left(\frac{1}{d_{\min}}^2 - \frac{1}{d_{\max}}^2\right) \frac{\hbar\pi}{\sqrt{2mL}}}$, $L = 50$ mm for all three cases, and $L_0 = 60$ mm, 140 mm, 152 mm for the vertical, horizontal, and cross-like bouncing-ball structures. Inserting expression (3.5) for $V(q)$ into equation (3.4) and performing the integration we get

$$n = \frac{2\hbar\pi^2}{mc^2\omega} \nu_n^2 + \frac{L_0}{2c} \sqrt{4\nu_n^2 - \nu_{\max}^2} - \frac{\hbar\pi^2}{8mc^2\omega} \nu_{\max}^2 - \frac{1}{2} \quad (3.6)$$

where ν_n is the eigenfrequency of the n th state. The calculated eigenfrequencies and measured eigenfrequencies for the vertical bouncing-ball, the horizontal

bouncing-ball and the cross-like bouncing-ball scarred wave functions are plotted in Fig. 3.21 to 3.23 respectively. Stars indicate the calculated values and diamonds the experimentally-identified values. The lower panels show a set of corresponding wave functions $|\psi|^2$. The deviations of experimental values are likely to be caused by imperfections and a possible misalignment of the top plate changing the potential slightly. The deviations are somewhat larger above 12.5 GHz where the states start to extend into the wave guides because we used the WKB approximation for bound states. The greater the contribution to transport of the trajectory the more influence we expect of the channel opening on the deviation. Therefore the deviations for the cross-like structures are largest above the channel opening frequency ν_T . However they are still small enough that we can find overall very good agreement of the experimental results with the predicted theoretical values.

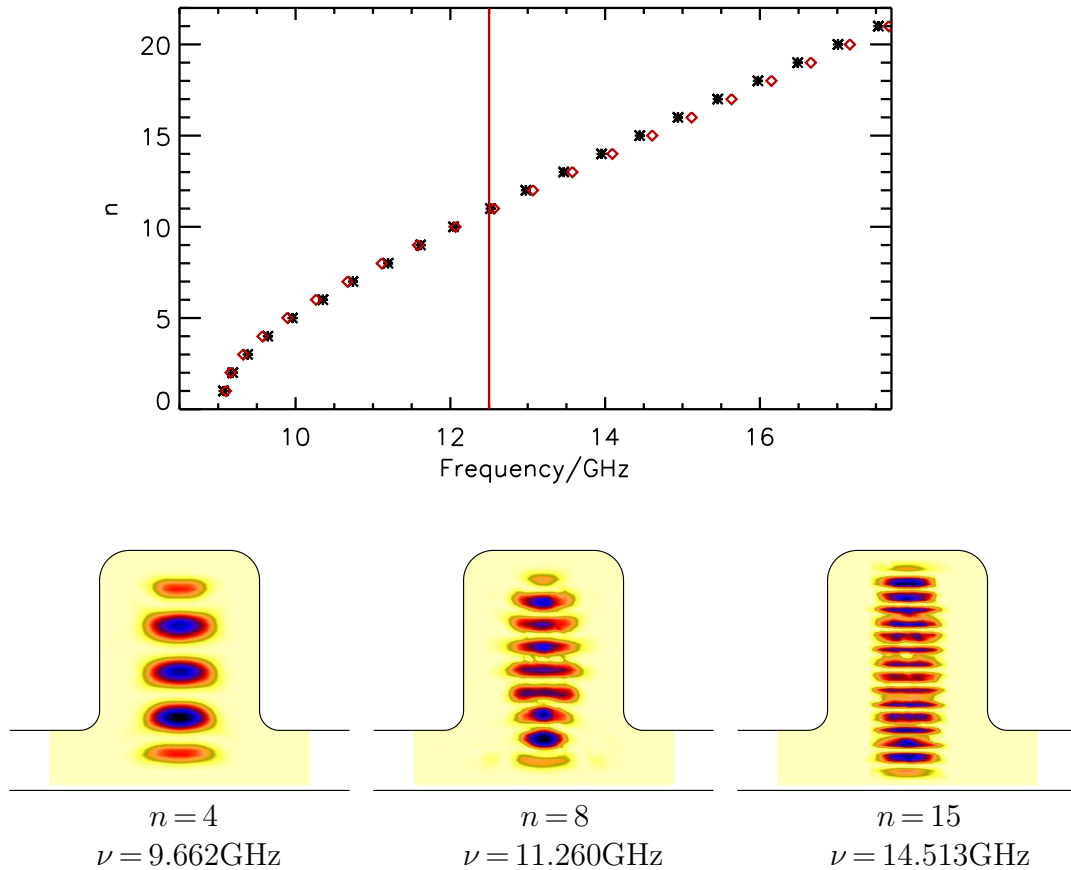


Figure 3.21: Vertical bouncing-ball scarred wave functions
 Calculated values are plotted with diamonds and measured values are plotted with stars. The solid line indicates the channel opening frequency $\nu_T = 12.5$ GHz.

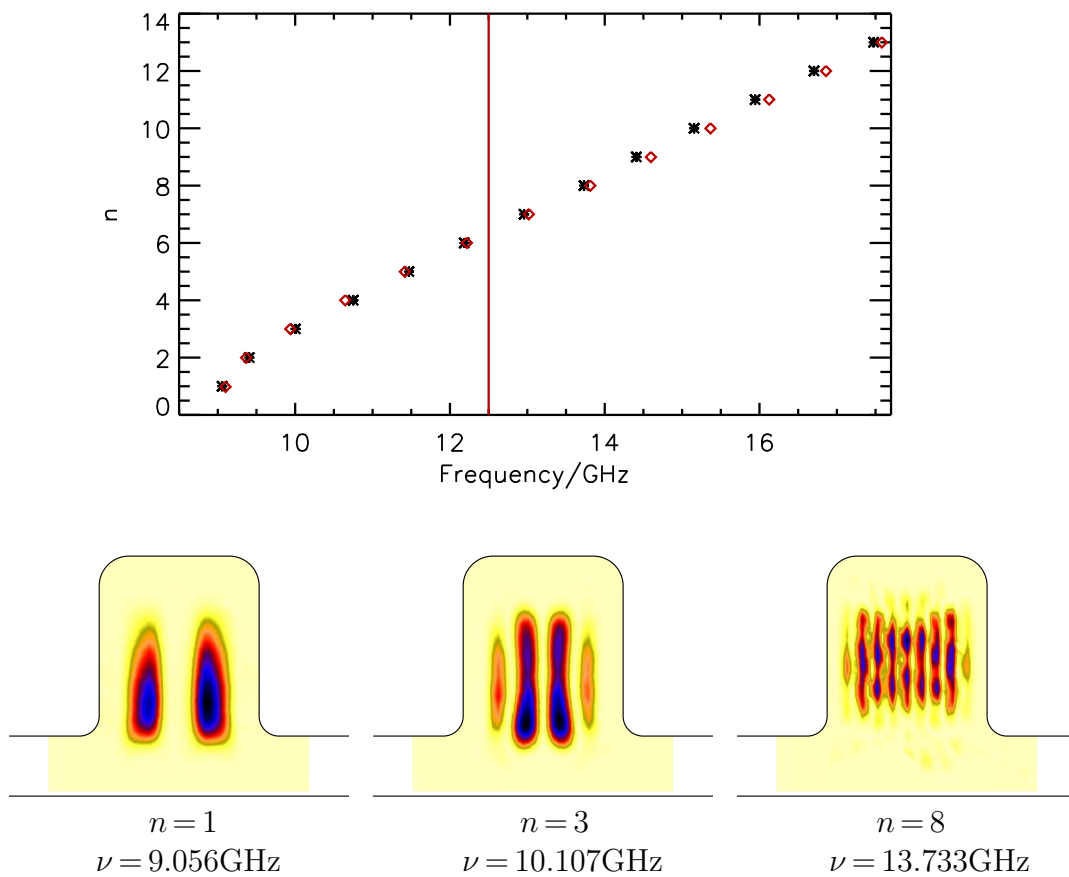


Figure 3.22: Horizontal bouncing-ball scarred wave functions
 Calculated values are plotted with diamonds and measured values are plotted with stars. The solid line indicates the channel opening frequency $\nu_T = 12.5$ GHz.

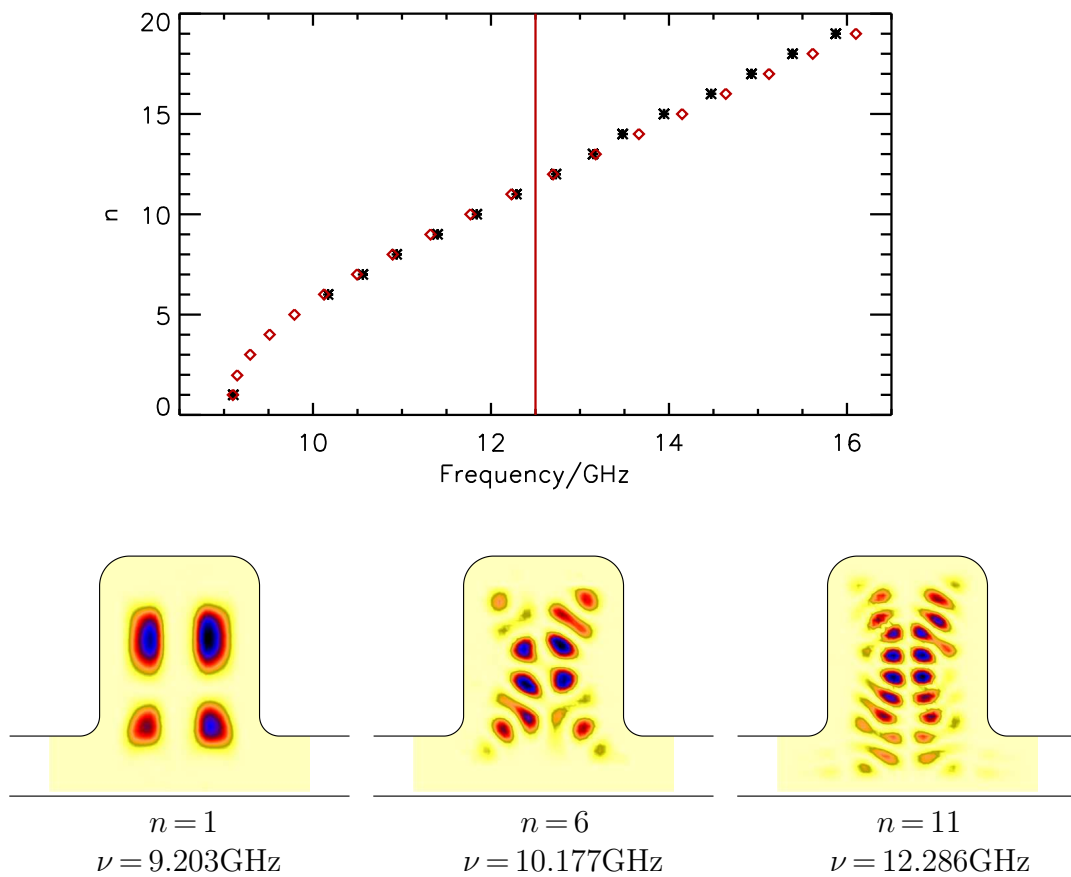


Figure 3.23: Cross bouncing-ball scarred wave functions
 Calculated values are plotted with diamonds and measured values are plotted with stars. The solid line indicates the channel opening frequency $\nu_T = 12.5$ GHz.

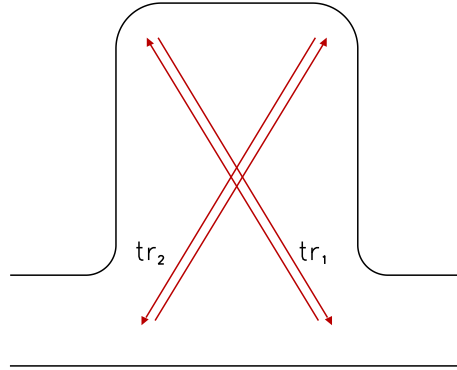


Figure 3.24: Cross-like scarred wave function

Cross-like orbit is an independent superposition of two diagonal bouncing ball orbits tr_1 , tr_2 . Classically such orbits do not contribute to transport between the leads.

3.3.3 Dynamical tunneling

Quantum mechanical tunneling involves an allowed quantum event which is classically forbidden. Dynamical tunneling is the subset of such events which do not involve a classically insurmountable potential barrier through which to tunnel in the traditional sense. The dynamical tunneling occurs between two distinct classically trapped regions in phase space. Semiclassically, we can consider the cross-like structure as an independent superposition of two one dimensional trajectories tr_1 , tr_2 oriented along the diagonals. Each of these structures corresponds classically to a particle that is injected from one side, following the diagonal trajectory, being reflected from the upper corner and leaving the billiard through the entrance wave guide (see Fig. 3.24). To use the terms introduced by E.J. Heller [Dav81, Hel95], the pair of “clean” states ψ_1, ψ_2 , oriented along to the diagonal are degraded by their tunneling interaction into the “dirty” cross-like states ψ_s, ψ_u with

$$\psi_s = c_{s1}\psi_1 + c_{s2}\psi_2 \quad (3.7)$$

$$\psi_u = c_{u1}\psi_1 + c_{u2}\psi_2 \quad (3.8)$$

where $c_{s1} = c_{s2} = c_{u1} = \frac{1}{\sqrt{2}}$, $c_{u2} = -\frac{1}{\sqrt{2}}$. The wave functions calculated by M.J. Davis and E.J. Heller are plotted in Fig. 3.25.

The magnitudes of these coefficients are all equal because of the symmetry of potential from Eq. 3.5 around $x = 0$. Without dynamical tunneling, we could not explain the contribution of the cross-like states to the transport between the input and output leads which is clearly shown in Fig. 3.18. If the symmetry of

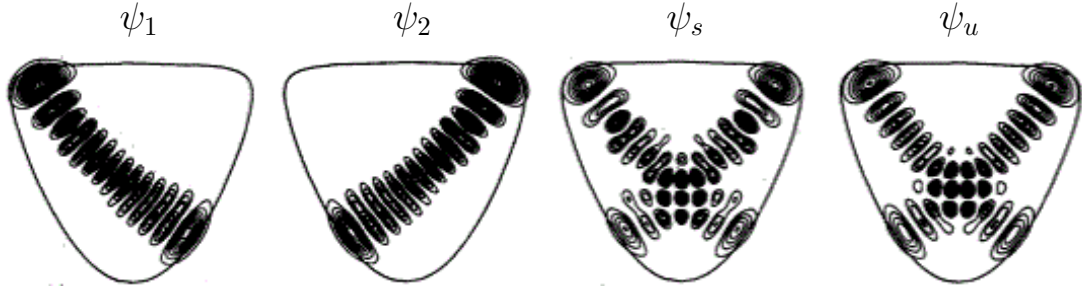


Figure 3.25: Clean and Dirty states

The clean states (two uncoupled single states) ψ_1, ψ_2 and the dirty states (symmetrically and anti-symmetrically coupled states) ψ_s, ψ_u with $\psi_s = \frac{1}{\sqrt{2}}(\psi_1 + \psi_2)$, $\psi_u = \frac{1}{\sqrt{2}}(\psi_1 - \psi_2)$. These are calculated by M.J. Davis and E.J. Heller [Dav81]

the potential is broken enough we should expect eigenstates with $|c_{s1}| \neq |c_{s2}|$ and $|c_{u1}| \neq |c_{u2}|$ resulting in a reduction of the dynamical tunneling [Dav81, Hel95]. In those cases, one of the two single states dominate the coupled state. Such cases are shown in Fig. 3.26. In our experiment, the symmetry of the potential was broken due to the imperfections and a possible misalignment of the top plate. Thanks to that, however, we could observe the cases for which $|c_{s1}| \neq |c_{s2}|$ and $|c_{u1}| \neq |c_{u2}|$. The comparable experimental cases are shown in Fig. 3.29.

The case of (a) in Fig. 3.29 shows an eigenstate dominated by $\psi_1 \equiv tr_1$ and in the case of (c), dominated by $\psi_2 \equiv tr_2$.

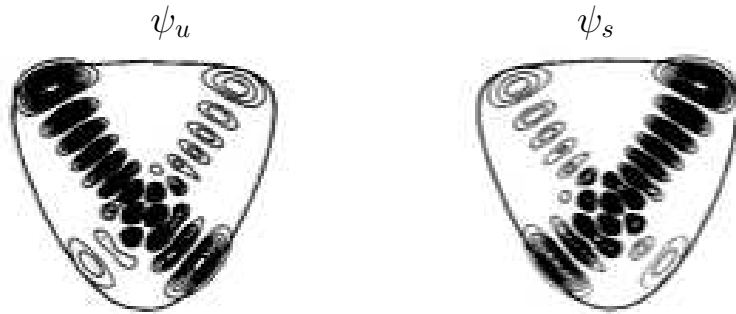


Figure 3.26: Dirty states by breaking the symmetry of potential

The differently coupled states $\psi_u = c_{u1}\psi_1 + c_{u2}\psi_2$, $\psi_s = c_{s1}\psi_1 + c_{s2}\psi_2$ with $|c_{u1}| \gg |c_{u2}|$ and $|c_{s1}| \ll |c_{s2}|$. These are calculated by M.J. Davis and E.J. Heller [Dav81]

We found one more evidence of the existence of the dynamical tunneling at the

cross-like orbits. If the cross-like orbits consisted of a single state, there would be no change from the symmetric state ψ_s to the antisymmetric state ψ_u through the resonance frequency. This is a direct evidence of dynamical tunneling discussed in a number of papers [Mou02, Tom94, Tom01, Hen01, Ste01, Hel95]. We calculated the phase of measurements ϕ with $S_{12} = |S_{12}|e^{i\phi}$. Theoretically the modulus of phase differences of two symmetrical positions to the y-axis

$$\Delta\phi = |\phi(x, y) - \phi(-x, y)| \quad (3.9)$$

should be 0 for the symmetric case and π for the antisymmetric case. In our experiment, noise sources obscure the observation of the symmetric $\Delta\phi = 0$ or antisymmetric $\Delta\phi = \pi$ states. Instead, cases where $\Delta\phi < \frac{\pi}{2}$ are considered as symmetric and those where $\Delta\phi > \frac{\pi}{2}$ as antisymmetric. In Fig. 3.27, the mean value of the phase difference over the measured area $\langle\Delta\phi\rangle_{(x,y)}$ is plotted in the range of 11.3 – 13.6 GHz and the frequencies of the cross-like orbits with quantum number $n = 9, 10, 11, 12, 13, 14$ are marked by dotted lines. A change of the phase difference from the symmetric state ($\Delta\phi < \frac{\pi}{2}$) to the antisymmetric state ($\Delta\phi > \frac{\pi}{2}$) is observed around every resonant frequency. For demonstration,

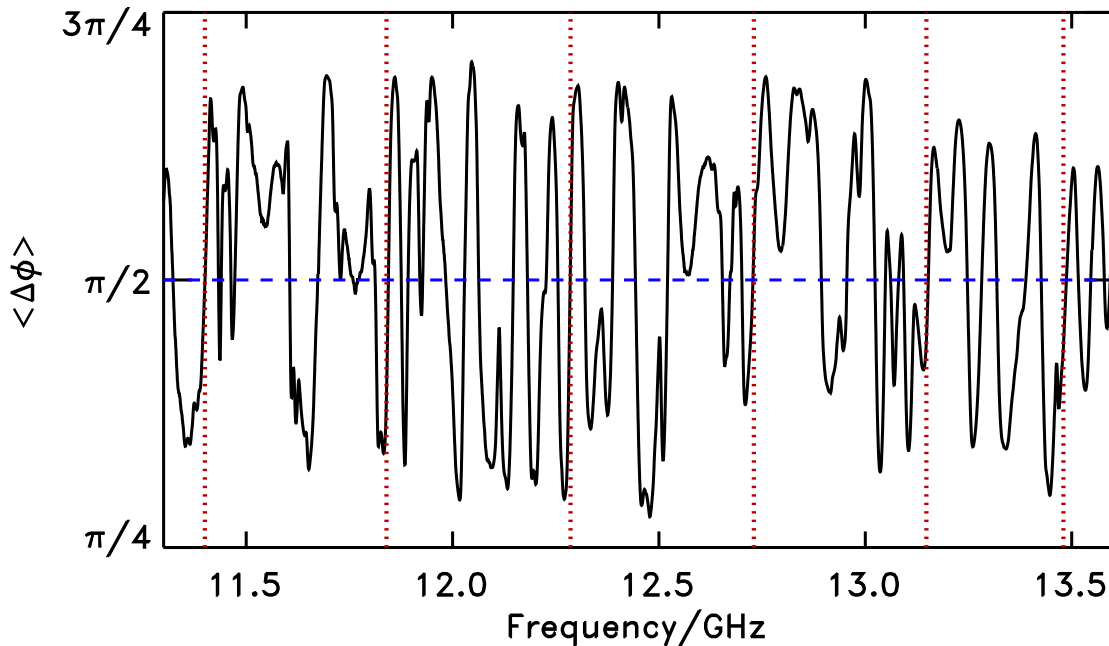


Figure 3.27: Mean value of the phase difference over the measured area $\langle\Delta\phi\rangle_{(x,y)}$. The mean value of the phase difference $\langle\Delta\phi\rangle_{(x,y)}$ vs frequency is plotted. The frequencies for the cross-like orbits are marked by dotted lines.

we chose a typical cross-like wave function at $\nu = 15.285$ GHz. In the first row and second row in Fig. 3.28, the reflection and transmission $|S_{11}|$, $|S_{32}|$ are shown

in the frequency range of 15.25 – 15.33 GHz, respectively. The mean value of the corresponding phase difference over the measured area $\langle \Delta\phi \rangle_{(x,y)}$ is plotted in the last row. The three dotted lines a, b, c indicate three different frequencies 15.278 (below the resonance), 15.285 (the resonance case), 15.295 GHz (above the resonance) which are also used for the phase maps and intensity plots in Fig. 3.29. The corresponding phase distributions ϕ are plotted in the third row. Black for $\phi < 0$ and white for $\phi > 0$ are used in the phase map. The corresponding wave functions from reflection $|S_{11}|$ and transmission $|S_{12}|$ are shown in the first and second row in Fig. 3.29, respectively. A phase difference changing from the symmetric state to the antisymmetric state is also found around this state in Fig. 3.28, the phase map is symmetric below the resonance frequency and antisymmetric above the resonance frequency (see the lowest panel in Fig. 3.29).

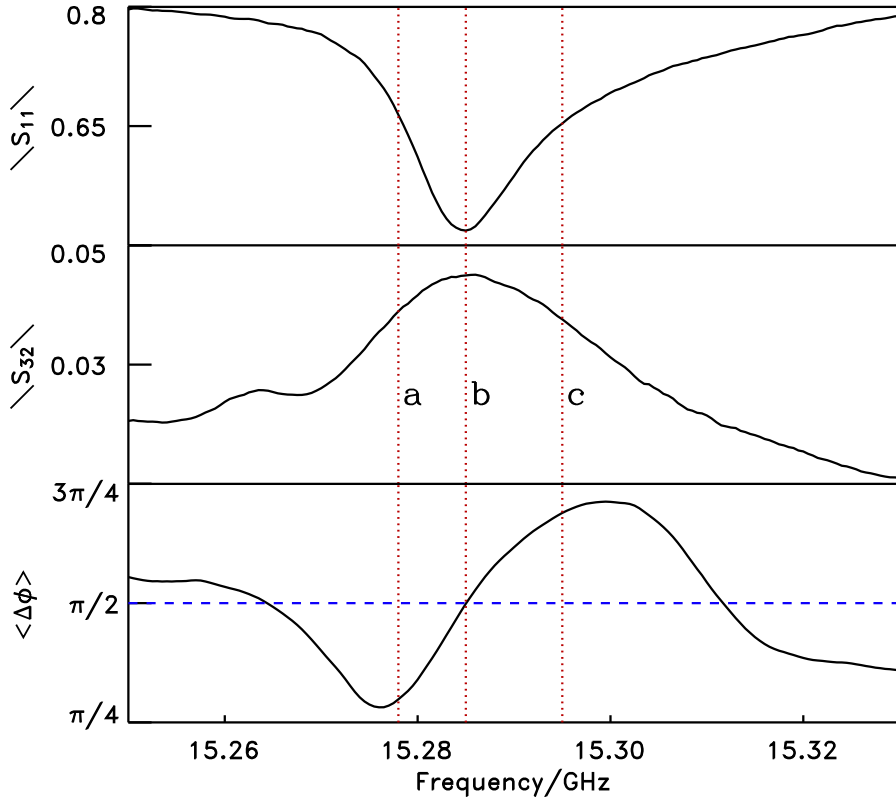


Figure 3.28: Spectrum $|S_{11}|$, $|S_{32}|$ and phase difference at 15.285 GHz

The reflection spectrum $|S_{11}|$ (first row) at a position in the billiard $(x, y) = (140, 125)$ mm and transmission spectrum $|S_{32}|$ between the input and output channels (second row) and the mean value of the phase difference $\langle \Delta\phi \rangle_{(x,y)}$ vs frequency (third row) are plotted. The wave functions and phase maps for the frequencies marked by dotted lines are shown in Fig. 3.29.

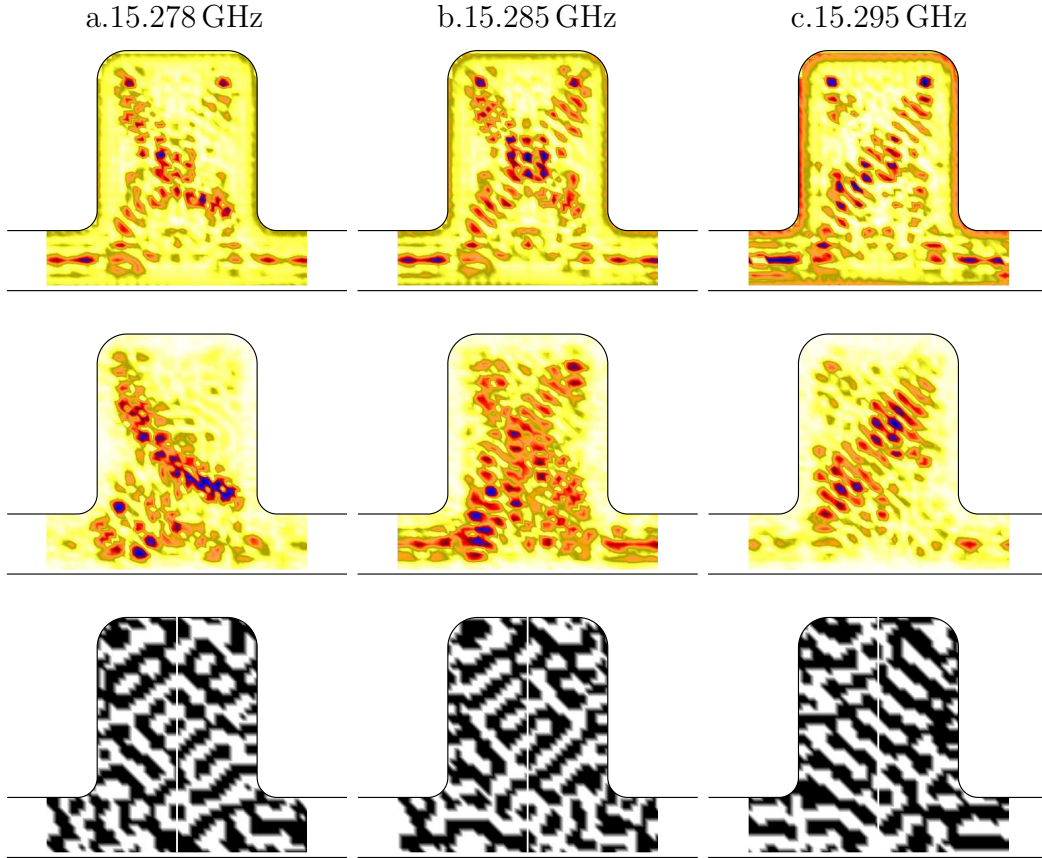


Figure 3.29: Typical cross bouncing-ball scar near 15.285 GHz
 The first row shows $|S_{11}|$, the second row shows $|S_{12}|$. The third panel presents the phase maps ϕ in black for negative values and white for positive values.

In this section, we dealt with three dominating bouncing-ball scar families. First we found very good agreement of experiment with the theoretical prediction from a WKB approximation for one dimensional systems. The contribution of the cross-like scar family as a pair of two separated diagonal bouncing ball orbits showed evidence of dynamical tunneling. The observed changes of the phase difference near the resonant frequencies of this scar family strongly supported the existence of dynamical tunneling.

3.3.4 Outlook

After this first attempt with a open soft-walled microwave resonator, we can extend the microwave measurement with soft wall potential varying the shape and corresponding potential. The placement of the top plate should be improved to achieve the desired accurate heights of the resonator since the heights correspond to the potential. The structure of the leads connecting to the outside world can be lengthened and changed. A multi-quantum-dot like resonator can be fabricated, and the transport behavior through the multi-quantum dots and their wave functions can be investigated.

There are works in which a scanning microscope is used to study current flow in a quantum point contact by M.A. Topinka [Top00, Top01]. By scanning the charged microscope tip above the two-dimensional electron gas, the electron flow through a narrow constriction in two-dimensional electron gas (quantum point contact) was imaged. The influence of the width of the quantum point contact and the position of the tip on current flow were studied. Such investigations of quantum point contacts can be easily simulated with microwave experiments.

Chapter 4

Wave function statistics for open systems

4.1 Intensity distribution in dependence of the phase rigidity

The statistical properties of the eigenfunctions and eigenvalues of a chaotic billiard can be well described by random matrix theory (RMT) [Guh98] or the random superposition of plane waves approach (RSPW) [Ber77]. At any point in the system, sufficiently far from the boundary, the wave function can be described by a random superposition of plane waves [Ber77],

$$\psi(\vec{r}) = \sum_n a_n \exp^{i\vec{k}_n \cdot \vec{r}}, \quad k = |\vec{k}_n| \quad (4.1)$$

where the modulus of the wave number k of the incoming wave is fixed, but the directions \vec{k}_n/k and amplitudes a_n are considered as random. In billiards with time-reversal symmetry, there is an additional restriction that the wave function has to be real. This ansatz is not strictly correct, because it completely ignores the boundary conditions at the billiard walls, but this is of no importance as long as the wave length is small enough compared to the billiard size. As an immediate consequence the wave function amplitudes are Gaussian distributed, or, equivalently, their squares $|\psi|^2$ are Porter-Thomas distributed,

$$P(|\psi|^2) = \sqrt{\frac{A}{2\pi|\psi|^2}} \exp\left(-\frac{A}{2}|\psi|^2\right), \quad (4.2)$$

where A is the billiard area.

For the spatial correlation function of the wave function amplitudes, one obtains a Bessel function,

$$C(\vec{r}_1, \vec{r}_2) = \langle \psi^*(\vec{r}_1) \psi(\vec{r}_2) \rangle = J_0(kr), \quad (4.3)$$

where $r = |\vec{r}_1 - \vec{r}_2|$. The brackets denote an average over all positions. All these features have been demonstrated by McDonald and Kaufman in their influential work on stadium wave functions [McD79, McD88]. It is impossible to mention all papers which have been published hitherto on the subject. The RSPW approach is not restricted to quantum mechanics. This is why experiments using classical waves have played an important role, since for a long time they were the only ones with the ability to look into the system. Very recently techniques have been developed which yield comparable information for electron flow patterns in mesoscopic structures [Top00]. The state of the art of experiments with classical waves is presented in reference [Stö99].

Most of experiments with classical waves have been performed in microwave resonators [Stö90, Sri91, Grä92] and vibrating solids [Ell95]. In one work, light propagation through a wave guide with distorted cross-section was studied [Doy02]. In all cases the predictions of the RSPW approach could be verified. It should be noted that in the general case there is *no* one-to-one correspondence to quantum mechanics, thus demonstrating the universality of the approach. Therefore similar ideas have been developed independently in the context of room acoustics [Ebe84]. Quasi-two-dimensional microwave resonators constitute one prominent exception where the equivalence to quantum mechanics is complete, including the boundary conditions. This is no longer true in three-dimensional resonators. But even here the approach remains valid [Dör98]. One only has to superimpose plane *electromagnetic* waves with the consequence that expression (4.3) for the spatial autocorrelation function has to be modified [Eck99].

If the billiard is opened, or if time-reversal symmetry is broken, the wave functions are complex, and currents are present, the wave function acquires an imaginary part,

$$\psi = \psi_R + i\psi_I, \quad (4.4)$$

where ψ_R and ψ_I are orthogonal. In Ref. [Bro03], the wave function distribution was described as the convolution of a Gaussian distribution with correlated real and imaginary parts and that of a single complex number ρ , the dot product of the wave function ψ and its time reversed,

$$\rho = \int d\vec{r} \cdot \psi(\vec{r})^2. \quad (4.5)$$

The square modulus $|\rho|^2$ is known as the “phase rigidity” of the wave function ψ [Lan97]. Real wave functions have $\rho = 1$, whereas $\rho = 0$ is fully complex, *i. e.*,

ψ_R and ψ_I have the same magnitude.

In microwave experiments wall absorption is another source of currents. For quasi-two-dimensional electromagnetic cavities we use the one-to-one correspondence between the z -component of the electric field E_z and the quantum-mechanical wave function ψ . We normalize the wave function ψ such that

$$\int d\vec{r} |\psi(\vec{r})|^2 = 1. \quad (4.6)$$

Then the square of the z -component of the electric field and the Poynting vector correspond to the normalized ‘‘intensity’’ and ‘‘current’’ density, respectively [Šeb99].

$$I(\vec{r}) = A|\psi(\vec{r})|^2, \quad \vec{j}(\vec{r}) = \frac{A}{k} \text{Im}[\psi^*(\vec{r})\nabla\psi(\vec{r})]. \quad (4.7)$$

In dependence of the phase rigidity ρ , the distribution of the intensity $I = A|\phi|^2$ changes from Porter-Thomas (Eq. (4.2)) to single exponential behavior. An explicit formula describing the distribution in this cross-over regime has been given by different authors [Życ91, Kan96, Pni96, Sai02],

$$P_\rho(I) = \frac{1}{\sqrt{1-|\rho|^2}} \exp\left[-\frac{I}{1-|\rho|^2}\right] I_0\left[\frac{|\rho|I}{1-|\rho|^2}\right], \quad (4.8)$$

In the case of $\rho = 1$, there is no imaginary part, then Eq. (4.8) reduces to the Porter-Thomas distribution, whereas one obtains an exponential distribution for $\rho = 0$, or $\langle |\psi_R|^2 \rangle = \langle |\psi_I|^2 \rangle$.

By convolution Eq. (4.8) with the distribution of phase rigidity $p(\rho)$, we can obtain the full intensity distribution,

$$P(I) = \int d\rho p(\rho) P_\rho(I). \quad (4.9)$$

The distribution $p(\rho)$ was calculated in Ref. [Bro03] and is given by,

$$p(\rho) = \frac{6 + 2(1 - |\rho|^2)^{1/2}}{3\pi (1 + (1 - |\rho|^2)^{1/2})^3}, \quad 0 \leq |\rho| \leq 1. \quad (4.10)$$

For the experiment, we used the same resonator as in Fig. 3.2, but to break the symmetry of the shape of the resonator and to block direct transport, we placed two half disks with a radius of 3 cm in the resonator. These were made of the same material as the resonator. In the range of 4-18 GHz, the same measurements as described in section 3.2.1 were done. We now describe the measured wave function distributions.

We first discuss wave function distributions measured at a fixed frequency, and compare the results to the theory for the corresponding fixed value of ρ . A statistical distribution at a fixed frequency is obtained by varying the position of the antenna only. The phase rigidity $|\rho|^2$ can be measured independently using Eq. (4.5). Fig. 4.1 shows the intensity distribution for the intensity pattern at 11.048, 12.015, 13.865 GHz shown in the left panel of Fig. 4.2 together with the theory of Eq. (4.8), using the measured value of $|\rho|^2 = 0.0937, 0.5226, 0.2358$. The solid lines in Fig. 4.1 indicate the calculated values from Eq. (4.8). Dark color corresponds to large intensity in wave function in the left column in Fig. 4.2. The corresponding currents maps are shown in the right column in fig. 4.2, and the arrow lengths indicate the magnitudes of the Poynting vectors.

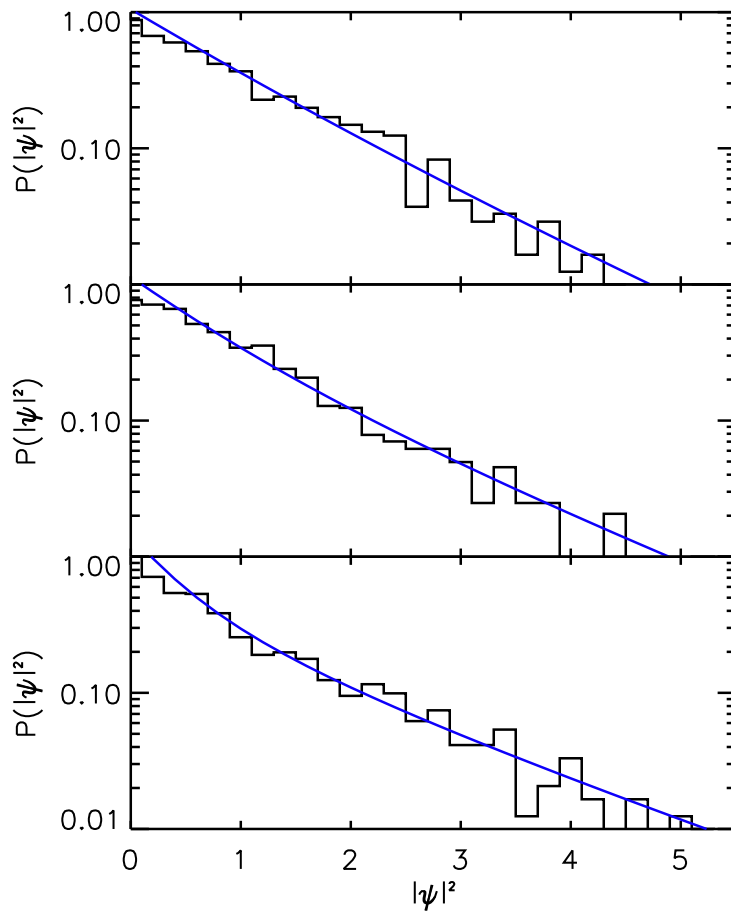


Figure 4.1: Intensity distribution for the wave function Intensity distribution for the wave function at $\nu = 11.048, 12.015, 13.865$ GHz. The corresponding wave functions are shown in Fig. 4.2. The theoretical values from Eq. (4.8) with $|\rho|^2 = 0.0937, 0.5226, 0.2358$ are plotted with solid line.

As was discussed in Ref. [Bar02], there are frequency regimes where the leakage to the probe antenna becomes intolerably high, either due to the fact that the

transport through the cavity is small, or due to some strongly scarred wave functions. In all such cases there were strong deviations from the generalized Porter-Thomas behavior described by Eq. (4.8). We therefore only used frequency regimes where $P_\rho(I)$ was in agreement with theory on a confidence level of 90 percent.

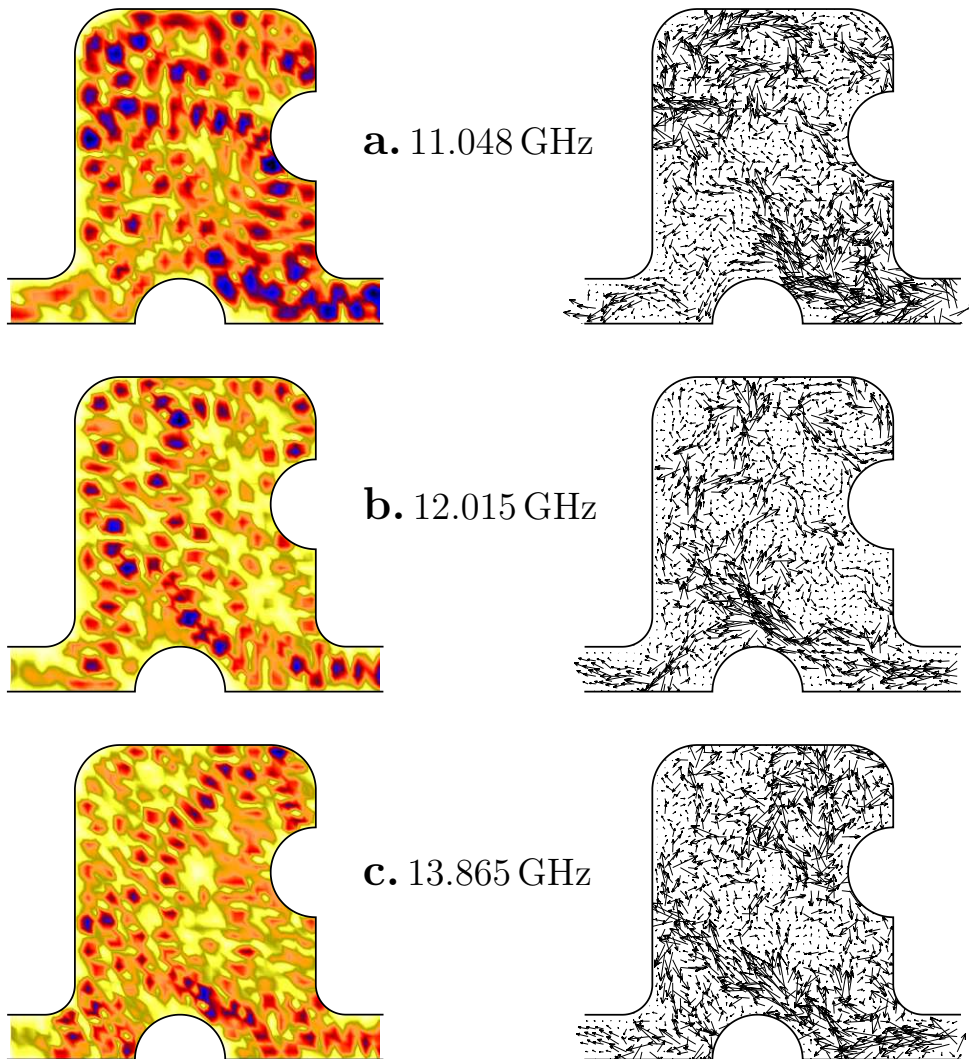


Figure 4.2: Typical wave functions and corresponding current distributions for asymmetrical billiard

The selected wave function plots $|S_{12}|$ (left panel) and the corresponding current distributions (right panel) for $a = 11.048$ GHz, $b = 12.015$ GHz, $c = 13.865$ GHz. Black in wave functions corresponds to maximum intensity and arrow lengths in flow map indicate the magnitude of the Poynting vector.

4.2 Current and vorticity auto correlation

The consequences of the RSPW approach for the distribution of currents have been studied in particular by Berggren and coworkers in a series of papers [Ber99, Sai01, Ber01, Sai02]. In open systems there are no longer nodal lines but nodal points, or vortices, since for the wave function to be zero both real and imaginary part have to be zero at the same time. Two-point correlation functions of vortices have been given independently by Berry and Dennis [Ber00] and by Saichev et al. [Sai01]. Nearest neighbor distributions of vortices have been studied in Ref. [Ber02]. The theoretical predictions have been tested experimentally in two microwave experiments [Bar02, Vra02], including a direct visualization of persistent currents well-known from mesoscopic physics. In the present paper a number of additional microwave tests of the RSPW hypothesis are presented with special emphasis on spatial auto correlation functions of currents and vorticities. To the best of our knowledge such quantities have never been studied before, neither theoretically nor experimentally.

Fig. 4.3 shows plots of the vorticities, or vortex strengths at the same frequencies as in Fig. 4.2. The vorticity is, up to the factor $1/2$, just the curl of the current [Ber00] and reduces for two-dimensional systems to

$$\omega = (\nabla_x \psi_R)(\nabla_y \psi_I) - (\nabla_y \psi_R)(\nabla_x \psi_I), \quad (4.11)$$

where ψ_R, ψ_I are real and imaginary part of the wave function. A plot of the vorticity is particularly useful to make the vortex pattern visible.

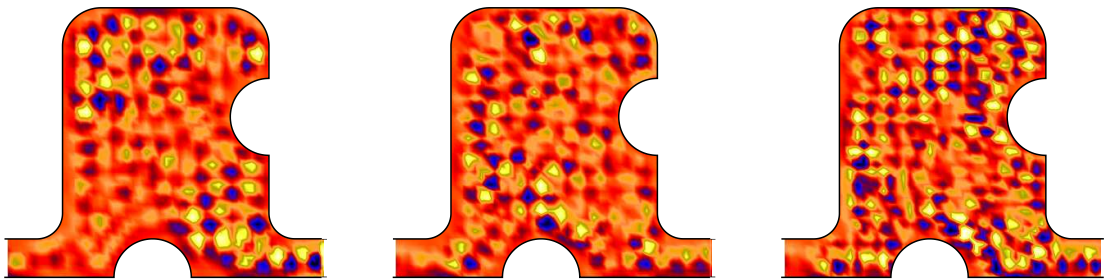


Figure 4.3: Selected vorticity map
The vorticity maps at $\nu = 11.048$, 12.015 , and 13.865 GHz. The corresponding wave functions are shown in Fig. 4.2.

It follows immediately from the RSPW hypothesis, as a consequence of the central

limit theorem, that $\psi(r)$ can be treated as Gaussian random variables. They obey the well-known property that all higher moments can be expressed in terms of the second moment. Thus all distributions of interest can be calculated [Sre96a, Sre96b]. We do not follow this route, however, but start directly from Eq. (4.1) to calculate current and vorticity auto correlation functions.

Writing $\vec{k}_n = k(\cos \varphi_n, \sin \varphi_n)$, we obtain for the derivatives of the wave function

$$\begin{aligned}\frac{\partial \psi}{\partial x} &= ik \sum_n a_n \cos \varphi_n e^{i\vec{k}_n \cdot \vec{r}} \\ \frac{\partial \psi}{\partial y} &= ik \sum_n a_n \sin \varphi_n e^{i\vec{k}_n \cdot \vec{r}}\end{aligned}\quad (4.12)$$

Using Eq. (4.7), it follows for the x component of the current

$$j_x(\vec{r}) = k \sum_{n,m} a_n^* a_m (\cos \varphi_n + \cos \varphi_m) e^{-i(\vec{k}_n - \vec{k}_m) \cdot \vec{r}}. \quad (4.13)$$

In calculating the autocorrelation functions

$$C_{j_x}(\vec{r}_1, \vec{r}_2) = \langle j_x(\vec{r}_1) j_x(\vec{r}_2) \rangle \quad (4.14)$$

we use the assumption that the a_n are uncorrelated

$$\langle a_n^* a_m \rangle = \langle |a_n|^2 \rangle \delta_{nm}. \quad (4.15)$$

It follows from Eqs. (4.13) and (4.14)

$$\begin{aligned}C_{j_x}(\vec{r}_1, \vec{r}_2) &\sim k^2 \left\langle \sum_{n,m} |a_n|^2 |a_m|^2 (\cos \varphi_n + \cos \varphi_m)^2 e^{-i(\vec{k}_n - \vec{k}_m) \cdot (\vec{r}_1 - \vec{r}_2)} \right\rangle \\ &\sim \left\langle \cos^2 \varphi_n e^{-i\vec{k}_n \cdot \vec{r}} \right\rangle \left\langle e^{i\vec{k}_n \cdot \vec{r}} \right\rangle + \left\langle \cos \varphi_n e^{-i\vec{k}_n \cdot \vec{r}} \right\rangle \left\langle \cos \varphi_n e^{i\vec{k}_n \cdot \vec{r}} \right\rangle,\end{aligned}\quad (4.16)$$

where $\vec{r} = \vec{r}_1 - \vec{r}_2$. All averages can be expressed in terms of Bessel functions with the result

$$C_{j_x}(r) = \langle J_0(kr)[J_0(kr) - \cos 2\varphi J_2(kr)] + 2 \cos^2 \varphi [J_1(kr)]^2 \rangle, \quad (4.17)$$

where we have written $C_{j_x}(r)$ instead of $C_{j_x}(\vec{r}_1, \vec{r}_2)$ to indicate that the autocorrelation function depends on $r = |\vec{r}_1 - \vec{r}_2|$ exclusively. The normalization $C_{j_x}(0) = 1$ was applied. It only remains to perform the average over φ , the angle between vector \vec{r} and the x axis. The averaging gives

$$C_{j_x}(r) = [J_0(kr)]^2 + [J_1(kr)]^2. \quad (4.18)$$

For the autocorrelation function of $j_y(r)$ the same expression is obtained. Instead of averaging over φ , we may alternatively look for two other quantities, namely the autocorrelation functions of $j_{\parallel}(r)$, and $j_{\perp}(r)$, the current components parallel and perpendicular to \vec{r} , respectively. Inserting $\varphi = 0$ and $\varphi = \frac{\pi}{2}$ we obtain from Eq. (4.17)

$$\begin{aligned} C_{j_{\parallel}}(r) &= J_0(kr)[J_0(kr) - J_2(kr)] + 2J_1(kr) \\ C_{j_{\perp}}(r) &= J_0(kr)[J_0(kr) + J_2(kr)] \end{aligned} \quad (4.19)$$

In the same way the spatial autocorrelation function for the vorticity is obtained, entering definition from Eq. (4.11) with expressions in (4.12) for the derivatives of the wave function. The derivation is a step-by-step repetition of the calculation for $C_{j_x}(r)$, and we find

$$\begin{aligned} C_{\omega}(r) &= \frac{\langle \omega(\vec{r}_1)\omega(\vec{r}_2) \rangle}{\langle \omega(\vec{r}_1)^2 \rangle} \\ &= [J_0(kr)]^2 - [J_1(kr)]^2 \end{aligned} \quad (4.20)$$

All correlation functions depend on the parameter kr exclusively. Therefore it is possible to superimpose the results from different frequencies by an appropriate rescaling to improve statistics. We start with the presentation of our results for the spatial autocorrelation function of the wave function amplitudes (see Fig. 4.4). A perfect agreement is found between the experimental results and the prediction from the RSPW hypothesis. This may be considered as a check for the validity of the approach in the selected frequency regimes.

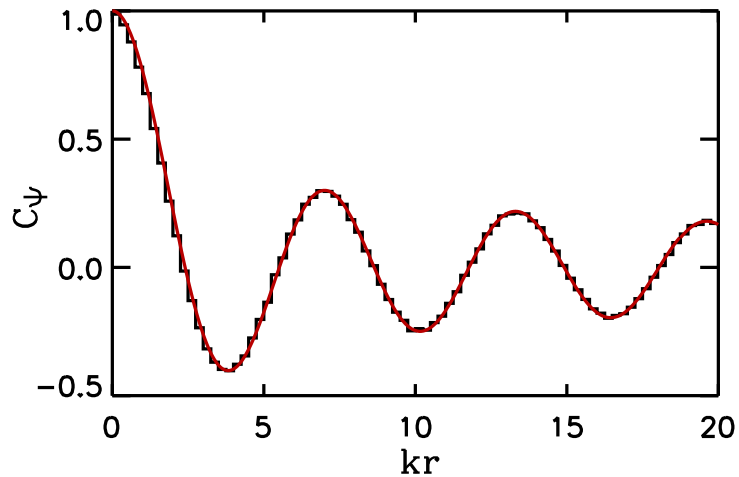


Figure 4.4: Spatial autocorrelation functions

Experimental spatial autocorrelation functions of the wave function amplitude for the quantum dot billiard. The solid lines correspond to the prediction from the random-superposition of plane-waves approach (see Eq. (4.3)).

In Fig. 4.5, the results of the different current autocorrelation functions derived in Eqs. (4.18), (4.19), are shown for the experimental data. The overall agreement is very good.

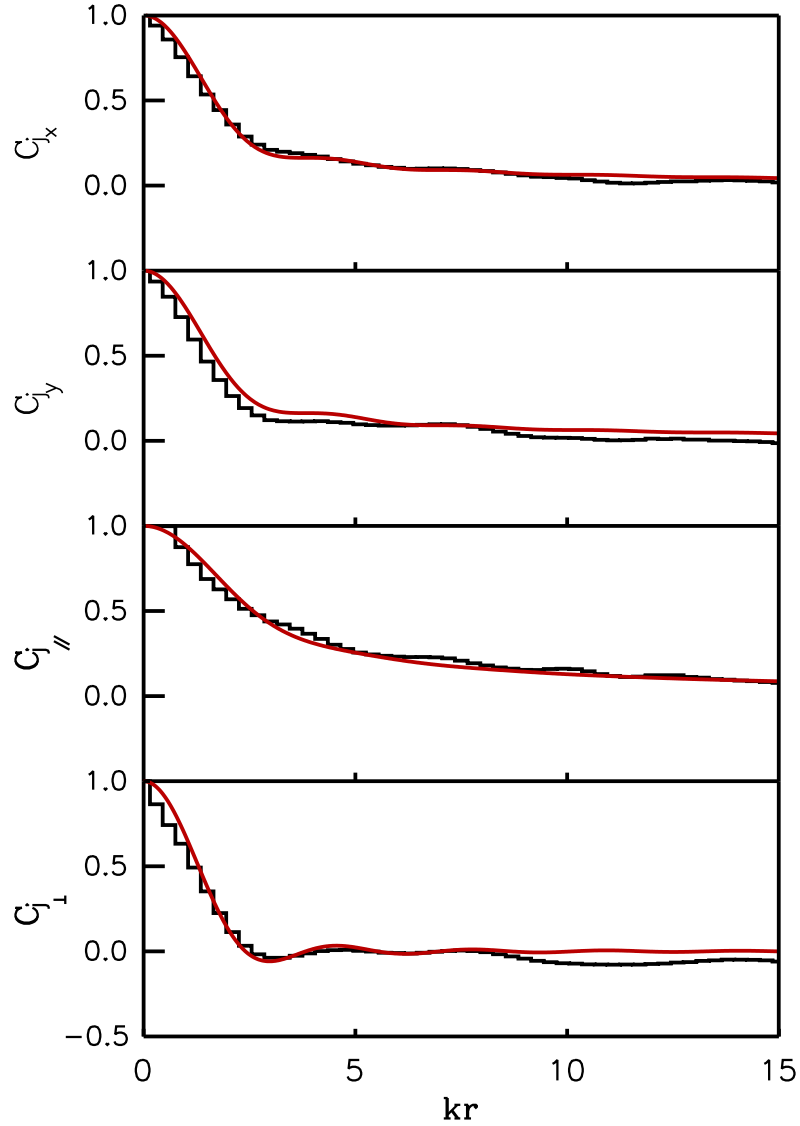


Figure 4.5: Spatial autocorrelation functions of $j_x(r)$, $j_y(r)$, $j_{\parallel}(r)$, and $j_{\perp}(r)$ Experimental spatial autocorrelation functions of $j_x(r)$, $j_y(r)$, $j_{\parallel}(r)$, and $j_{\perp}(r)$ (from top to bottom) for the quantum dot billiard. The solid lines correspond to the predictions from the random-superposition of plane-waves approach (see Eqs. (4.18) to (4.19)).

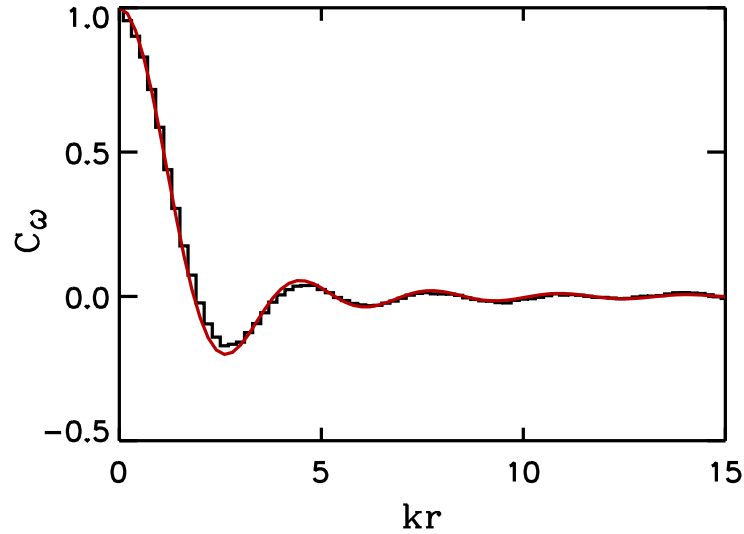


Figure 4.6: Experimental spatial autocorrelation functions of the vorticity $\omega(r)$. The solid lines correspond to the predictions from the random-superposition of plane-waves approach (see Eq. (4.20)).

For the vorticity autocorrelation function, shown in Fig. 4.6, the agreement between theory and experiment is nearly perfect. In Fig. 4.7 vortex pair correlation function for the system is presented. The vortex pair correlation function is given by [Ber00, Sai01]

$$g(kr) = \frac{1}{d^2} \langle \delta(R_A) \delta(I_A) \delta(R_B) \delta(I_B) |\omega_A| |\omega_B| \rangle \quad (4.21)$$

where A, B two vortices with distance r and their real R_A , R_B and imaginary part I_A , I_B . The corresponding vorticities ω_A , ω_B are calculated from Eq. 4.11. The expected oscillatory behavior again is reproduced correctly. The deviations between experiment and theory at small distances reflect the experimental resolution. The data were taken on a grid of 5 mm side length with the consequence that vortices with a distance below 10 mm can no longer be separated reliably.

We now extend this discussion to the nearest neighbor spacing distribution between vortices. This quantity was introduced by Saichev et al., [Sai01] and was studied by the authors in a number of papers. There are different types of spacing distributions denoted by $P_{++}(r)$, $P_{+-}(r)$, $P_{-+}(r)$, $P_{--}(r)$ where the pair of indices denotes the sense of rotation of the vortices considered. $P_{++}(r)$ and $P_{--}(r)$, as well as $P_{+-}(r)$ and $P_{-+}(r)$ should be identical, of course. Only for small system sizes (where the RSPW approach fails anyway) there may be deviations due to the presence of the boundary [Sai01]. Fig. 4.8 shows our results, for $P_{++}(r)$, $P_{--}(r)$ and $P_{+-}(r)$, $P_{-+}(r)$. The theoretical curve is the result of the Poisson approximation [Sai01]. It is obtained from the vortex pair-correlation functions and

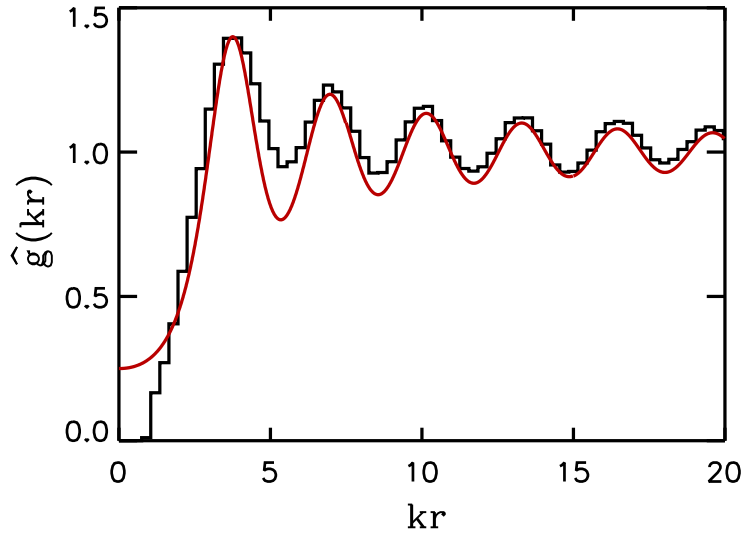


Figure 4.7: Vortex pair correlation function

The solid line corresponds to the theoretical prediction from the random-superposition-of-plane waves approach [Ber00, Sai01].

neglects all higher order correlations. The deviations between experiment and theory for $P_{+-}(r)$, $P_{-+}(r)$ are comparable to that found in the papers of the Berggren group [Sai01, Ber02], and reflect at least partly the limitations of the Poisson approximation. Another cause, in particular for the small distances, is the limited experimental resolution discussed above. For $P_{++}(r)$, $P_{--}(r)$, on the other hand, the agreement between experiment and theory is quite good, again in accordance with Refs. [Sai01, Ber02]. In addition, the experiment resolution has only a small effect in this case, since small distances do not contribute anyway to $P_{++}(r)$, $P_{--}(r)$ significantly.

In this section, a number of consequences of the RSPW hypothesis have been presented not been studied hitherto. A qualitatively good agreement between the experiment and the theoretical prediction was found for different types of spatial current correlation functions. The remaining discrepancies are probably due to experimental imperfections caused by leakage currents into the probe antennas. For the vorticity autocorrelation function a perfect agreement between experiment and theory is found. In addition vortex pair correlation functions, and vortex nearest neighbor distance distributions were studied. Again the agreement between experiment and theory are good, apart from discrepancies at small distances.

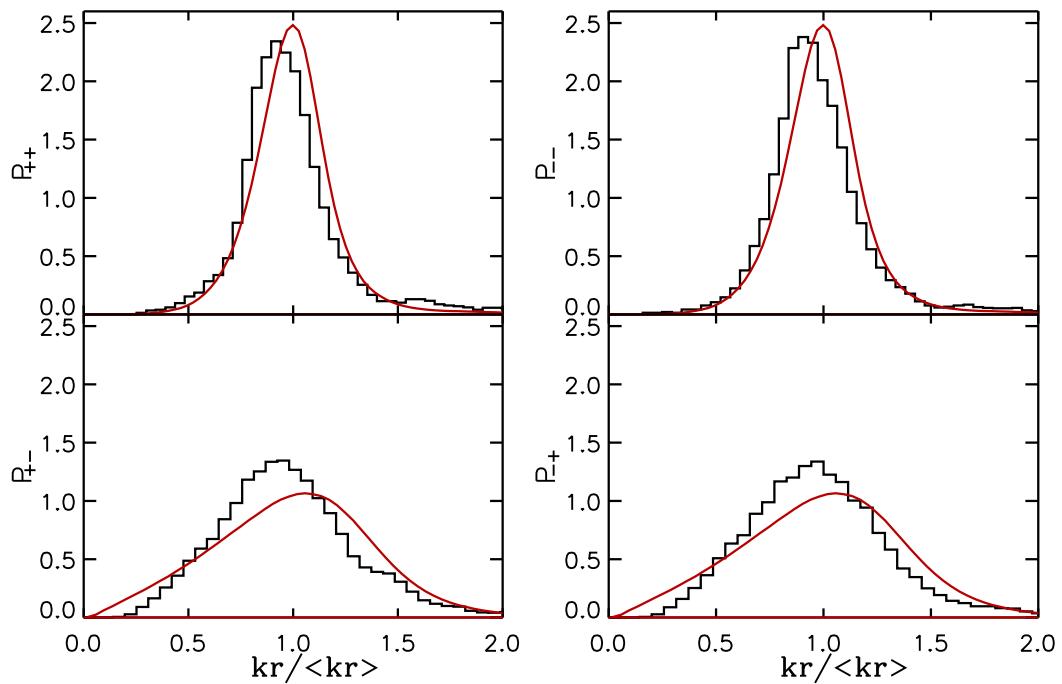


Figure 4.8: Nearest neighbor distance distribution of vortices

Nearest neighbor distance distribution of vortices of opposite ($P_{+-}(r)$), ($P_{-+}(r)$) in the lower panel and same sense of rotation ($P_{++}(r)$), ($P_{--}(r)$) in the upper panel respectively, for the hard wall billiard. The solid lines have been calculated from the respective pair correlation functions, neglecting higher order correlations.

4.3 Long-range correlation

For microwaves, an open billiard is obtained by connecting a two-dimensional microwave cavity to wave guides. The parameter governing the crossover from real to complex wave functions is the total number of channels N in the two wave guides. As was shown by P.W. Brouwer [Bro03], wave functions in this crossover have a non-Gaussian distribution and long-range correlations, just like the eigenvectors of the Pandey-Mehta Hamiltonian (4.22).

$$H(\alpha) = H_0 + \alpha H_1, \quad (4.22)$$

where H_0 and H_1 are real and complex random hermitian matrices, respectively, and α is a crossover parameter. The main difference, however, is that the crossover parameter N is discrete and can be measured independently. We here report on the first measurement of such long-range wave function correlations in the real-to-complex crossover. In this section, we study spatial correlation functions of the *squares* of intensities and currents. The statistical average is taken by averaging over both position \vec{r} and frequency ν . It is for these quantities and for this full ensemble average that long-range correlations were predicted [Bro03].

In order to explain the origin of long-range correlations of intensity and current density in an open chaotic billiard, we consider the joint distribution of intensities at points \vec{r}_1 and \vec{r}_2 with separation $kr = k|\vec{r}_1 - \vec{r}_2| \gg 1$,

$$P[I(\vec{r}_1), I(\vec{r}_2)] = \int d\rho p(\rho) P_\rho[I(\vec{r}_1)] P_\rho[I(\vec{r}_2)]. \quad (4.23)$$

For an open billiard, ρ has a nontrivial distribution, hence the long-range correlations of $P[I(\vec{r}_1), I(\vec{r}_2)]$. Whereas random matrix theory predicts the long-range correlations of intensities through Eq. (4.23), it cannot alone predict the long-range correlations of current densities and the precise dependence of these correlators on the separation $r = |\vec{r}_1 - \vec{r}_2|$ for $kr = k|\vec{r}_1 - \vec{r}_2|$ of order unity. However, as shown in Ref. [Bro03], the latter can be obtained from the random matrix result by making use of a random sum over plane waves (see Eq. (4.1)). The plane wave amplitudes $a(\vec{k})$ of Eq. 4.1 have a Gaussian distribution with zero mean and with variance

$$\langle a(\vec{k})a(-\vec{k}) \rangle = \rho \langle a(\vec{k})a^*(\vec{k}) \rangle, \quad (4.24)$$

where ρ is the (random) phase rigidity of ψ . Performing the ensemble average using Eqs. (4.1) and (4.24), the correlators of intensity and current density can be expressed in terms of moments of the phase rigidity $|\rho|^2$. Long range correlations are found for correlators involving the square of the intensity I and the current

density $J = |\vec{j}|$,

$$\begin{aligned}
\langle I(\vec{r}_1)^2 I(\vec{r}_2)^2 \rangle_c &= \text{var } |\rho|^2 + 4J_0(kr)^2 \langle 4 + 13|\rho|^2 + |\rho|^4 \rangle \\
&\quad + 4J_0(kr)^4 \langle 1 + 4|\rho|^2 + |\rho|^4 \rangle, \\
\langle I(\vec{r}_1)^2 J(\vec{r}_2)^2 \rangle_c &= -\frac{1}{4} \text{var } |\rho|^2 + J_0(kr)^4 \langle 2 - |\rho|^2 - |\rho|^4 \rangle, \\
\langle J(\vec{r}_1)^2 J(\vec{r}_2)^2 \rangle_c &= \frac{1}{4} \text{var } |\rho|^2 + \frac{1}{2} J_0(kr)^2 \langle 1 - 2|\rho|^2 + |\rho|^4 \rangle \\
&\quad + \frac{1}{4} J_0(kr)^4 \langle 3 - 5|\rho|^2 + 2|\rho|^4 \rangle. \tag{4.25}
\end{aligned}$$

Here J_0 is the Bessel function, and the subscript “c” refers to the connected correlator, $\langle AB \rangle_c = \langle AB \rangle - \langle A \rangle \langle B \rangle$. The relevant moments of the phase rigidity $|\rho|^2$ were calculated in Ref. [Bro03] and are compared with the experimental values in Tab. 4.1. We found a good agreement between experiment and theory.

N	$\langle \rho ^2 \rangle$			$\langle \rho ^4 \rangle$		
	2	4	6	2	4	6
Theory	0.7268	0.5014	0.3918	0.6064	0.3285	0.2155
Experiment	0.7116	0.4986	0.3849	0.6070	0.3464	0.2368

Table 4.1: The calculated and experimental moments of the phase rigidity

To have a well defined number of transversal modes within each waveguide, we investigate the frequency regimes 5-9.5, 10-14.5, 15-18 GHz, corresponding to a total number of channels $N=2, 4, 6$, respectively (*i. e.*, 1, 2, and 3 propagating modes in each waveguide)

We now describe our results for a full ensemble average, in which both the position of the detector antenna and the frequency are varied. Fig. 4.9 shows the measured phase rigidity distribution $P(|\rho|^2)$ together with the theory of Ref. [Bro03], for $N = 2, 4$, and 6. Good agreement is found between experiment and theory, especially as there is no free parameter. Figures 4.10, 4.11, and 4.12 show measurement and theoretical prediction for the correlation functions of the squared intensity and the squared current density at positions \vec{r} and \vec{r}' . Since these correlation functions depend on the positions \vec{r} and \vec{r}' through the combination kr only, results from different frequency regimes can be superimposed by a proper scaling. In our analysis, we selected frequency windows for averaging of $\Delta\nu = 0.3$ GHz guaranteeing that $\Delta\nu \ll c/2\nu L$, where L is the billiard size and c the velocity of wave propagation. The gaps in the $N = 4, 6$ histograms for small values of kr reflect the spatial resolution, which is limited to 5 mm due to the chosen grid size. For the long-range correlations, we observe very good agreement between experiment and theory for the squared intensity correlation $\langle I(\vec{r}_1) I(\vec{r}_2) \rangle$. The short-range oscillations predicted by theory are suppressed to a large extent

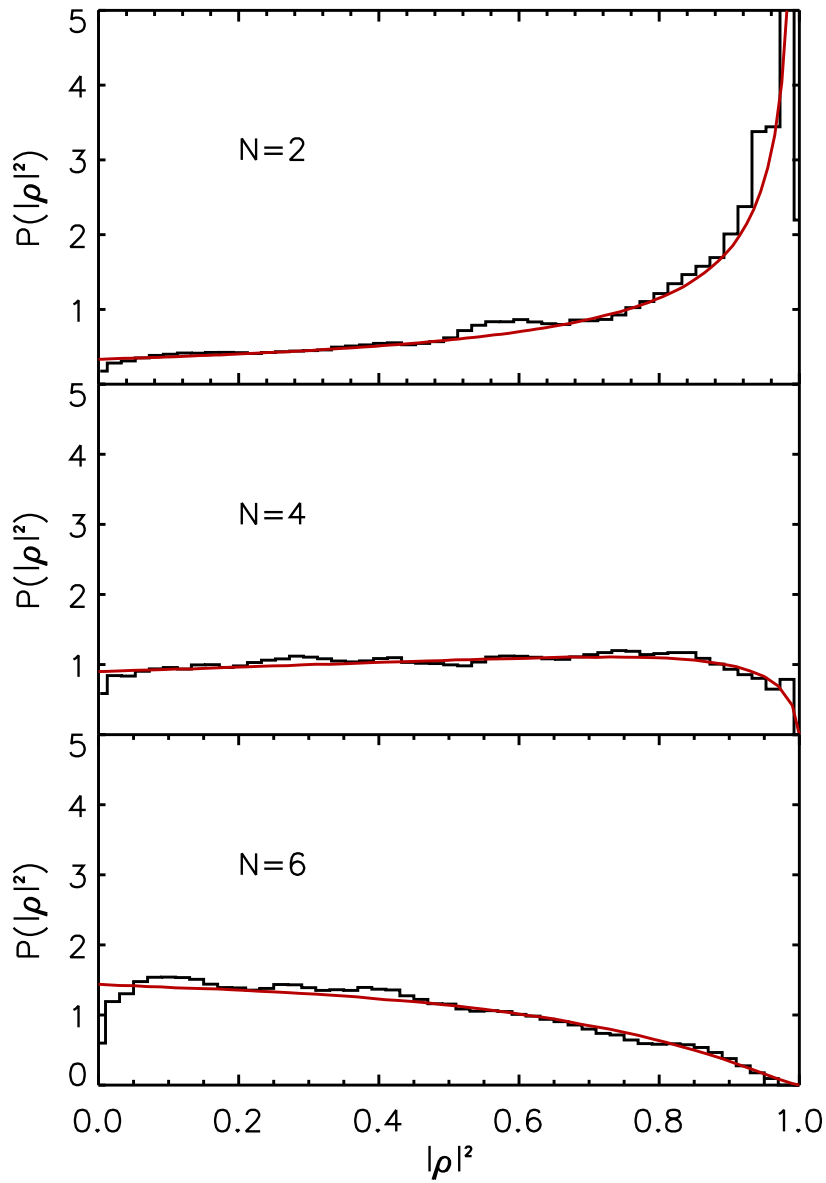


Figure 4.9: Phase rigidity distribution $P(|\rho|^2)$ for different values of the total number of channels N . Solid curves indicate the theory of Ref. [Bro03].

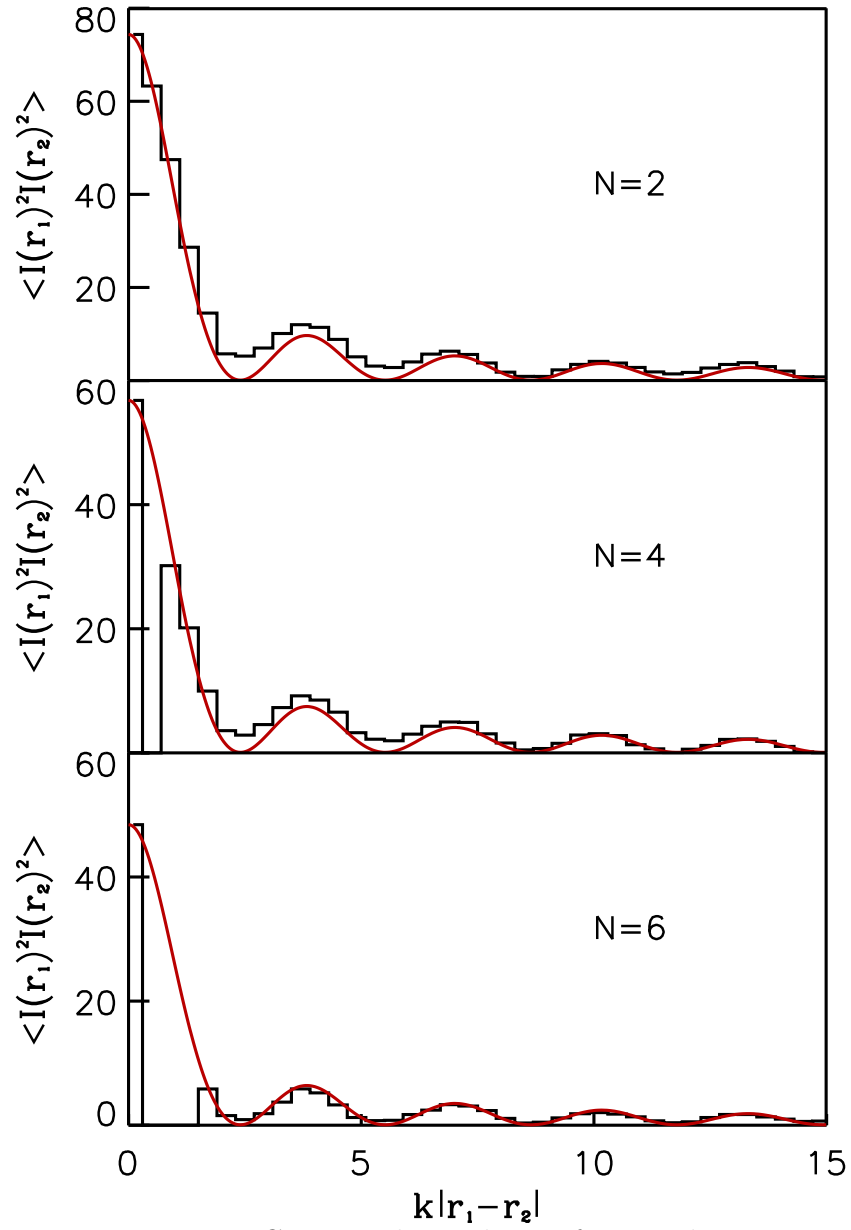


Figure 4.10: Connected correlator of squared intensity $\langle I(\vec{r}_1)^2 I(\vec{r}_2)^2 \rangle_c$ versus kr for different values of the total number of channels N .

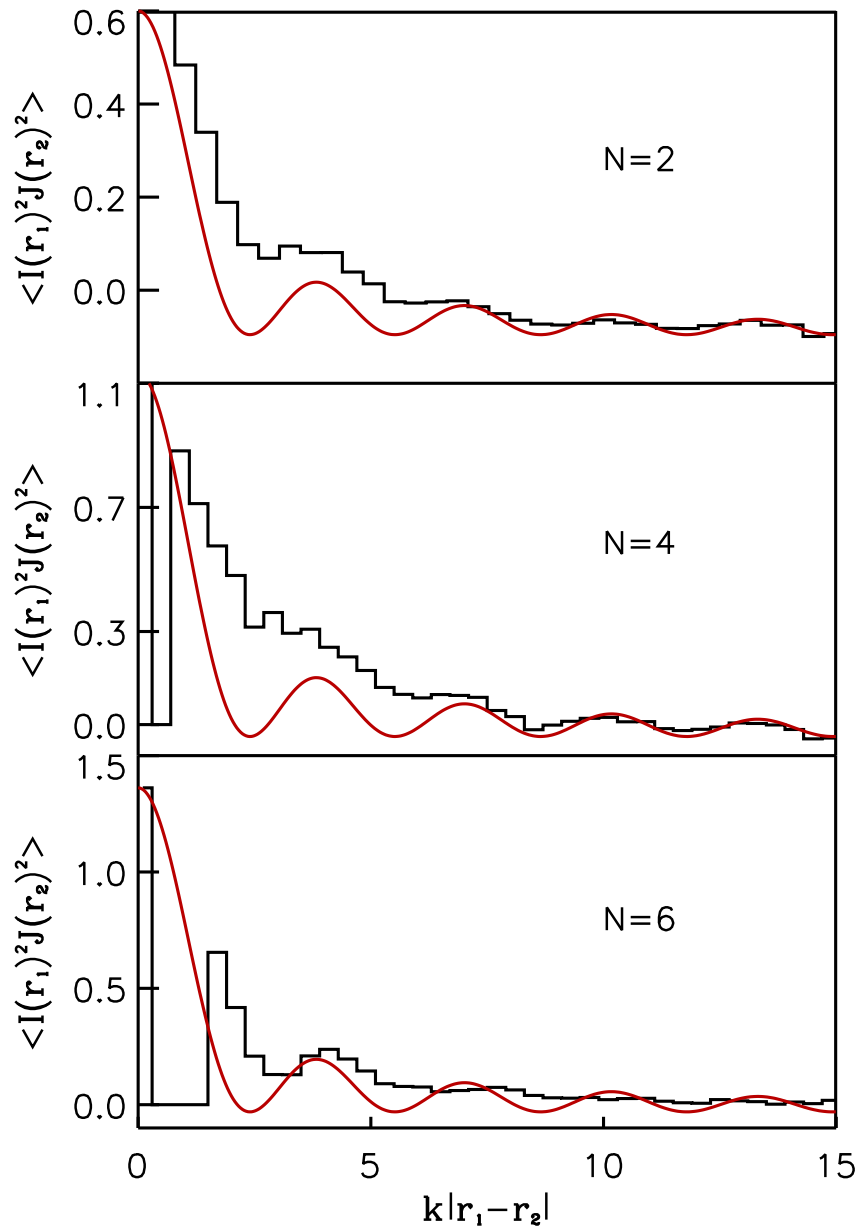


Figure 4.11: Connected correlator of squared intensity and squared current density

$\langle I(\vec{r}_1)^2 J(\vec{r}_2)^2 \rangle_c$ versus kr , for different values of the total number of channels N .

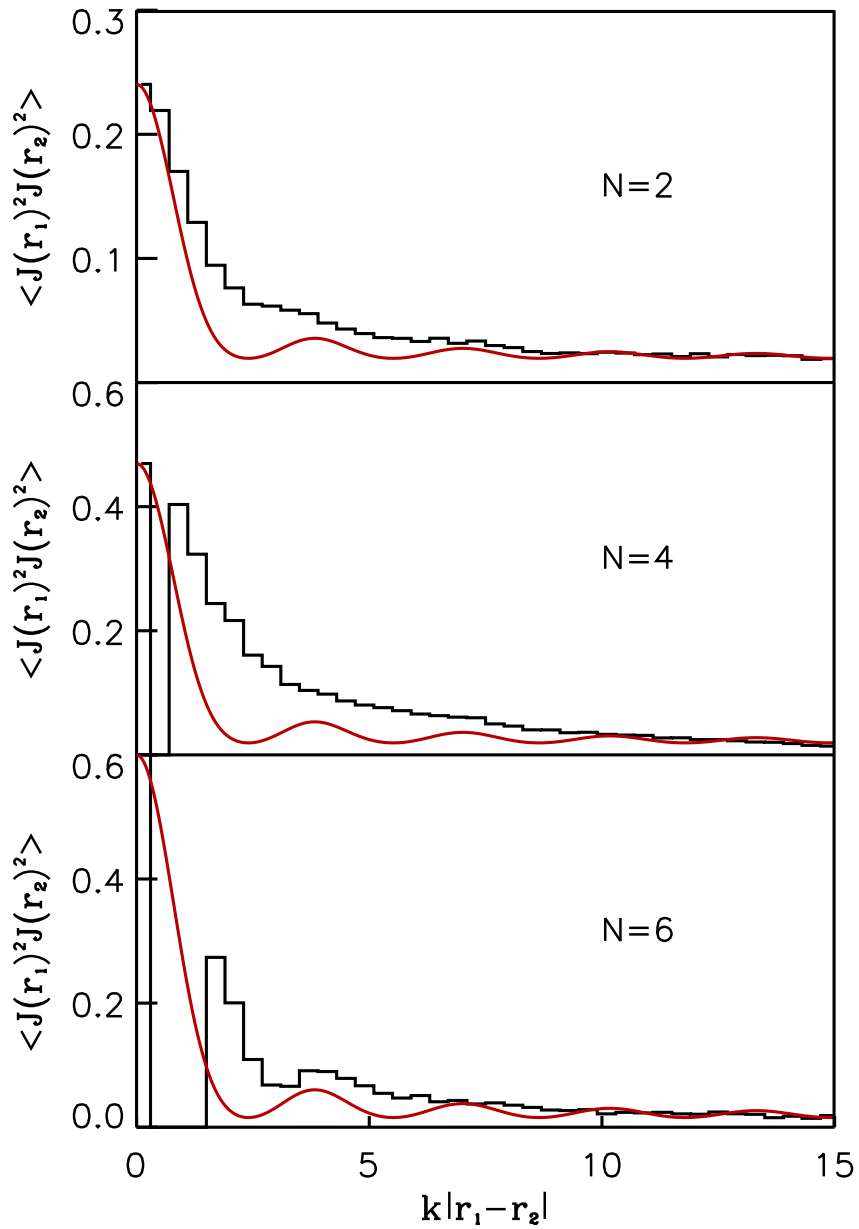


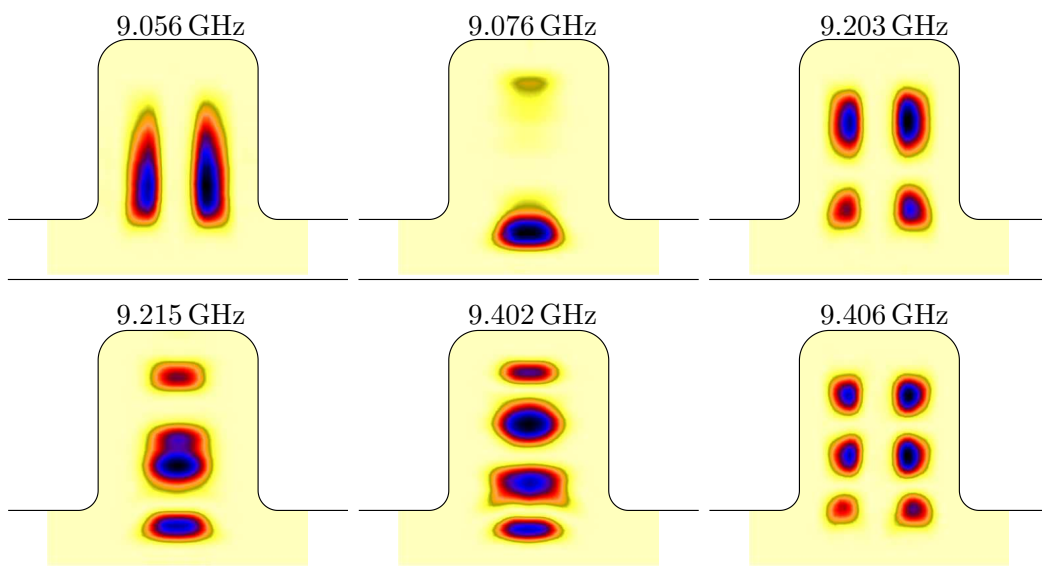
Figure 4.12: Connected correlator of squared current density $\langle J(\vec{r}_1)^2 J(\vec{r}_2)^2 \rangle_c$ versus kr for different values of the total number of channels N .

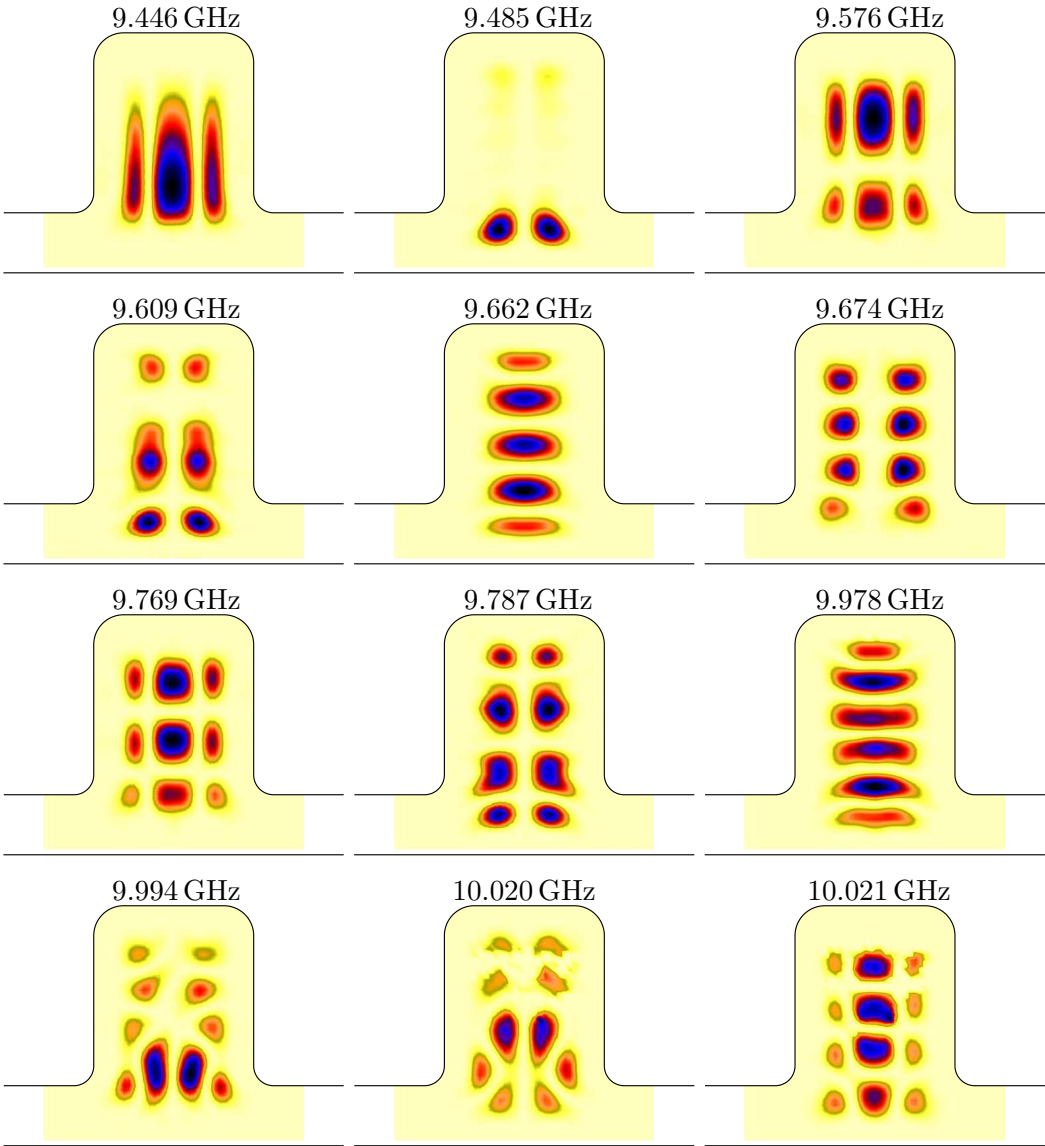
in the experiment for the correlators that involve the current density, however. This, again, is a consequence of the limited resolution. We would like to stress, however, that the asymptotic values of all correlations in the limit $kr \rightarrow \infty$ is different from zero and in perfect agreement with the predictions from Eq. (4.25). We analyzed the measured data with the symmetric billiard in Fig. 3.2. For the all magnitudes mentioned above, we could also find very good agreement with the theoretical prediction in spite of the symmetry of the billiard shape. The influence of the coupling antenna might be strong enough to break the symmetry of the system.

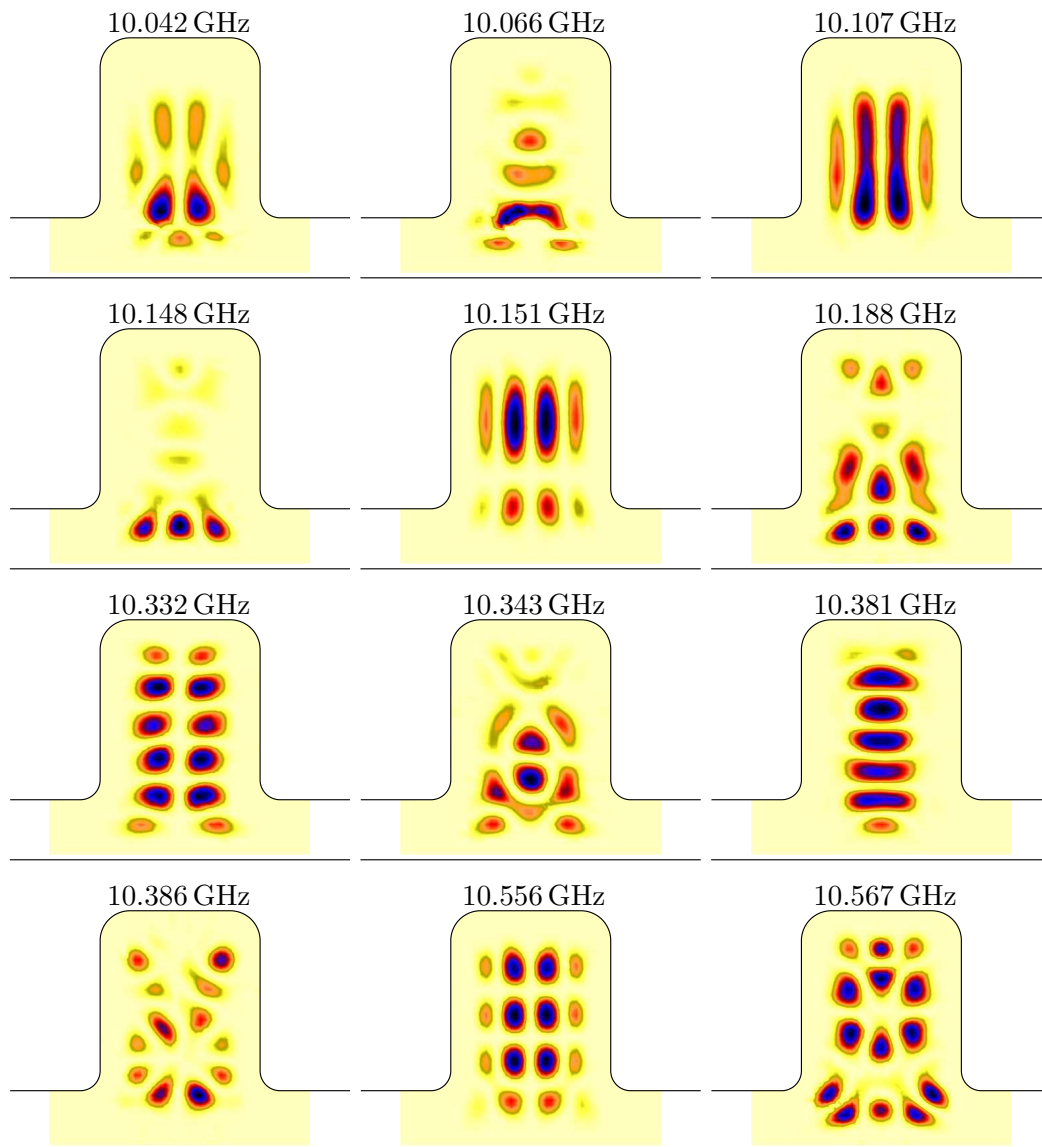
Long-range correlations have also been observed in the transmission of microwaves [Seb02] and visible light [Emi03] through two- and three-dimensional disordered media, in which wave propagation is diffusive. There are important differences between the long-range correlations observed in Refs. [Seb02, Emi03] and those in ballistic systems, which are reported here. First, in Refs. [Seb02, Emi03], long-range correlations appear already for the intensity autocorrelation function, whereas we find long-range correlations for correlators of second and higher moments only. Second, in Refs. [Seb02, Emi03], the correlations scale with the inverse of the sample conductance, whereas in the present work there is no small parameter that sets the size of the long-range correlations, irrespective of sample size or distance. In that sense, only the latter correlations are truly long range.

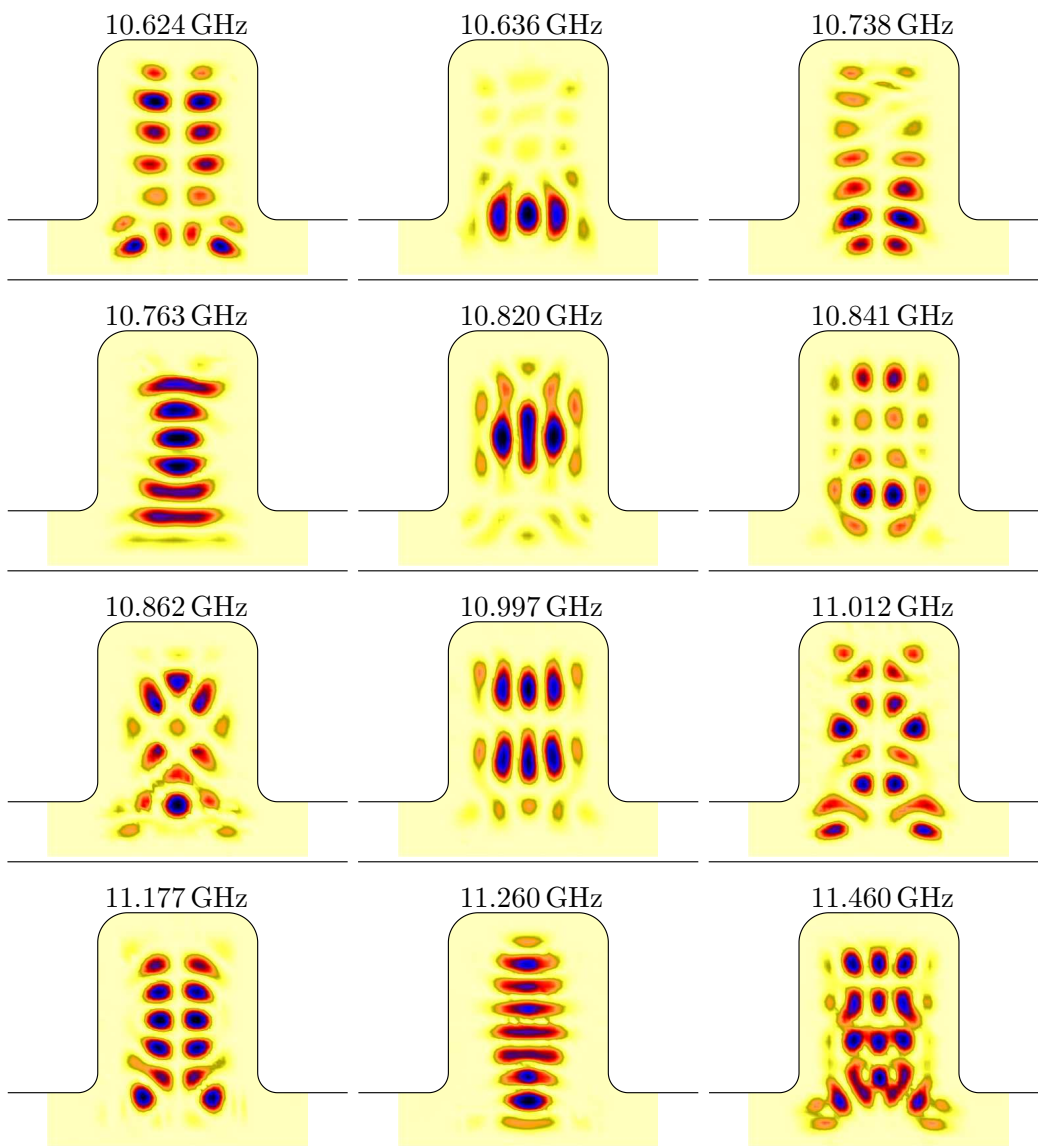
Appendix A

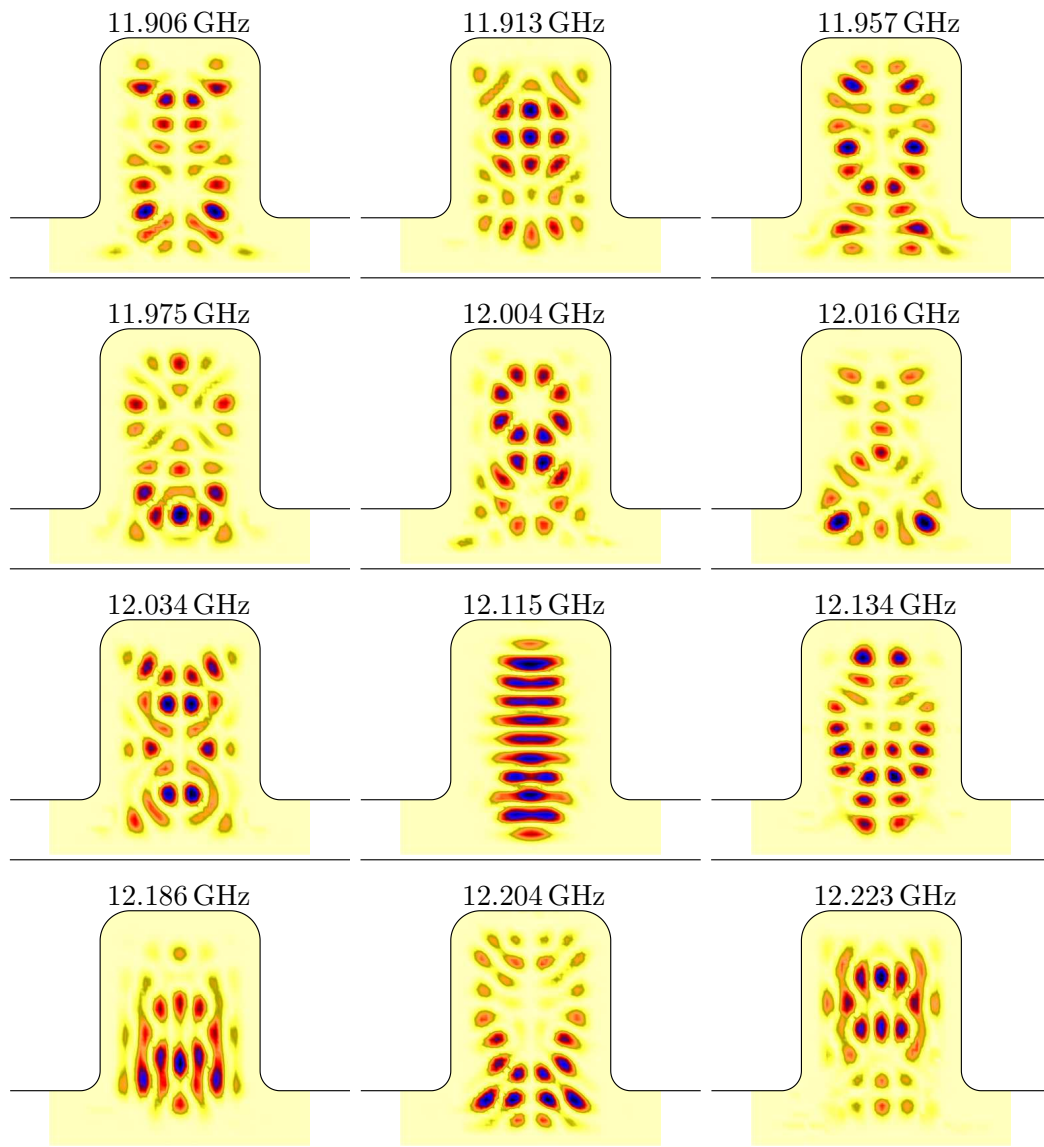
Fitted wave functions for the soft-wall billiard

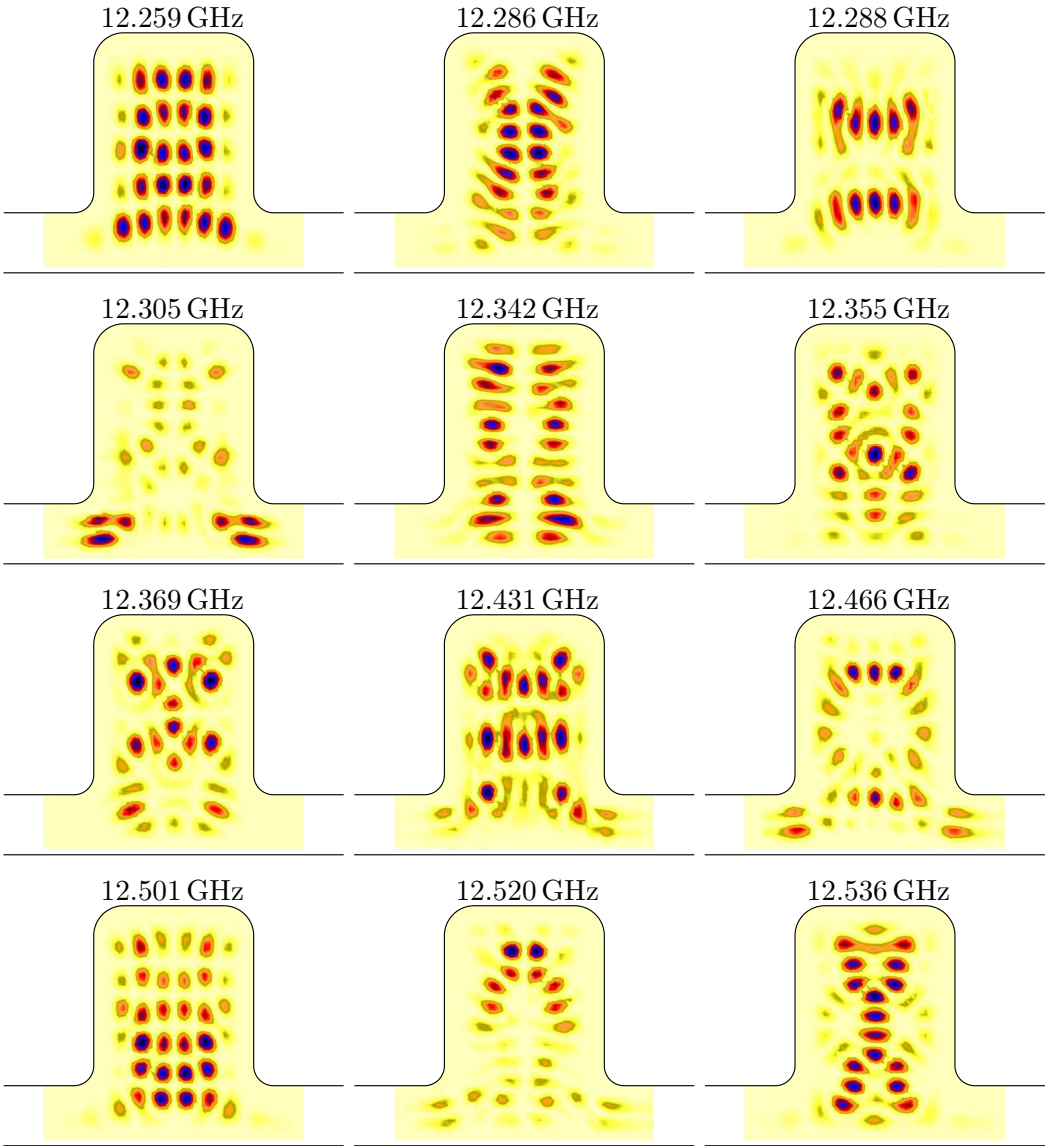


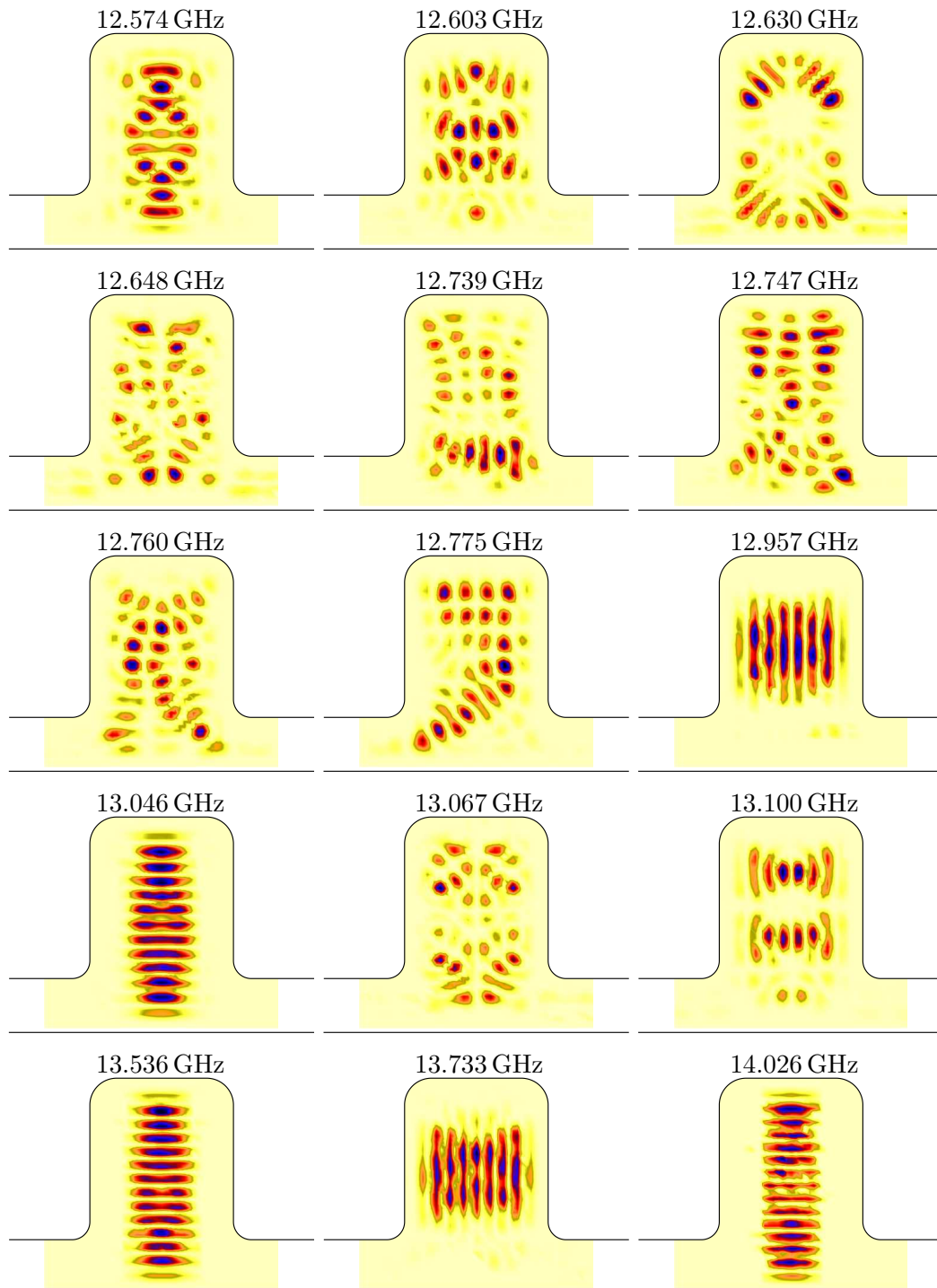












Appendix B

WKB approximation

Semiclassically we can decompose the wave function into an amplitude factor $A(q)$ and a phase factor $S(q)$ for a one-dimensional system

$$\psi(q) = A(q)e^{\frac{i}{\hbar}S(q)}. \quad (\text{B.1})$$

We put this expression into the time-independent Schrödinger equation

$$\frac{-\hbar^2}{2m}\nabla^2\psi(q) = (E - V(q))\psi(q), \quad (\text{B.2})$$

then we obtain

$$A\left(\frac{dS}{dq}\right)^2 - i\hbar A\frac{d^2S}{dq^2} - 2i\hbar\frac{dA}{dq}\frac{dS}{dq} - \hbar^2\frac{d^2A}{dq^2} = 2m(E - V)A \quad (\text{B.3})$$

Separating real and imaginary parts, it yield two equations

$$\left(\frac{dS}{dq}\right)^2 = 2m(E - V) + \frac{\hbar^2}{A}\frac{d^2A}{dq^2} \quad (\text{B.4})$$

$$A\frac{d^2S}{dq^2} + 2\frac{dA}{dq}\frac{dS}{dq} = 0 \quad (\text{B.5})$$

Eq. (B.5) can be paraphrased by

$$\frac{1}{2}\frac{dq}{dS}\frac{d^2S}{dq^2} + \frac{1}{A}\frac{dA}{dq} = 0 \quad (\text{B.6})$$

which is equivalent to

$$\frac{d}{dq}\left(\frac{1}{2}\log\frac{dS}{dq} + \log A\right) = 0 \quad (\text{B.7})$$

The integration of Eq. (B.7) yields

$$A = \frac{\psi_0}{\sqrt{|S|^{\prime}}} \quad (\text{B.8})$$

where ψ_0 is the integration constant.

In the semiclassical limit $\hbar \rightarrow 0$, the term $\frac{\hbar^2}{A} \frac{d^2 A}{dq^2}$ in Eq. (B.4) is negligible and thus Eq. (B.4) yields

$$S = \int_{q_0}^q dq \sqrt{2m(E - V(q))}. \quad (\text{B.9})$$

From Eq. (B.8) and Eq. (B.1) one can obtain

$$\psi(q) = \frac{\psi_0}{\sqrt{\left| \sqrt{2m(E - V(q))} \right|}} \exp\left(\frac{i}{\hbar} \int_{q_0}^q dq \sqrt{2m(E - V(q))}\right) \quad (\text{B.10})$$

This approximation becomes invalid in particular for the classical turning points with $p = 0$. Maslov [Mas81, Eck88] developed this approximation for this problematic region. If the approximation is poor in position space then it should work well in momentum space. The wave function $\hat{\psi}(p)$ in momentum space is obtained from $\psi(q)$ by a Fourier transformation.

$$\begin{aligned} \hat{\psi}(p) &= \frac{1}{\sqrt{2\pi\hbar}} \int dq \psi(q) \exp\left(-\frac{i}{\hbar} qp\right) \\ &= \frac{\psi_0}{\sqrt{2\pi\hbar}} \int dq \frac{\psi_0}{\sqrt{\left| \sqrt{2m(E - V(q))} \right|}} \exp\left(\frac{i}{\hbar} \int dq \sqrt{2m(E - V(q))} - qp\right) \end{aligned} \quad (\text{B.11})$$

The integral is of the type

$$I = \int dq A(q) \exp\left(\frac{i}{\hbar} \Phi(q)\right). \quad (\text{B.12})$$

In the semiclassical limit $\hbar \rightarrow 0$, the phase $\frac{i}{\hbar} \Phi(q)$ oscillates rapidly. These oscillations cause a cancelation of nearly all contributions to the integral. Exceptions are the neighborhoods of the points q_s where the phase is stationary, *i. e.* where

$$\Phi'(q_s) = \frac{1}{\hbar} \left(\sqrt{2m(E - V(q_s))} - p \right) = 0, \quad (\text{B.13})$$

and it yields with the Taylor expansion at the point x_s

$$\Phi(q) = \Phi(q_s) + \frac{(q - q_s)^2}{2} \Phi''(q_s) + \dots \quad (\text{B.14})$$

If $A(q)$ is regular, it may be considered as constant. We thus obtain

$$I \approx A(q_s) \exp\left(\frac{i}{\hbar}\Phi(q_s)\right) \int dq \exp\left(\frac{i}{\hbar}\frac{(q-q_s)^2}{2}\Phi''(q)\right). \quad (\text{B.15})$$

This is of the type of the *Fresnel integral*(see Appendix D), and we thus obtain

$$I \approx \sqrt{\frac{2\pi\hbar}{|\Phi''(q_s)|}} A(q_s) \exp\left(\frac{i}{\hbar}\Phi(q_s) + \frac{i\pi}{4}\text{sgn}(\Phi''(q_s))\right). \quad (\text{B.16})$$

This is the *stationary phase approximation*. Now we can apply this approximation to the integral in Eq. B.12. From Eq. B.13 we can replace q_s with $q(p)$ as a function of p . Now we can express the wave function $\hat{\psi}(p)$ in momentum space by:

$$\hat{\psi}(p) = \psi_0 \sqrt{\left|\frac{q'(p)}{p}\right|} \exp\left(\frac{i}{\hbar} \int_{q_0}^{q(p)} dq \sqrt{2m(E-V(q))} - pq(p) - \frac{i\pi}{4}\right) \quad (\text{B.17})$$

By Fourier transformation into the position space and repeating the same steps as above we obtain the representation of the wave function in the position space

$$\psi(q) = \frac{\psi_0}{\sqrt{|p(q)|}} \exp\left(\frac{i}{\hbar} \int_{q_0}^q dq p(q) - \frac{i\pi}{2}\right) \quad (\text{B.18})$$

where $p(q) = \sqrt{2m(E-V(q))}$ As Eq. B.18 shows there is a phase loss of $\pi/2$ whilst passing the turning point. It yields:

$$\Delta\Phi = \frac{1}{\hbar}S - \frac{\mu\pi}{2}, \quad (\text{B.19})$$

where $S = \oint dq p(q)$, and μ , called the *Maslov index*. For Dirichlet boundary conditions each reflection leads to a phase jump of π , *i. e.* a hard wall reflection contributes twice to the Maslov index, while there is no phase jump for Neumann boundary conditions. Semiclassically only orbits with $\Delta\Phi = n \cdot 2\pi$ are allowed, and this yields

$$\frac{1}{\hbar} \oint dq p(q) = 2\pi \left(n + \frac{\mu}{4}\right). \quad (\text{B.20})$$

Appendix C

Random superposition of plane waves

In the semiclassical case, we can describe the wave function by a random superposition of plane waves with random amplitudes a_n , and random directions of wave number \vec{k}/k ,

$$\psi(\vec{r}) = \sum_n a_n \exp^{i\vec{k}_n \cdot \vec{r}}, \quad k = |\vec{k}_n|. \quad (\text{C.1})$$

The amplitude distribution can be written ,

$$P(\psi) = \left\langle \delta \left(\psi - \sum_n a_n e^{i\vec{k}_n \cdot \vec{r}} \right) \right\rangle,$$

where the average over amplitudes and directions of incoming waves. We can express the delta function by its Fourier representation (compare with Appendix D) and get

$$P(\psi) = \frac{1}{2\pi} \int_{-\infty}^{+\infty} dt e^{it\psi} \prod_{n=1}^N \left\langle e^{-ita_n e^{i\vec{k}_n \cdot \vec{r}}} \right\rangle. \quad (\text{C.2})$$

We have thus obtained a factorization of the averaging over the different contributions. An exponential expansion yields

$$\begin{aligned} \left\langle e^{-ita_n e^{i\vec{k}_n \cdot \vec{r}}} \right\rangle &= 1 - it \left\langle a_n e^{i\vec{k}_n \cdot \vec{r}} \right\rangle - \frac{t^2}{2} \left\langle a_n^2 e^{2i\vec{k}_n \cdot \vec{r}} \right\rangle + \dots \\ &= 1 - \frac{t^2}{2} \langle a_n^2 \rangle + \dots \end{aligned}$$

From the normalization of the wave function in billiard area A , we obtain in the

case of $N \rightarrow \infty$ only terms with $\vec{k}_n = -\vec{k}_m$ remain:

$$1 = \int |\psi(\vec{r})|^2 dA = \sum_{n,m} a_n a_m \int e^{i\vec{k}_n \cdot \vec{r}} e^{i\vec{k}_m \cdot \vec{r}} dA = A \sum_n a_n^2 = AN \langle a_n^2 \rangle.$$

Inserting this result into Eq. C.2 we obtain in the limit $N \rightarrow \infty$:

$$\begin{aligned} P(\psi) &= \frac{1}{2\pi} \int_{-\infty}^{+\infty} dt e^{it\psi} \lim_{N \rightarrow \infty} \left(1 - \frac{t^2}{2AN} + \dots \right)^N \\ &= \frac{1}{2\pi} \int_{-\infty}^{+\infty} dt e^{it\psi} \exp\left(-\frac{t^2}{2A}\right) \\ &= \sqrt{\frac{A}{2\pi}} \exp\left(-\frac{A\psi^2}{2}\right). \end{aligned}$$

This is a Gaussian amplitude distribution and once more a manifestation of the central limit theorem.

One can further obtain a Porter Thomas distribution for intensity $I = |\psi|^2$ distribution,

$$P_\rho(I) = \langle \delta(I - |\psi|^2) \rangle = \sqrt{\frac{A}{2\pi I}} \exp\left(-\frac{AI}{2}\right). \quad (\text{C.3})$$

Appendix D

Mathematical functions/ formulas

In this appendix, the formulas used in previous chapters are listed.

Fresnel integral

$$\int_{-\infty}^{\infty} e^{i\alpha x^2} dx = \sqrt{\frac{\pi}{|\alpha|}} e^{i\frac{\pi}{4}\text{sgn}(\alpha)} \quad (\text{D.1})$$

Fourier representation of δ -function

$$\delta(x) = \frac{1}{2\pi} \int_{-\infty}^{\infty} e^{itx} dx \quad (\text{D.2})$$

Bessel J function

$$\begin{aligned} J_{n-1}(x) + J_{n+1}(x) &= \frac{2n}{x} J_n(x) \\ \frac{dJ_n(x)}{dx} &= -\frac{n}{x} J_n(x) + J_{n-1}(x) \\ \frac{dJ_0(x)}{dx} &= -J_1(x) \\ J_n(x) &= \frac{(-i)^n}{\pi} \int_0^\pi e^{ix \cos \varphi} \cos(n\varphi) d\varphi \\ J_0(x) &= \frac{1}{\pi} \int_0^\pi e^{ix \cos \varphi} \end{aligned}$$

Bessel Y function

$$\begin{aligned} Y_{n-1}(x) + Y_{n+1}(x) &= \frac{2n}{x}Y_n(x) \\ \frac{dY_n(x)}{dx} &= -\frac{n}{x}Y_n(x) + Y_{n-1}(x) \\ \frac{dY_0(x)}{dx} &= -Y_1(x). \end{aligned}$$

Bessel I function

$$\begin{aligned} I_{n-1}(x) - I_{n+1}(x) &= \frac{2n}{x}I_n(x) \\ \frac{dI_n(x)}{dx} &= -\frac{n}{x}I_n(x) + I_{n-1}(x) \\ \frac{dI_0(x)}{dx} &= +I_1(x) \\ I_0(x) &\approx \frac{e^x}{\sqrt{2\pi x}} \quad \text{for } x \gg 1 \\ I_n(x) &= i^{-n}J_n(ix), \quad I_0(x) = J_0(ix), \quad d\varphi. \end{aligned}$$

Bessel K function

$$\begin{aligned} K_{n+1}(x) - K_{n-1}(x) &= \frac{2n}{x}K_n(x) \\ \frac{dK_n(x)}{dx} &= -\frac{n}{x}K_n(x) - K_{n-1}(x) \\ \frac{dK_0(x)}{dx} &= -K_1(x). \end{aligned}$$

Bibliography

- [Bar01] M. Barth. *Mikrowellen-Experimente zu Leveldynamik und Wirbelbildung*. Dissertation Philipps-Universität Marburg (2001).
- [Bar02] M. Barth and H.-J. Stöckmann. Current and vortex statistics in microwave billiards. *Phys. Rev. E* **65**, 066208 (2002).
- [Ber77] M. V. Berry. Regular and irregular semiclassical wavefunctions. *J. Phys. A* **10**, 2083 (1977).
- [Ber85] M. V. Berry. Semiclassical theory of spectral rigidity. *Proc. R. Soc. Lond. A* **400**, 229 (1985).
- [Ber99] K.-F. Berggren, K. N. Pichugin, A. F. Sadreev, and A. Starikov. Signatures of quantum chaos in the nodal points and streamlines in electron transport through billiards. *JETP Lett.* **70**, 403 (1999).
- [Ber00] M. V. Berry and M. R. Dennis. Phase singularities in isotropic random waves. *Proc. R. Soc. Lond. A* **456**, 2059 (2000).
- [Ber01] K.-F. Berggren, A. F. Sadreev, and A. A. Starikov. Quantum chaos among nodal points and streamlines at ballistic electron transport through open quantum dots. *Nanotechnology* **12**, 562 (2001).
- [Ber02] K.-F. Berggren, A. F. Sadreev, and A. A. Starikov. Crossover from regular to irregular behavior in current flow through open billiards. *Phys. Rev. E* **66**, 016218 (2002).
- [Bir95] J. P. Bird, D. M. Olatona, R. Newbury, R. P. Taylor, K. Ishibashi, M. Stopa, Y. Aoyagi, T. Sugano, and Y. Ochiai. Lead-induced transition to chaos in ballistic mesoscopic billiards. *Phys. Rev. B* **52**, R14336 (1995).
- [Bir97a] J. P. Bird, R. Akis, D. K. Ferry, Y. Aoyagi, and T. Sugano. Periodic conductance fluctuations and lead-induced scarring in open quantum dots. *J. Phys.: Condens. Matter* **9**, 5935 (1997).

- [Bir97b] J. P. Bird, K. Ishibashi, Y. Aoyagi, T. Sugano, R. Akis, D. K. Ferry, D. P. Pivin Jr. , K. M. Connolly, R. P. Taylor, R. Newbury, D. M. Olatona, A. Micolich, R. Wirtz, , Y. Ochiai, and Y. Okubo. Quantum transport in open mesoscopic cavities. *Chaos, Solitons & Fractals* **8**, 1299 (1997).
- [Bir99] J. P. Bird, R. Akis, D. K. Ferry, D. Vasileska, J. Cooper, Y. Aoyagi, and T. Sugano. Lead-orientation-dependent wave function scarring in open quantum dots. *Phys. Rev. Lett.* **82**, 4691 (1999).
- [Bro81] T. A. Brody, J. Flores, J. B. French, P. A. Mello, A. Pandey, and S. S. M. Wong. Random-matrix physics: spectrum and strength fluctuations. *Rev. Mod. Phys.* **53**, 385 (1981).
- [Bro03] P. W. Brouwer. Wave function statistics in open chaotic billiards. *Phys. Rev. E* **68**, 046205 (2003).
- [Chu00] S.-H. Chung, A. Gorkirmak, D.-H. Wu, J. S. A. Bridgewater, E. Ott, T. M. Antonsen, and S. M. Anlage. Measurement of wave chaotic eigenfunctions in the time-reversal symmetry-breaking crossover regime. *Phys. Rev. Lett.* **85**, 2482 (2000).
- [Dav81] M. J. Davis and E. J. Heller. Quantum dynamical tunneling in bound states. *J. Chem. Phys.* **75**, 246 (1981).
- [Dör98] U. Dörr, H.-J. Stöckmann, M. Barth, and U. Kuhl. Scarred and chaotic field distributions in three-dimensional Sinai-microwave resonators. *Phys. Rev. Lett.* **80**, 1030 (1998).
- [Doy02] V. Doya, O. Legrand, F. Mortessagne, and C. Miniatura. Light scarring in an optical fiber. *Phys. Rev. Lett.* **88**, 014102 (2002).
- [Ebe84] K. J. Ebeling. Statistical properties of random wave fields. volume 17 of *Physical Acoustics: Principles and Methods* page 233. Academic Press New York (1984).
- [Eck88] B. Eckhardt. Quantum mechanics of classically non-integrable systems. *Phys. Rep.* **163**, 205 (1988).
- [Eck99] B. Eckhardt, U. Dörr, U. Kuhl, and H.-J. Stöckmann. Correlations of electromagnetic fields in irregular cavities. *Europhys. Lett.* **46**, 134 (1999).
- [Ell95] C. Ellegaard, T. Guhr, K. Lindemann, H. Q. Lorensen, J. Nygård, and M. Oxborrow. Spectral statistics of acoustic resonances in aluminium blocks. *Phys. Rev. Lett.* **75**, 1546 (1995).

- [Emi03] V. Emiliani, F. Intonti, M. Cazayous, D. S. Wiersma, M. Colocci, F. Aliev, and A. Lagendijk. Near-field short range correlation in optical waves transmitted through random media. *Phys. Rev. Lett.* **90**, 250801 (2003).
- [Fro94] T. M. Fromhold, L. Eaves, F. W. Sheard, M. L. Leadbeater, T. J. Foster, and P. C. Main. Magnetotunneling spectroscopy of a quantum well in the regime of classical chaos. *Phys. Rev. Lett.* **72**, 2608 (1994).
- [Fro95] T. M. Fromhold, P. B. Wilkinson, F. W. Sheard, L. Eaves, J. Miao, and G. Edwards. Manifestation of classical chaos in the energy level spectrum of a quantum well. *Phys. Rev. Lett.* **75**, 1142 (1995).
- [Grä92] H.-D. Gräf, H. L. Harney, H. Lengers, C. H. Lewenkopf, C. Rangacharyulu, A. Richter, P. Schardt, and H. A. Weidenmüller. Distribution of eigenmodes in a superconducting stadium billiard with chaotic dynamics. *Phys. Rev. Lett.* **69**, 1296 (1992).
- [Guh97] T. Guhr and A. Müller-Groeling. Spectral correlations in the crossover between GUE and poisson regularity: on the identification of scales. *J. Math. Phys.* **38**, 1870 (1997).
- [Guh98] T. Guhr, A. Müller-Groeling, and H. A. Weidenmüller. Random matrix theories in quantum physics: common concepts. *Phys. Rep.* **299**, 189 (1998).
- [Gut90] M. C. Gutzwiller. *Chaos in Classical and Quantum Mechanics*. Interdisciplinary Applied Mathematics, Vol. 1. Springer New York (1990).
- [Haa01] F. Haake. *Quantum Signatures of Chaos. 2nd edition*. Springer Berlin (2001).
- [Hel95] E. J. Heller. Dynamical tunneling and molecular spectra. *J. Phys. C* **99**, 2625 (1995).
- [Hen01] W. K. Hensinger, H. Häffner, A. Browaeys, N. R. Heckenberg, K. Helmerson, C. McKenzie, G. J. Milburn, W. D. Phillips, S. L. Rolston, H. Rubinsztein-Dunlop, and B. Uppcroft. Dynamical tunnelling of ultracold atoms. *Nature* **412**, 52 (2001).
- [Jac82] J. D. Jackson. *Klassische Elektrodynamik, 2. Auflage*. de Gruyter Berlin (1982).
- [Jal90] R. A. Jalabert, H. U. Baranger, and A. D. Stone. Conductance fluctuations in the ballistic regime: A probe of quantum chaos? *Phys. Rev. Lett.* **65**, 2442 (1990).

- [Kan96] E. Kanzieper and V. Freilikher. Eigenfunctions of electrons in weakly disordered quantum dots: Crossover between orthogonal and unitary symmetries. *Phys. Rev. B* **54**, 8737 (1996).
- [Kim02] Y.-H. Kim, M. Barth, H.-J. Stöckmann, and J. P. Bird. Wavefunction scarring in open quantum dots: A microwave-billiard analogy study. *Phys. Rev. B* **65**, 165317 (2002).
- [Kuh98] U. Kuhl. *Mikrowellenuntersuchungen an eindimensionalen Streusystemen und in zweidimensionalen Kavitäten*. Dissertation Philipps-Universität Marburg (1998).
- [Kuh01] U. Kuhl and H.-J. Stöckmann. Microwave transmission spectra in regular and irregular one-dimensional scattering arrangements. *Physica E* **9**, 384 (2001).
- [Lan97] S. A. van Langen, P. W. Brouwer, and C. W. J. Beenakker. Fluctuating phase rigidity for a quantum chaotic system with partially broken time-reversal symmetry. *Phys. Rev. E* **55**, R1 (1997).
- [Lau94] H.-M. Lauber. *Experimenteller Nachweis geometrischer Phasen und Untersuchungen der Wellenmechanik nichtintegrierbarer Systeme mit Mikrowellenresonatoren*. Dissertation Ruprecht-Karls-Universität Heidelberg (1994).
- [Mar92] C. M. Marcus, A. J. Rimberg, R. M. Westervelt, P. F. Hopkins, and A. C. Gossard. Conductance fluctuations and chaotic scattering in ballistic microstructures. *Phys. Rev. Lett.* **69**, 506 (1992).
- [Mas81] V. P. Maslov and N. V. Fedoriuk. *Semi-Classical Approximation in Quantum Mechanics*. Reidel Dordrecht (1981).
- [McD79] S. W. McDonald and A. N. Kaufman. Spectrum and eigenfunctions for a Hamiltonian with stochastic trajectories. *Phys. Rev. Lett.* **42**, 1189 (1979).
- [McD88] S. W. McDonald and A. N. Kaufman. Wave chaos in the stadium: Statistical properties of short-wave solutions of the Helmholtz equation. *Phys. Rev. A* **37**, 3067 (1988).
- [Mic98] A. P. Micolich, R. P. Taylor, R. Newbury, J. P. Bird, R. Wirtz, C. P. Dettmann, Y. Aoyagi, and T. Sugano. Geometry-induced fractal behaviour in a semiconductor billiard. *J. Phys.: Condens. Matter* **10**, 1339 (1998).

- [Mou02] A. P. S. de Moura, Y.-C. Lai, R. Akis, J. P. Bird, and D. K. Ferry. Tunneling and nonhyperbolicity in quantum dots. *Phys. Rev. Lett.* **88**, 236804 (2002).
- [Per00] E. Persson, I. Rotter, H.-J. Stöckmann, and M. Barth. Observation of resonance trapping in an open microwave cavity. *Phys. Rev. Lett.* **85**, 2478 (2000).
- [Pni96] R. Pnini and B. Shapiro. Intensity fluctuations in closed and open systems. *Phys. Rev. E* **54**, R1032 (1996).
- [Sai01] A. I. Saichev, K.-F. Berggren, and A. F. Sadreev. Distribution of nearest distances between nodal points for the Berry function in two dimensions. *Phys. Rev. E* **64**, 036222 (2001).
- [Sai02] A. I. Saichev, H. Ishio, A. F. Sadreev, and K.-F. Berggren. Statistics of interior current distributions in two-dimensional open chaotic billiards. *J. Phys. A* **35**, L87 (2002).
- [Sch94] M. Schroeder. Zahlentheorie in der Physik. *Phys. Bl.* **50**, 1123 (1994).
- [Sch01] K. Schaadt. *Experiments on Acoustic Chaology and Statistical Elastodynamics*. Dissertation Niels Bohr Institute, Copenhagen (2001).
- [Šeb99] P. Šeba, U. Kuhl, M. Barth, and H.-J. Stöckmann. Experimental verification of topologically induced vortices inside a billiard. *J. Phys. A* **32**, 8225 (1999).
- [Seb02] P. Sebbah, B. Hu, A. Z. Genack, R. Pnini, and B. Shapiro. Spatial-field correlation: The building block of mesoscopic fluctuations. *Phys. Rev. Lett.* **88**, 123901 (2002).
- [Sre96a] M. Srednicki. Gaussian random eigenfunctions and spatial correlations in quantum dots. *Phys. Rev. E* **54**, 954 (1996).
- [Sre96b] M. Srednicki and F. Stiernelof. Gaussian fluctuations in chaotic eigenstates. *J. Phys. A* **29**, 5817 (1996).
- [Sri91] S. Sridhar. Experimental observation of scarred eigenfunctions of chaotic microwave cavities. *Phys. Rev. Lett.* **67**, 785 (1991).
- [Ste93] J. Stein. *Eigenfunktionen von Hohlraumresonatoren*. Dissertation Philipps-Universität Marburg (1993).
- [Ste95] J. Stein, H.-J. Stöckmann, and U. Stoffregen. Microwave studies of billiard Green functions and propagators. *Phys. Rev. Lett.* **75**, 53 (1995).

- [Ste01] D. A. Steck, W. H. Oskay, and M. G. Raizen. Observation of chaos-assisted tunneling between islands of stability. *Science* **293**, 274 (2001).
- [Stö90] H.-J. Stöckmann and J. Stein. “Quantum” chaos in billiards studied by microwave absorption. *Phys. Rev. Lett.* **64**, 2215 (1990).
- [Stö99] H.-J. Stöckmann. *Quantum Chaos - An Introduction*. University Press Cambridge (1999).
- [Tom94] S. Tomsovic and D. Ullmo. Chaos-assisted tunneling. *Phys. Rev. E* **50**, 145 (1994).
- [Tom01] S. Tomsovic. Tunneling and chaos. *Phys. Scr.* **T90**, 162 (2001).
- [Top00] M. A. Topinka, B. J. LeRoy, S. E. J. Shaw, E. J. Heller, R. M. Westervelt, K. D. Maranowski, and A. C. Gossard. Imaging coherent electron flow from a quantum point contact. *Science* **289**, 2323 (2000).
- [Top01] M. A. Topinka, B. J. LeRoy, R. M. Westervelt, S. E. J. Shaw, R. Fleischmann, E. J. Heller, K. D. Maranowski, and A. C. Gossard. Coherent branched flow in a two-dimensional electron gas. *Nature* **410**, 183 (2001).
- [Vra02] M. Vraničar, M. Barth, G. Veble, M. Robnik, and H.-J. Stöckmann. ‘Persistent currents’ and eigenfunctions in microwave resonators with broken time reversal symmetry. *J. Phys. A* **35**, 4929 (2002).
- [Woo02] M. T. Woodside and P. L. McEuen. Scanned probe imaging of single-electron charge states in nanotube quantum dots. *Science* **296**, 1098 (2002).
- [Życ91] K. Życzkowski and G. Lenz. Eigenvector statistics for the transitions from the orthogonal to the unitary ensemble. *Z. Phys. B* **82**, 299 (1991).

Acknowledgments

First of all, I would like to give my thanks to my supervisor Prof. Dr. Hans-Jürgen Stöckmann for the help, guidance and encouragement he has given me and for all his patience with me. I also thank him for a good collegial relationship.

I am grateful to my second thesis advisor Prof. Dr. Jonathan. P. Bird for his stimulating suggestions, good and fruitful collaboration, including finding funds for my stay in ASU.

I would like to express my gratitude to Prof. Dr. Piet. W. Brouwer for his invaluable theoretical insights and support.

I thank my colleagues Ulrich Kuhl, Michael Barth, Hendrik Schanze, Rudi Schäfer, Ruven Höhemann from the AG-Quantenchaos for good working conditions during my Ph.D time. A special thanks goes to Ulrich Kuhl for a critical reading of the text.

My gratitude extends to the staff at the institutes of the faculty of physics, especially the fine mechanical workshop.

Finally, I thank to my dear family.

Wissenschaftlicher Werdegang

Name	Kim
Vorname	Young-Hee
Geburtsdatum	15.04.1969
Geburtsort	Seoul
Familienstand	ledig
Schulbesuch	Grundschule Eonju 1975 - 1981 Mittelschule Seocho 1981 - 1984 Oberschule Duksung 1984 - 1987 - Allgemeine Hochschulreife am 13.02.1987
Studium der Pharmazie	Universität Duksung in Seoul, 1987 - 1991 - Bachelor 27.02.1991
Studium der Physik	Universität Marburg, 1996 - 1998 - Vordiplom 1998 - Diplom am 13.03.2001
Berufstätigkeit	Wissenschaftliche Angestellte 2001 - 2004 am Fachbereich Physik der Philipps-Universität Marburg

